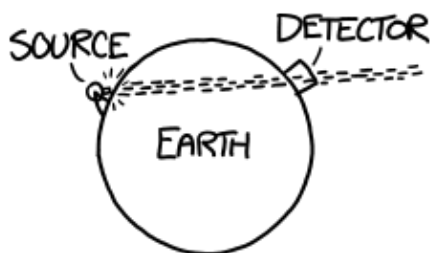


ALEXIS NIKOLAKOPOULOS

ENERGY RECONSTRUCTION IN ACCELERATOR BASED
NEUTRINO NUCLEUS SCATTERING EXPERIMENTS

ENERGY RECONSTRUCTION IN ACCELERATOR BASED NEUTRINO NUCLEUS SCATTERING EXPERIMENTS

ALEXIS NIKOLAKOPOULOS



Promotor: prof. dr. Natalie Jachowicz
Theoretical nuclear and statistical physics
Faculty of science
UGent

June 2017

ABSTRACT

In accelerator-based neutrino scattering experiments, the neutrino flux is often broadly spread over a large region of energies. Measurements of neutrino-oscillation parameters are dependent on accurate determination of the neutrino energy. The determination of neutrino energy from inclusive measurements of charged-current quasi-elastic scattering events, is based on the reconstruction of the energy by the lepton energy, and the scattering angle. The distribution of reconstructed energies \bar{E}_ν is then unfolded using theoretical models that determine the conditional probability of an event being due to a neutrino having a certain real energy E_ν , for a given reconstructed energy. It has been shown that nuclear effects beyond the impulse approximation can severely influence the interpretation of data in terms of reconstructed energies. We explore the effects of the reconstruction procedure by confronting the Hartree-Fock and continuum random phase approximation, models developed in the Ghent nuclear physics group, with the reconstruction procedure. We compare the obtained distributions with different (local) relativistic Fermi gas models. It is shown that these mean-field descriptions feature a more spread out distribution of energies for a fixed reconstructed energy. This leads to a redistribution of strength from high- \bar{E}_ν values, to lower values, effectively increasing the number of events found around the peak of the MiniBooNE flux. The effect is reminiscent of the well-established redistribution when including multi-nucleon knock-out contributions to the cross section, although it is not of the same magnitude. The magnitude of the effect is not well established, uncertainties regarding the cross section for energies higher than 1.5 GeV would first have to be resolved.

SAMENVATTING

In neutrino experimenten waarbij neutrino's gemaakt worden door interacties van protonen uit deeltjesversnellers is de flux uitgesmeerd over een brede waaier van energieën. Accurate metingen van de oscillatieparameters hangen af van hoe nauwkeurig de energie van het neutrino bepaald kan worden. Het bepalen van de energie in een inclusief quasi-elastisch proces, is gebaseerd op de reconstructie van de energie op basis van de verstrooiingshoek en de energie van het uitgaande lepton. The distributie van gereconstrueerde energieën \bar{E}_ν wordt vervolgens herverdeelt over echte energieën door gebruik te maken van modellen voor de interactie van het neutrino met de kern. Op basis van een theoretisch model kan de conditionele waarschijnlijkheid bepaald worden van een echte energie, gegeven een zekere gereconstrueerde energie. Er werd reeds aangetoond dat nucleaire effecten belangrijk zijn in deze procedure, en dat de interpretatie van data in termen van gereconstrueerde energieën erdoor bemoeilijkt wordt. We onderzoeken de effecten van de reconstructieprocedure door deze toe te passen op de Hartree-Fock, en continuum random phase approximation modellen ontwikkeld in de Gentse vakgroep voor nucleaire fysica. We vergelijken de distributies van energieën met verschillende (lokale) relativistische Fermigas modellen. Het wordt aangetoond dat deze mean-field beschrijvingen van de kern aanleiding geven tot meer uitgespreide distributies van energieën voor een gegeven gereconstrueerde energie. Dit leidt tot een herverdeling van sterkte in de gereconstrueerde distributie, van hoge waarden van \bar{E}_ν naar lagere waarden. Dit effect is analoog aan wat men ziet als multi-nucleon knock-out processen worden toegevoegd aan de werkzame doorsnede, echter op een minder grote schaal. De grootte van de herverdeling is nog een vraagteken, de onzekerheden betreffende de werkzame doorsnede voor energieën groter dan ≈ 1.5 GeV moeten eerst afgeschat worden.

CONTENTS

0	INTRODUCTION	1
1	NEUTRINOS AND THE STANDARD MODEL	7
1.1	Neutrino interaction	7
1.2	Sterile neutrinos and neutrino masses	9
1.2.1	Dirac mass term	11
1.2.2	Majorana mass term	11
1.2.3	See-saw mechanism	12
1.3	Neutrino oscillations	13
2	QUASI ELASTIC NEUTRINO SCATTERING	17
2.1	Quasi-elastic scattering on the neutron	17
2.2	Quasi-elastic scattering off the nucleus	20
2.2.1	Partial wave decomposition	21
2.3	Modeling quasi-elastic neutrino-nucleus scattering	23
2.3.1	Impulse Approximation	23
2.3.2	Nuclear structure	24
2.3.3	Modern descriptions of neutrino-nucleus scattering	25
3	NEUTRINO EXPERIMENTS	29
3.1	Neutrino beams	29
3.2	Detectors	32
3.3	Experiments	34
3.3.1	MiniBooNE	35
4	ENERGY RECONSTRUCTION	37
4.1	Quasi-elastic energy reconstruction	37
4.2	Energy distributions with fixed lepton observables	39
4.2.1	Comparison of reconstructed energy distributions	41
5	RECONSTRUCTED ENERGY DISTRIBUTIONS	47
5.1	The smearing function	47
5.2	Cross section in terms of reconstructed energies	48
5.2.1	Unfolding procedure	50
5.3	Comparison of $d(E_\nu, \bar{E}_\nu)$ in different models	51
5.3.1	Dependence on lepton mass and separation energy	51
5.3.2	Comparison of the Hartree-Fock and Continuum Random Phase Approximation	55
5.3.3	Comparison with the RFG approach and multi-nucleon contributions	59
5.4	Reconstructed cross sections	62
5.4.1	Cross sections in terms of real energies	63
5.4.2	Influence of the binding energy	64

5.4.3	Distribution of reconstructed energies in the mean field model	66
6	CONCLUSION	69
	BIBLIOGRAPHY	73



INTRODUCTION

The neutrino was hypothesized by Pauli in 1930 to explain the conservation of energy and momentum in β -decay. The energy spectrum of electrons from β -decay of a nucleus is continuous, thus under the assumption that only one particle (the electron) was produced in the decay, energy seems to disappear. Pauli suggested an electrically neutral unobserved particle that carried the missing energy and momentum.

In 1954, the neutrino was experimentally observed in inverse β -decay reactions [1]. This neutrino was associated with the electron. Later, neutrinos associated with the muon [2] and τ lepton [3] were experimentally observed. The neutrinos complete the leptonic sector in the standard model. This sector contains 3 charged leptons and 3 neutrinos of the same flavor.

The neutrino is an uncharged lepton, meaning it only interacts through the weak interaction. The weak interaction is a chiral theory, meaning that it only couples left-handed fermions, and right-handed anti-fermions. The handedness of a particle, often called its chirality is an abstract concept determined by the transformation of particle states. Initially the neutrino was thought to be massless, and due to it only interacting weakly, neutrinos were thought to only exist as left(right)-handed (anti-)particles.

By inclusion of the Higgs-boson in the standard model, giving mass to the charge-mediating bosons in the electroweak sector and the fermions, neutrinos remain consistently massless. For a fermion to obtain mass by coupling to the Higgs-boson, it requires a right-handed component. The neutrino, lacking this component, is thus well described by the standard model.

That is until neutrinos were shown to oscillate. The first hint towards oscillating neutrinos was given by the Homestake experiment [4]. The experiment counted the neutrinos created by nuclear fusion in the sun. For this they used a detector where neutrinos induced the transformation of ^{37}Cl into radioactive ^{37}Ar . The argon was periodically filtered out of a large tank of chlorine, the number of argon nuclei was then counted by observation of their radioactive decay. The experiment found that the amount of neutrinos originating from the sun was smaller than the theoretical models [5] predicted.

The deficit of neutrinos originating from the sun was further established by the Sudbury neutrino observatory (SNO) experiment [6]. Also the Super-Kamiokande experiment [7], measured a deficit of neutrinos originating from interactions of high-energy cosmic rays with the earths atmosphere. The experiments found a deficit of neutrinos of a specific type, compared to well-established theoretical models, but the total number of neutrinos (of all types) however was consistent with the predictions.

In this way neutrinos were shown to oscillate, i.e. they change their type when traveling. These oscillations of neutrino flavor are possible when neutrinos have a non-zero mass. The neutrino flavor states are a superposition of neutrino mass states. The mass states define how neutrinos, when they are not interacting, will propagate through space. After propagating for some distance L , the propagated mass states can be described as a superposition of flavor eigenstates. When this neutrino interacts however a definite flavor state has to be recovered. For example in a charge-changing interaction with the neutron, a lepton of a specific flavor can be detected, the neutrino then has to have the same flavor.

$$\nu_l + n \rightarrow p + l$$

In a simple model, where only 2 neutrinos are considered, lets say the electron- and muon-neutrino, the probability of the ν_e being transformed into a ν_μ , at some distance L from where the electron neutrino was last detected is given by

$$P(\nu_e \rightarrow \nu_\mu) = \sin^2 2\theta \left(\frac{L (m_1^2 - m_2^2)}{4E_\nu} \right),$$

where E_ν is the neutrino energy, m_i are the definite masses of the neutrino mass states, and θ determines how the mass states relate to the flavor states.

With neutrino oscillations firmly established, the question remains how neutrinos can obtain mass in the standard model. The most simple method is by introducing right-handed components for the neutrinos. The neutrino can then obtain a mass in the same way as the other fermions. The right-handed components of neutrinos do not interact at all, they do not have a flavor, nor an electric charge or color. While the number of active neutrinos (the ones with a definite flavor) is fixed at 3 by considering the decay width of the Z-boson, there is no direct limit on the amount of inactive right-handed neutrinos. The only way in which additional right-handed neutrinos could influence physical processes, is by their effect on neutrino oscillations.

Another way in which neutrinos could obtain mass is by considering them to be *Majorana* particles. Simply stated a Majorana particle is its own anti-particle, and the antiparticle state that behaves right-handed can be constructed from the particle state. But coupling a leptonic particle to its anti-particle violates lepton number. It is impossible to generate such a coupling with the single Higgs-boson in the standard model, and the particle content of the standard model would have to be extended.

ACCELERATOR BASED NEUTRINO EXPERIMENTS

This brings us to the current state of neutrino physics: neutrino oscillations are established, implying that neutrinos have mass, but the mechanism in which they acquire mass is unknown. Many experiments measure (or have measured) the parameters that determine neutrino oscillations, being the squared mass differences and elements of the mixing matrix, and these parameters are thus constrained, but the

nature of neutrino mixing is not yet completely determined. The new generation of neutrino experiments that set out to study neutrino oscillations look at neutrinos created in controlled collisions of high-energy protons from particle accelerators with a target. They are referred to as accelerator-based experiments.

A particle accelerator provides high energy protons which are directed into a nuclear target. The interactions between the protons and the target material produce mainly pions, and other charged mesons. The resulting charged mesons are directed to a decay pipe by electromagnetic devices, named focusing horns. These horns focus the beam and make it possible to select mesons based on their charge. In the decay region the prominent pions decay primarily into muons and muon neutrinos. Depending on the selected charge of the pions (π^+ or π^-), the resulting beam is composed mainly of ν_μ or $\bar{\nu}_\mu$, respectively [8].

Neutrino oscillations depend on the fraction $\frac{L}{E_\nu}$, in these experiments the distance L can be tuned at will, and by tuning the beam the energy E_ν is also under control. The neutrino beam however consists of neutrinos with many different energies. Accurate measurement of oscillation parameters requires the energy to be known to high precision.

In order to determine the neutrino energy distribution seen in a detector, the energy of the neutrino has to be inferred from the interaction with the detector material. In order to do this the interaction of the neutrino with the nuclei in the detector has to be modeled.

Recent developments have shown that different nuclear models can severely influence the interpretation of data, not only in analysis of neutrino oscillations, but also from a nuclear modeling standpoint. It has been accepted that in order to determine the neutrino energy in the few-GeV region, many effects beyond the impulse approximation play an important role.

Inclusion of multi-nucleon knock-out contributions, short- and long-range correlations, final-state interactions, etc. have a non-trivial effect on the reconstruction- and unfolding procedures used to determine the distribution of neutrino energies.

Energy reconstruction

The procedure by which the distribution in terms of E_ν is determined in the Miniature Booster Neutrino Experiment ([MiniBooNE](#)) [9] is as follows. A Charged-Current Quasi Elastic ([CCQE](#))-like scattering event is defined as an event where only a charged lepton is found in the final state. The inclusive interaction is

$$\nu_l + {}^{12}\text{C} \rightarrow X + l(E_l, \mathbf{q}_l),$$

in which only the final state lepton is observed. The final nuclear state X is not observed or measured in any way. The reaction is assumed to be a [CCQE](#) scattering

event, in which a single neutron absorbs all energy, transforming it into a proton which is knocked out of the nucleus.

Based on this assumption the reconstructed energy of the event \bar{E}_ν is defined by the final state lepton observables as

$$\bar{E}_\nu = \frac{2M'_n E_l - ((M'_n)^2 + m_l^2 - M_p^2)}{2(M'_n - E_l + P_l \cos \theta)},$$

where $M'_n = M_n - E_B$, and M_n, M_p are the neutron- and proton mass respectively. This definition of the reconstructed energy is based on the scattering off a neutron on the quasi-elastic peak, which is bound in the nucleus by a fixed value of E_B .

This leads to a distribution of events in terms of their reconstructed energies. These distributions are modeled by a nuclear model, usually based on a Relativistic Fermi Gas (RFG) description of the nucleus. A theoretical model allows to calculate the number of events in terms of \bar{E}_ν , given a certain value of E_ν .

Using these conditional probabilities, the amount of events in bins of \bar{E}_ν are distributed into bins of E_ν^{RFG} , where the superscript indicates that a relativistic Fermi gas was used in the procedure. If the nuclear model describes the reaction well, this procedure results in a distribution of energies that closely resemble the real energy. However when in this procedure, dubbed unfolding, the model is not well suited to the actual scattering-process the unfolded distribution will not represent the true energy distribution.

In this work the focus is the distribution of reconstructed energies. We consider this distribution for the pure charged-current quasi-elastic scattering process in which one nucleon is knocked-out.

OUTLINE

In *chapter 1*, the electroweak sector of the standard model is presented. The mass-generating mechanism for the fermions is touched upon, and some mechanisms for neutrino mass generation are discussed. Neutrino oscillations are also presented, and the most common form of the neutrino-mass mixing matrix, the Pontecorvo-Maki-Nakagawa-Sakata (PMNS) matrix is discussed.

In *chapter 2* we discuss charged-current quasi-elastic scattering of neutrinos. First scattering off the neutron is discussed, the cross section is determined by the hadron current which is parametrized by form factors. We then turn to the nucleus, a general overview of the determination of the cross section is presented by introducing the nuclear current leading to the nuclear response functions. The Impulse Approximation (IA) as most common approximation of the nuclear current, and nuclear structure-effects and common techniques are presented. Finally we list some prominent modern approaches to calculation of the CCQE scattering on the nucleus at energies relevant for accelerator-based experiments. The Hartree Fock (HF), and

Continuum Random Phase Approximation (CRPA) models developed in the Ghent nuclear physics group [10], are also presented.

In *chapter 3* we give an overview of accelerator-based neutrino experiments. Different neutrino beams, detectors, and experiments are presented. We use the MiniBooNE as a case study to highlight the interplay of nuclear modeling with neutrino experiments.

In *chapter 4* the quasi-elastic reconstruction procedure is outlined. We mention some work done on the influence of nuclear effects on the reconstruction procedure. The implications of the reconstruction procedure are discussed by looking at the probability of a neutrino having energy E_ν scattering off a nucleus, with fixed E_l , and $\cos\theta$ for the final lepton. The HF/CRPA models are compared to a (local) RFG in different parameter regions. Also the influence of the neutrino flux on these distributions is highlighted.

In *Chapter 5*, the conditional probability of a neutrino having energy E_ν for some given \bar{E}_ν is examined. We show how this probability can be obtained from a cross section. We also touch on the unfolding procedure and present an approximate way to consider unfolded data from a given theoretical model. The probability distributions obtained from the HF and CRPA are compared, also the comparison with simple RFG models is made.

NEUTRINOS AND THE STANDARD MODEL

The neutrino was hypothesized by Pauli in 1930 to explain the conservation of energy and momentum in β -decay. The energy spectrum of electrons from β -decay of a nucleus is continuous, thus under the assumption that only one particle (the electron) was produced in the decay, energy seems to disappear. Pauli suggested a neutral unobserved particle that carried the missing energy and momentum. In 1954, the neutrino was experimentally observed in inverse β -decay reactions [1]. This neutrino was associated with the electron. Later, neutrinos associated with the muon [2] and τ lepton [3] were experimentally observed. The neutrinos complete the leptonic sector in the standard model. The leptonic sector contains 3 charged leptons and their uncharged neutrinos of the same flavor. In the first section we will give a short overview of relevant terms in the standard model Lagrangian and discuss the peculiarities arising with neutrinos. Then we discuss some mechanisms to explain the mass of the neutrino. Lastly we discuss the implications of specific neutrino mass mixing schemes on neutrino oscillations.

1.1 NEUTRINO INTERACTION

The fermion fields of flavor l (either e , μ , or τ) are contained in a left handed-doublet and right-handed singlet

$$\Psi_L = \begin{pmatrix} \nu_{lL} \\ l_L \end{pmatrix}, \quad \Psi_R = l_R, \quad (1.1)$$

which transform under a $SU(2)_L \times U(1)_Y$ gauge group. The right-handed singlets do not transform under $SU(2)_L$, the left handed doublets transform as

$$\Psi_L \rightarrow \Psi'_L = \exp(i g \tau_j \omega_j(x)/2) \Psi_L, \quad (1.2)$$

$$\bar{\Psi}_L \rightarrow \bar{\Psi}'_L = \bar{\Psi}_L \exp(-i g \tau_j \omega_j(x)/2), \quad (1.3)$$

where $\omega_j(x)$ are arbitrary functions, g is a real parameter which will be related to the weak coupling constant, and the τ_j represent the Pauli matrices. The fields transform under $U(1)$ transformations

$$\Psi \rightarrow \Psi' = \exp(i g' Y f(x)) \Psi, \quad (1.4)$$

$$\bar{\Psi} \rightarrow \bar{\Psi}' = \bar{\Psi} \exp(-i g' Y f(x)), \quad (1.5)$$

with $f(x)$ an arbitrary function, g' a real parameter and Y the weak hypercharge which is $-1/2$ for the left handed leptons, and -1 for the right handed charged lepton fields.

Note that we only include a right handed singlet for the charged leptons. Experiments find only left-handed (right-handed) (anti-)neutrinos in interactions. Thus as far as interactions go right handed neutrino terms should not be included. One can however include a right-handed neutrino as a singlet with hypercharge $Y = 0$. This right-handed term will then not appear in the interaction Lagrangian.

The Lagrangian is made invariant under local gauge transformations by applying the Yang-Mills prescription. Therefore introducing 3 gauge fields $W_j^\mu(x)$ defined to be invariant under $U(1)$ transformations and the field $B^\mu(x)$ invariant under $SU(2)$. Defining the covariant derivatives as:

$$D^\mu \Psi_L(x) = \left[\partial^\mu + ig\tau_j W_j^\mu(x)/2 + ig'B^\mu(x)/2 \right] \Psi_L(x), \quad (1.6)$$

$$D^\mu \Psi_R(x) = \left[\partial^\mu - ig'B^\mu(x) \right] \Psi_R(x), \quad (1.7)$$

results in the Lagrangian density

$$\mathcal{L} = \sum \bar{\Psi} \not{D} \Psi, \quad (1.8)$$

that is invariant under local $SU(2)_L \times U(1)_Y$ transformations.

The sum is taken over all lepton generations, and over the left- and right-handed fermion fields. The interpretation in terms of the physical gauge bosons, the W^\pm , Z , and photon A , is done through identification of the bosons in terms of combinations of the gauge fields. One defines the electrically charged boson fields W and it's adjoint W^\dagger by

$$W^\mu = \frac{1}{\sqrt{2}} \left(W_1^\mu - iW_2^\mu \right), \quad W^{\dagger\mu} = \frac{1}{\sqrt{2}} \left(W_1^\mu + iW_2^\mu \right). \quad (1.9)$$

The neutral Z_μ and the photon field A_μ are obtained as a linear combination of W_3^μ and B^μ , generally written as the rotation over the weak mixing angle θ_W

$$W_3^\mu = \cos \theta_W Z_\mu + \sin \theta_W A_\mu, \quad (1.10)$$

$$B^\mu = -\sin \theta_W Z_\mu + \cos \theta_W A_\mu. \quad (1.11)$$

To compactify the equations we first introduce the charged leptonic currents J^μ , the neutral current J_3^μ and the electromagnetic current s^μ in terms of the fermion fields and γ matrices

$$J^\mu = \bar{\Psi}_l^L \frac{1}{2} \gamma^\mu (\tau_1 - i\tau_2) \Psi_l^L = \bar{l}^L \gamma^\mu \nu_l^L, \quad (1.12)$$

$$J^{\mu\dagger} = \bar{\Psi}_l^L \frac{1}{2} \gamma^\mu (\tau_1 + i\tau_2) \Psi_l^L = \bar{\nu}_l^L \gamma^\mu l^L, \quad (1.13)$$

$$J_3^\mu = \frac{1}{2} \bar{\Psi}_l^L \gamma^\mu \tau_3 \Psi_l^L = -\frac{1}{2} \left[\bar{\nu}_l^L \gamma^\mu \nu_l^L - \bar{l}^L \gamma^\mu l^L \right], \quad (1.14)$$

$$s^\mu = J_3^\mu + J_Y^\mu = \frac{1}{2} \bar{\Psi}_l^L \gamma^\mu (\tau_3 + Y\mathbb{1}) \Psi_l^L - \bar{l}_R \gamma^\mu l_R = Q \bar{l} \gamma^\mu l. \quad (1.15)$$

Table 1.1: Overview of the fermions in the standard model and their electroweak charges, namely the third component of weak isospin I_3 and weak hypercharge Y_W . The electromagnetic charge is given by $Q = I_3 + Y_W$.

	I_3		Y_W	
	left-handed	right-handed	left-handed	right-handed
e, μ, τ	$-1/2$	0	-1	-2
ν_e, ν_μ, ν_τ	$1/2$	$-$	-1	$-$
u, c, t	$1/2$	0	$1/6$	$2/3$
d, s, b	$-1/2$	0	$1/6$	$-1/3$

The charged and neutral currents couple to the left handed doublets. While the electromagnetic current is a combination of the hypercharge and isospin currents such that the charge is given by $Q = I_3 + Y_W$. I_3 is the third component of weak isospin, for the lower components of a left handed doublet $I_3 = -1/2$, while the upper components carry $I_3 = 1/2$.

If one rewrites the interaction Lagrangian (the terms in eq. (1.8) containing the vector fields) in terms of the newly defined fields and currents, one sees that in order to interpret A_μ as the photon field it should not couple to the neutral current, and the coupling constant for $s(x)^\mu A_\mu$ should be e . This requires that

$$g \sin \theta_W = g' \cos \theta_W = e. \quad (1.16)$$

We can now compactly write the interaction Lagrangian in terms of θ_W , g , and e as

$$\mathcal{L}_I = -es^\mu A_\mu - \frac{g}{2\sqrt{2}} [J^{\mu\dagger} W_\mu + J^\mu W_\mu^\dagger] - \frac{g}{\cos \theta_W} [J_3^\mu - \sin^2 \theta_W s^\mu] Z_\mu. \quad (1.17)$$

Limiting the discussion to the electroweak sector, including the quarks in the model is straightforward. The left-handed quarks are introduced as (u, d) doublets that transform under $SU(2)$, the right-handed quarks are singlets. The left-handed quarks have hypercharge $Y = 1/6$. For the right handed quarks, up-type quarks carry $Y = 2/3$ and down-type quarks $Y = -1/3$. The charged-, neutral-, and electromagnetic currents have the same form for quarks as for leptons taking into account the correct electric charges. It should be noted that because the quarks transform under the $SU(3)_c$ group, while the leptons do not, the electroweak sector sees 3 times as many quarks as leptons.

Finally in table 1.1 an overview of the fermions in the standard model with their isospin and hypercharge is shown.

1.2 STERILE NEUTRINOS AND NEUTRINO MASSES

The previous discussion introduces the particles and gauge fields in the standard model and their interactions. It does however not introduce mass terms for the

fermions. A general mass term $m_f \bar{\psi}_f \psi_f$ is not allowed in the Lagrangian as it is not invariant under $SU(2) \times U(1)$ transformations. One can easily see this by decomposing the fields into their helicity states and noting that $\bar{\psi}_R \psi_R = \bar{\psi}_L \psi_L = 0$ which then results in

$$m_f \bar{\psi} \psi = m_f (\bar{\psi}_R \psi_L + \bar{\psi}_L \psi_R) \quad (1.18)$$

The right-handed components however do not transform under $SU(2)$ (they have isospin 0) while the left handed components do as prescribed by eq. (1.2). This means the mass term is not invariant under the gauge group.

The standard model solution to this problem is the introduction of the massive Brout-Englert-Higgs (BEH)-field Φ together with a scalar potential $V(\Phi)$. The field is introduced as a scalar $SU(2)_L$ doublet with complex components and hypercharge $Y = 1/2$

$$\Phi = \begin{pmatrix} \Phi^+ \\ \Phi^0 \end{pmatrix}, \quad V(\Phi) = m^2 \Phi^\dagger \Phi + \lambda (\Phi^\dagger \Phi)^2. \quad (1.19)$$

Due to the shape of the potential term introduced with the field, it has a degenerate non-zero ground state. The doublet therefore gets a specific non-zero vacuum expectation value, that is chosen to give mass to the massive gauge bosons while leaving the photon massless through the interaction terms in the BEH-Lagrangian.

The masses of the fermion fields can be introduced by the Yukawa coupling of the fermion fields to the BEH scalar. Indeed, the triple coupling of the BEH doublet, with a left-handed fermion doublet and a right handed field is renormalizable and gauge-invariant. The non-zero vacuum expectation value then leads to a mass term for the fermion fields. A thorough discussion of the mechanism and Yukawa coupling is found in [11].

The Yukawa coupling terms result in mass terms of the form

$$\mathcal{L} = \bar{\psi}_{Li} M_{ij}^{(u)} \psi_{Rj} + \bar{\psi}_{Li} M_{ij}^{(d)} \psi_{Rj} \quad (1.20)$$

Here the sum runs over particle flavors and the fields ψ are of the same type, i.e. either the upper or lower components of the $SU(2)$ doublets and their corresponding right-handed fields. The mass matrix M_{ij} is determined by the coupling of the scalar field to the fermions and can in general be any square complex matrix.

One sees that in this way the quarks and charged leptons can be given a mass. However the neutrinos remain massless as they lack a right-handed component. To give the neutrino mass we can introduce right-handed neutrinos at this point. Because the right handed neutrino should not interact with any other particle they are $SU(2)$ singlets that carry $Y_W = 0$. This in principle leaves us free to add any number of inactive neutrinos that behave right-handed as they will not show up in the interaction Lagrangian. There is no reason why these inactive (or sterile) neutrinos should be considered as the right handed component of the left handed neutrinos as is the case for the charged leptons.

1.2.1 Dirac mass term

First we shall outline the most conservative case in which we introduce 3 sterile neutrinos, these can then be identified as the right handed components of the left handed active neutrinos and we will therefore denote them as ν_i^R . This leads to a so-called Dirac mass term generated by Yukawa couplings in the same way as the other fermions. The mass term looks like

$$\mathcal{L}_D = M_{Dij} \bar{\nu}_i^R \nu_j^L. \quad (1.21)$$

M_D is a general complex 3×3 matrix in this case. This matrix can be diagonalized with two different unitary matrices V_R and V . The eigenvalues are states with definite mass which are combinations of the sterile and left-handed active neutrinos determined by the matrices V and V_R which we denote as ν_k . The weakly interacting neutrinos ν_{Li} are the left-handed component of a linear combination of the mass eigenstates ν_k through the unitary mixing matrix V_{ik} . As mentioned there is no restriction on the amount of sterile neutrinos one introduces. If we introduce m sterile neutrinos the mass matrix is a general complex matrix.

1.2.2 Majorana mass term

The other most common consideration is a Majorana mass term. To introduce this mass term we first need to introduce the charge conjugation operation C . The charge conjugation connects a particle to its antiparticle state multiplied by an additional phase factor denoted by η_c . For example a neutrino state transforms as

$$C\nu \rightarrow \eta_c \bar{\nu}. \quad (1.22)$$

The charge conjugated state is defined as $(\nu_L)^c = C\nu_L C^{-1} = \eta_c C\bar{\nu}_L$. A possible representation for a C matrix is $C = i\gamma_0\gamma_2$.

One can show that $(\nu_L)^c$ behaves as a right-handed field whilst $(\nu_R)^c$ behaves as a left-handed field. The charge conjugation thus changes a particle to its antiparticle without changing the chirality. From this one can construct a mass term involving only the active neutrinos coupled to their Majorana antiparticles with a mass matrix M_M that can be shown to be symmetric

$$\mathcal{L} = \frac{1}{2} M_{Mij} (\bar{\nu}_{iL})^c \nu_{jL}. \quad (1.23)$$

This type of mass term is unique to neutrinos as it couples particles to their charge conjugate. A Majorana mass term for a charged fermion couples particles to their anti-particles thus breaking the conservation of electric charge. The neutrino, which does not carry an electrical charge, is the only candidate for such a mass term.

Also this coupling does not conserve the weak isospin, or equivalently the lepton number. The term is a product of two doublets under $SU(2)$. The BEH-mechanism

for a single scalar doublet cannot produce such a term. It can however be considered if we assume a triplet representation of the BEH-field which would imply three scalar particles of which one is neutral, one has charge 1 and one has charge 2 [12, 13]. Another mechanism that can produce lepton-number violating mass terms is the model of Zee [14]. By introducing at minimum a scalar singlet with unit hypercharge h^\pm (does not get a non-zero vacuum expectation value), and an additional complex doublet, interactions that break lepton number by 2 units can be considered, leading to a Majorana mass term.

1.2.3 See-saw mechanism

One last mechanism we will introduce is the combination of a Dirac and Majorana mass term. In the most general case, one introduces any number n of sterile right handed neutrinos ν_{iR} . Then the following three mass terms are possible

$$\mathcal{L} = \frac{1}{2} \overline{(\nu_L)^c} M_{Lij} \nu_L + \frac{1}{2} \bar{\nu}_{Ri} M_{Rij} \nu_{Rj} + \bar{\nu}_{Ri} M_{Dij} \nu_{Lj} + h.c \quad (1.24)$$

The first Majorana term is the same as in eq. (1.23) coupling the active neutrinos with their Majorana antiparticle. The same considerations as above apply and this term does not conserve $SU(2)$ symmetry.

The second term mixes the additional sterile neutrinos with their charge conjugate.

The third term is the Dirac mass term originating from Yukawa coupling of the active neutrinos with the right handed sterile neutrinos, which can be either square as in the first case or rectangular if we introduce an arbitrary number of sterile neutrinos.

If we introduce the shorthand notation

$$\Psi_L = \begin{pmatrix} \nu_{eL} \\ \nu_{\mu L} \\ \vdots \\ \nu_{1R} \\ \vdots \\ \nu_{nR} \end{pmatrix}, \quad (\Psi_L)^c = \begin{pmatrix} \nu_{eL}^c \\ \nu_{\mu L}^c \\ \vdots \\ \nu_{1R}^c \\ \vdots \\ \nu_{nR}^c \end{pmatrix} \quad (1.25)$$

where $(\Psi_L)^c$ is the vector obtained by charge conjugation of every element of Ψ_L . Then the mass term can be summarized by

$$\mathcal{L}_M = \bar{\Psi}_L M (\Psi_L)^c + h.c. \quad (1.26)$$

Where M is a square matrix with dimension $n + 3$ when considering 3 active neutrinos and n sterile neutrinos which consists of the matrices M_L , M_R and M_D defined

in the general mass term eq. (1.24). The matrix is structured as the first matrix in eq. (1.27).

$$M = \begin{pmatrix} M_L & M_D \\ M_D^T & M_R \end{pmatrix} \xrightarrow{SU(2) \text{ invariant}} \begin{pmatrix} 0 & M_D \\ M_D^T & M_R \end{pmatrix} \xrightarrow{1R+1L} \begin{pmatrix} 0 & m_D \\ m_D & m_R \end{pmatrix}. \quad (1.27)$$

The second matrix in the above equation is obtained by setting $M_L = 0$ which means we do not allow a mass term coupling the active left handed neutrinos to their charge conjugates.

The third option is obtained when we only consider one neutrino flavor and add a single sterile neutrino. We shall use this last case to illustrate the popular see-saw mechanism [15]. The eigenvalues of the last matrix in eq. (1.27) are

$$m_{\pm} = \frac{1}{2} \left(m_R \pm \sqrt{m_R^2 - 4m_D^2} \right). \quad (1.28)$$

The see-saw mechanism assumes that m_D is situated around the typical MeV scale of the charged leptons, but that the mass scale m_R associated with the sterile neutrinos is very large such that we can approximate the mass eigenvalues by

$$m_{\pm} = \frac{1}{2} \left(m_R \pm m_R \left(1 + \frac{m_D^2}{2m_R^2} \right) \right) \quad (1.29)$$

leading to $m_+ \approx m_R$ and $m_- \approx m_D^2/m_R$.

The two neutrino mass eigenstates then consist of a state with a very small mass, and one with an extremely large mass. This would explain the small masses observed in the neutrino sector. This type of argument can be extended to the more general consideration of an arbitrary amount of sterile neutrinos with 3 active neutrino generations. If the elements of M_R are large in comparison to the masses in M_D and one applies the same prescription one obtains 3 small eigenvalues and n large mass-states.

1.3 NEUTRINO OSCILLATIONS

From the previous discussion we see that the neutrino mass eigenstates (eigenstates of the mass matrix) are not necessarily the neutrino flavor eigenstates. The flavor eigenstate ν_{α} with $\alpha = e, \mu, \tau$ can generally be described by a linear combination of mass eigenstates ν_k

$$|\nu_{\alpha}\rangle = U_{\alpha k}^* |\nu_k\rangle. \quad (1.30)$$

$U_{\alpha k}$ is a general complex matrix describing the mixing of mass states into flavor eigenstates. If we assume that there are three mass eigenstates we get the Pontecorvo-Maki-Nakagawa-Sakata (PMNS) matrix which is unitary.

To illustrate neutrino oscillations we assume a neutrino created in some weak interaction with flavor α . Then the probability of finding a neutrino with weak flavor β after it has traveled a distance L in vacuum is given by

$$|\langle \nu_\beta | \nu_\alpha \rangle|^2 = \delta_{\alpha\beta} - 2\mathcal{R} \left\{ \sum_{k>j} U_{\alpha j} U_{\alpha k}^* U_{\beta j}^* U_{\beta k} \left[1 - \exp \left(-i \frac{\Delta m_{ij}^2}{2E} L \right) \right] \right\}. \quad (1.31)$$

Here $\Delta m_{jk}^2 = m_j^2 - m_k^2$ is the difference between the squared mass of the ν_k . This is under the assumption that the neutrino mass is small such that the energy of a neutrino can be expressed as $E = \sqrt{p^2 + m^2} = p [1 + m^2/(2p^2)]$ where then p is set equal to E to obtain the above formula. One thus sees that neutrino flavor states oscillate over a length L with wave number determined by the fraction $\Delta m^2/E$.

One can understand this result by the following consideration. If we assume a flavor state $|\nu_\alpha(0)\rangle$ being created in some interaction at time $t = 0$ we can write this state as a linear combination of mass eigenstates by using eq. (1.30). It are the mass eigenstates, here labeled by k that will evolve in time as plane waves with energy E_k . The time evolution of the initially pure α state is thus given in terms of the initial mass states by

$$|\nu_\alpha(t)\rangle = U_{\alpha k}^* e^{-iE_k t} |\nu_k\rangle. \quad (1.32)$$

One can again substitute the flavor states, which then gives the transition amplitude of an α state to a β at time t as

$$|\nu_\alpha(t)\rangle = U_{\alpha k}^* e^{-iE_k t} U_{\beta k} |\nu_\beta\rangle = U_{\alpha k} e^{-i \frac{m_k^2}{2E} L} U_{\beta k} |\nu_\beta\rangle \quad (1.33)$$

The second equality is under the assumption that the neutrino masses are small such that $t \approx L$ and $E_k = E [1 + m_k^2/(2E^2)]$. Squaring this amplitude then results in eq. (1.31). The **PMNS** matrix is a three by three unitary matrix, it is most commonly parametrized by 3 angles ($\theta_{12}, \theta_{23}, \theta_{13}$) and 1 complex phase δ_{CP} as

$$U_{PMNS} = \begin{pmatrix} 1 & 0 & 0 \\ 0 & c_{23} & s_{23} \\ 0 & -s_{23} & c_{23} \end{pmatrix} \begin{pmatrix} c_{13} & 0 & s_{13} e^{-i\delta_{CP}} \\ 0 & 0 & 0 \\ -s_{13} e^{i\delta_{CP}} & 0 & s_{13} \end{pmatrix} \begin{pmatrix} c_{12} & s_{12} & 0 \\ -s_{12} & c_{12} & 0 \\ 0 & 0 & 0 \end{pmatrix}. \quad (1.34)$$

Here c_{ij} and s_{ij} are shorthand for $\cos(\theta_{ij})$ and $\sin(\theta_{ij})$ respectively.

The phase δ_{CP} is a source for CP violation. For anti-neutrinos, assuming CPT symmetry the oscillation probability is related to the neutrino oscillation probability by $P(\nu_\alpha \rightarrow \nu_\beta) = P(\bar{\nu}_\beta \rightarrow \bar{\nu}_\alpha)$. By inspection of eq. (1.31) one sees that $P(\nu_\alpha \rightarrow \nu_\beta)$ can be obtained from $P(\nu_\beta \rightarrow \nu_\alpha)$ by considering the complex conjugate of U , i.e. by substituting U for U^* and vice versa in eq. (1.31). For a general complex matrix this means that $P(\nu_\alpha \rightarrow \nu_\beta) \neq P(\nu_\beta \rightarrow \nu_\alpha)$. Which implies CP violation unless δ_{CP} is either 0 or π such that the phase is real.

More explicitly, we get the oscillation probability for anti-neutrinos from 1.31 by complex conjugation of the matrix U , i.e. setting $\delta_{CP} = -\delta_{CP}$. From this one has

$$P(\nu_\alpha \rightarrow \nu_\beta) - P(\bar{\nu}_\alpha \rightarrow \bar{\nu}_\beta) = -16\mathcal{I} \left(U_{\alpha 1} U_{\alpha 2}^* U_{\beta 1}^* U_{\beta 2} \right) \sin \Delta_{12} \sin \Delta_{23} \sin \Delta_{31}. \quad (1.35)$$

Here Δ_{ij} is shorthand for $\frac{\Delta m_{ij}^2 L}{4E}$ and the imaginary part of the product of mixing matrices is proportional to $s_{12}c_{12}s_{23}c_{23}s_{13}c_{13}^2 \sin(\delta_{CP})$ which explicitly shows that there is no CP-violation either if δ_{CP} is 0 or π , or if any of the mixing angles are zero [16].

As a last remark we revisit the parametrization of the PMNS matrix. An arbitrary unitary $N \times N$ matrix can be parametrized by

$$N(N-1) = 2N^2 - N(N-1) - N - N$$

parameters. Where the first term is simply counting the number of real numbers in a complex $N \times N$ matrix, the second term is given by the number of constraints from the columns of the basis having to be an orthonormal basis, the third term is obtained from the constraint that every column should have unit norm, and the last term is a rescaling of the diagonal elements. Of these parameters half are mixing angles, and half are phases¹. In our case of a 3×3 matrix one would therefore expect 3 mixing angles and 3 phases to be required. The PMNS matrix however describes mixing for 3 lepton generations with 3 right handed neutrinos considered to be Dirac particles. This allows to absorb $N-1 = 2$ phases by the redefinition of the 3 mass eigenstates without changing the Lagrangian. If however we assume that neutrinos are Majorana particles the rescaling by a phase factor would affect the mass term as $\nu_i = \bar{\nu}_i$. Therefore the mixing matrix U that can be considered as a more general version of the PMNS matrix, is parametrized as

$$U = U_{PMNS} \begin{pmatrix} e^{i\eta_1} & 0 & 0 \\ 0 & e^{i\eta_2} & 0 \\ 0 & 0 & 0 \end{pmatrix}, \quad (1.36)$$

including the Majorana phases η_1 and η_2 . The Majorana phases should not have an effect on neutrino oscillations [17], the main prospect in determining the nature of neutrinos, be it Majorana or Dirac, is in the observation of double beta decay which would only be possible if neutrinos are Majorana particles [18].

Neutrino mass terms, mass generating mechanisms, and their implications on neutrino oscillations are discussed in [13, 19].

¹ The $SO(3)$ subgroup of real matrices can be parametrized by three angles, while the subgroup consisting of complex diagonal matrices requires 3 phases.

QUASI ELASTIC NEUTRINO SCATTERING

In this section we will give a short overview of Charged-Current Quasi Elastic (CCQE) scattering. Without trying to explicitly calculate any cross sections or matrix elements we shall simply present results and define specific terms. First we will look at CCQE scattering of neutrinos off a free nucleon

$$\nu_l + n \rightarrow p + l,$$

outlining the conventions for the kinematic variables, and highlighting the connection and differences with electron-induced quasi-elastic scattering. Afterwards we discuss the implications of the difficulties arising when scattering from a nucleon bound in the nucleus. The nuclear model [20] based on a mean field generated in the Hartree Fock (HF) approach and which includes long-range correlation effects through the Continuum Random Phase Approximation (CRPA) is briefly discussed. Also an overview of different models that describe the CCQE scattering of neutrinos off the nucleus is given.

2.1 QUASI-ELASTIC SCATTERING ON THE NEUTRON

We shall concern ourselves here with the reaction

$$\nu_l(E_\nu, \mathbf{k}_\nu) + n \rightarrow p + l(E_l, \mathbf{k}_l), \quad (2.1)$$

where a neutrino of flavor l with energy E_ν and three-momentum \mathbf{k}_ν scatters off a neutron through exchange of a charged W^+ -boson, resulting in a proton and charged lepton l in the final state with energy E_l and momentum \mathbf{k}_l . Interaction of an anti-neutrino with the proton resulting in a neutron and anti-lepton in the final state can be considered completely analogously.

The diagram for this interaction is depicted in Fig. 2.1. The standard model of particle physics is based on the interactions of quarks, nucleons could in principle be described by a constituent quark model. The problem is that the strong interaction is non-perturbative at the energy scale of nucleons and we cannot describe the process using quark degrees of freedom. Therefore the effective degrees of freedom of the nucleons are employed and the coupling of the leptons to these nucleons is described in an effective way by introducing form factors.

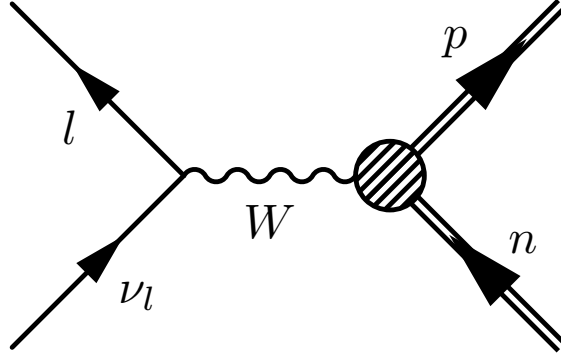


Figure 2.1: Feynman diagram of charged current neutrino-nucleus scattering. The double lines and vertex style indicate that the nucleons are considered as a complicated effective system.

We will consider the inclusive reaction where the initial neutron-, and final proton state are unobserved. We define the energy- and momentum transfer, ω and q respectively, as

$$\omega = E_\nu - E_l \quad (2.2)$$

$$q^2 = (\mathbf{k}_\nu - \mathbf{k}_l)^2 = E_\nu^2 + E_l^2 - m_l^2 - 2E_l E_\nu \sqrt{1 - \frac{m_l^2}{E_l^2}} \cos \theta, \quad (2.3)$$

these are effectively the energy and momentum transferred from the neutrino to the nucleon by the intermediate boson. Additionally the transferred four momentum Q is given by

$$Q^2 = q^2 - \omega^2 \quad (2.4)$$

Here m_l is the lepton mass and $\cos \theta$ the cosine of the scattering angle between \mathbf{k}_ν and \mathbf{k}_l .

The cross section for this reaction is determined from the matrix element \mathcal{M} which consists of a lepton current, completely determined from the standard model Lagrangian, and a hadron current

$$\mathcal{M} = -i \frac{G_F}{\sqrt{2}} V_{ud} \bar{l} \gamma^\mu (1 - \gamma^5) \nu_l J_\mu^{hadron}. \quad (2.5)$$

It is the hadronic current J_μ^{hadron} , which is in principle determined by the distribution of the quarks in hadrons, that is parametrized by form factors. The cross section can be expressed as¹ [21, 22].

$$\frac{\partial \sigma}{\partial Q^2} = \frac{G_F^2 M_p^2 |V_{ud}|^2}{8\pi E_\nu^2} \left(A - \frac{s-u}{M_p^2} B + \frac{(s-u)^2}{M_p^4} C \right). \quad (2.6)$$

¹ The cross section for anti-neutrinos on the proton is the same but the function A has to be multiplied by -1

The cross section is obtained from the four-point Fermi interaction where G_F is the Fermi coupling constant. The factor V_{ud} is the matrix element of the Cabibbo-Kobayashi-Maskawa matrix which describes quark mixing analogously to the Pontecorvo-Maki-Nakagawa-Sakata (PMNS) matrix for neutrino mixing, and M_p is the proton mass. The Mandelstam variables s and u are related to the neutrino energy and the squared four momentum by $s - u = 4M_p E_\nu - Q^2 - m^2$.

The terms A, B , and C are functions of nucleon form factors and Q^2 , explicit forms of the functions will not be given but can be found in [21]. We shall however list and discuss the form factors briefly. The cross section depends on two isovector form factors F_1 and F_2 . The conserved vector current hypothesis [23] relates the isovector form factors to the electric- and magnetic form factors, G_E and G_M respectively. Explicitly we have

$$F_1 = \frac{G_E - \frac{Q^2}{4M_p^2} G_M}{1 - \frac{Q^2}{4} M_p^2}, \quad \zeta F_2 = \frac{G_M - G_E}{1 - \frac{Q^2}{4M_p^2}} \quad (2.7)$$

and the electric- and magnetic form factors are described by a dipole form as

$$G_E = \frac{1}{\left(1 - \frac{Q^2}{M_V^2}\right)^2}, \quad G_M = \frac{1 + \zeta}{\left(1 - \frac{Q^2}{M_V^2}\right)^2} \quad (2.8)$$

where $\zeta = \mu_p - \mu_n$ is related to the magnetic moments of the proton and neutron. The parameter M_V is the vector cut-off mass. The magnetic- and electric form factors are well known from electron scattering on nucleons, an extensive discussion of the form factors of the nucleons can be found in [24].

Two additional form factors appear however when considering neutrino scattering. These are the axial- G_A and pseudo-scalar form factor G_p . The pseudo-scalar form factor enters the cross-section only in terms proportional to m_l^2 / M^2 and is thus often omitted as its contribution to the charged current quasi-elastic cross section is negligible [12]. The axial form factor is, in analogy to G_E , described by a dipole form for low energy transfers as

$$G_A = \frac{g_A}{\left(1 + \frac{Q^2}{M_A^2}\right)^2} \quad (2.9)$$

where M_A is the axial mass and g_A is a normalization factor, also called the axial coupling constant, determined by $G_A(Q^2 = 0)$ which is fixed by β -decay experiments [25]. The axial mass is thus a free parameter in the parametrization of the form factor. Originally measured in experiments where neutrinos are scattered on deuterium thus reducing the nuclear effects to a minimum, it is a major point of interest as experiments on heavier nuclei showed evidence for significantly differing values of the axial mass [26]. A thorough discussion of the axial and pseudo-scalar form factors can be found in [27].

The form factors in their dipole parametrization describe electron scattering well, but in the case of neutrinos other forms are frequently used. An example is the BBBA05 parametrization [28] where the same functional form is used to describe the electric and magnetic form factors which is structured as

$$G(Q^2) = \frac{\sum_{k=0}^2 a_k \left(\frac{Q^2}{4M_N^2}\right)^k}{1 + \sum_{k=0}^4 b_k \left(\frac{Q^2}{4M_N^2}\right)^k} \quad (2.10)$$

the 6 parameters a_k and b_k are specified and obtained by a fit to reproduce scattering data.

2.2 QUASI-ELASTIC SCATTERING OFF THE NUCLEUS

A detailed description of lepton scattering off the nucleus, derivation of the lepton current and definition of nuclear response functions and their relationship to nuclear structure can be found in [29]. Here we will outline some basic ideas and peculiarities, without delving deep into the specific forms of the terms, in a schematic fashion.

When the nucleons are bound in nuclei we consider the inclusive reaction, where the properties of the nucleus and outgoing proton remain unobserved,

$$\nu_l(E_\nu, \mathbf{k}_\nu) + A(N, Z) = X(N-1, Z) + p + l(E_l, \mathbf{k}_l). \quad (2.11)$$

The kinematic variables are the same and in principle the only difference is that in the expression of the matrix element in eq. 2.5 the hadronic current should be replaced by the nuclear current defined by the expectation value of the nuclear current operator taken between the initial and final nuclear states

$$J_\mu^{nuc} = \langle \Psi_f | \hat{J}_\mu^{nuc} | \Psi_i \rangle. \quad (2.12)$$

This parallels the description of quasi-elastic scattering on the nucleus. The nucleus is described as an effective degree of freedom which consists of nucleons that interact in a complex way. In a similar fashion to scattering off the neutron, where the cross section was described by the form factors of the nucleus, we will see that the cross section decomposes in products of factors depending on the lepton kinematics which are well known, and so-called nuclear response functions that contain the nuclear structure effects. When considering a scattering process the structure of the nucleus is completely described by the nuclear current operator. The lepton current can be determined from field theory, and the contraction of the lepton and nuclear tensors determines the cross section. The lepton and nuclear tensors are defined as

$$L_{\mu\nu} = \overline{\sum} \mathcal{J}_\mu^{lep\dagger} \mathcal{J}_\nu^{lep}, \quad (2.13)$$

$$W_{\mu\nu} = \overline{\sum} \mathcal{J}_\mu^{nuc\dagger} \mathcal{J}_\nu^{nuc}, \quad (2.14)$$

where the summation implies summing over the final and averaging over the initial states. This leads to a formal form for the squared matrix element

$$\overline{|\mathcal{M}|^2} = \frac{G_F^2 |V_{ud}|}{2} L_{\mu\nu} W^{\mu\nu} = \frac{G_F^2 |V_{ud}|}{2} \sum_i (v_i R_i) \quad (2.15)$$

where v_i are functions of lepton variables, and the response functions R_i contain the nuclear structure information and depend on the transferred four momentum and four momentum of the nucleus. For exclusive neutrino nucleus scattering one has to consider 10 response functions which together with the kinematic variables determine the exclusive differential cross section. For the inclusive cross section where only the lepton states are observed the amount of response functions is reduced to 5 in neutrino scattering. This can be shown explicitly for example by integrating out the nuclear final states [29].

One needs to consider fewer responses in electron induced quasi-elastic scattering by the conserved vector hypothesis. When one defines the momentum transfer by

$$Q^\mu = \begin{pmatrix} \omega \\ 0 \\ 0 \\ |\mathbf{q}| \end{pmatrix}, \quad (2.16)$$

the conserved vector hypothesis states that

$$q^\mu J_\mu = 0 \Rightarrow J^3 = \frac{\omega}{|\mathbf{q}|} J^0. \quad (2.17)$$

This relates the time-like component of the nuclear current to the third space-like component, and reduces the amount of response functions.

One sees that in the cross section the nuclear responses play a similar role for the nucleus as the form factors of the nuclei. Whereas in the case of nuclei the form factors are relatively well known, and well described in a functional form with a small amount of parameters the nuclear responses are far more complicated. In general a model for neutrino-nucleus scattering has the aim of determining the responses. We will now briefly discuss the partial-wave decomposition technique to illustrate the responses.

2.2.1 Partial wave decomposition

The space-like nuclear current can be decomposed in a spherical basis by expressing its components as

$$\mathcal{J}_\pm = \mp \frac{1}{\sqrt{2}} (\mathcal{J}_1 \pm i\mathcal{J}_2) \quad (2.18)$$

$$\mathcal{J}_3 = \mathcal{J}_3. \quad (2.19)$$

The lepton current for initial state i and final state f can generally be written as

$$\langle f | \mathcal{J}_\mu^{lep}(\mathbf{x}) | i \rangle = l_\mu e^{-i\mathbf{q}\cdot\mathbf{x}} \quad (2.20)$$

and expanded in the same basis [30]. The transition matrix element in momentum space can then be obtained as

$$\mathcal{M} = \frac{G_F}{\sqrt{2}} \int d^3x e^{-i\mathbf{q}\cdot\mathbf{x}} l_\mu \langle f | \hat{J}_\mu^{nuc}(\mathbf{x}) | i \rangle. \quad (2.21)$$

The integrand can be expanded in a multipole series and projected on irreducible tensor operators as described in [29]. The matrix element is then described as an infinite series of expectation values of multipole operators, the sum running over the multipole moment J of the operators. As the terms are tensor operators in the spherical basis, the Wigner-Eckart theorem can be used which states that the expectation value of any tensor operator \mathcal{O}_{JM}

$$\langle J_f M_f | \mathcal{O}_{JM} | J_i M_i \rangle = (-1)^{J_f - M_f} \begin{pmatrix} J_f & J & J_i \\ -M_f & M & M_i \end{pmatrix} \langle J_f || \mathcal{O}_J || J_i \rangle, \quad (2.22)$$

can be written as the product of a combinatorial factor depending on the coupling of the initial and final angular momentum J, M and a reduced matrix element. With this decomposition, one can show explicitly that when averaging over the initial and summing over the final states the orthogonality of combinatorial factors reduces the amount of response functions to 5 for inclusive cross sections. The cross section is then given as the sum over kinematic factors and the response functions which are completely determined by the expectation values of tensor operators.

Some additional structure becomes clear when decomposing the matrix element as such. The current is decomposed into projections onto the so called Coulomb $\hat{\mathcal{M}}_J$, longitudinal $\hat{\mathcal{L}}_J$ and transverse operators $\hat{\mathcal{J}}^{mag}$ and $\hat{\mathcal{J}}^{el}$. In the case of electron scattering there is no longitudinal projection because of the conserved vector current hypothesis.

Further there is interference between the Coulomb and longitudinal terms and separately between the two transverse terms, but the Coulomb Longitudinal (CL) part does not interfere with the transverse part. The same is true for electron scattering, but in electron scattering there is no interference between the two transverse terms².

Formally the cross section can now be written as

$$\frac{\partial^2 \sigma}{\partial \omega \partial \Omega} = \frac{G_F |V_{ud}|^2}{16\pi^2} \left(\frac{2}{2J_i + 1} \right) E_l k_l \left(\sum_{J=0}^{\infty} \sigma_{CL}^J + \sum_{J=1}^{\infty} \sigma_T^J \right). \quad (2.23)$$

The combinatorial factor is due to the averaging over the initial states. The summation over multipoles can be truncated at some point, the summation is shown to

² The electron induced cross section consists of 2 response functions determined by a Coulomb and 2 transverse operators. These tensor operators have analogous structure as the ones for neutrino scattering but are defined differently [29]

converge [31] and can be cut off at some value of J . At larger energies more multipole moments need to be taken into account.

For completeness we write the CL and transverse part explicitly in terms of the operators $\widehat{\mathcal{M}}_J$, $\widehat{\mathcal{L}}_J$, $\widehat{\mathcal{J}}^{mag}$ and $\widehat{\mathcal{J}}^{el}$. First the cross section is decomposed as a sum of the 5 response functions along with their corresponding kinematic factors v

$$\sigma_{CL}^J = v^{\mathcal{M}} R^{\mathcal{M}} + v^{\mathcal{L}} R^{\mathcal{L}} + 2v^{\mathcal{ML}} R^{\mathcal{ML}} \quad (2.24)$$

$$\sigma_T^J = v_T R^T \pm 2v^{TT} R^{TT}. \quad (2.25)$$

The response functions are defined in terms of expectation values of the multipole operators as

$$R^{\mathcal{M}} = |\langle J_f | \widehat{\mathcal{M}}_J | J_i \rangle|^2, \quad (2.26)$$

$$R^{\mathcal{L}} = |\langle J_f | \widehat{\mathcal{L}}_J | J_i \rangle|^2, \quad (2.27)$$

$$R^{\mathcal{ML}} = \mathcal{R} \left(\langle J_f | \widehat{\mathcal{L}}_J | J_i \rangle \langle J_f | \widehat{\mathcal{M}}_J | J_i \rangle^* \right), \quad (2.28)$$

$$R^T = |\langle J_f | \widehat{\mathcal{J}}^{el}_J | J_i \rangle|^2 + |\langle J_f | \widehat{\mathcal{J}}^{mag}_J | J_i \rangle|^2, \quad (2.29)$$

$$R^{TT} = \mathcal{R} \left(\langle J_f | \widehat{\mathcal{J}}^{mag}_J | J_i \rangle \langle J_f | \widehat{\mathcal{J}}^{el}_J | J_i \rangle^* \right). \quad (2.30)$$

The exact definition of the multipole operators can be found [29, 30, 32].

The only difference between neutrino and anti-neutrino cross sections is due to the sign of the transverse interference term \mathcal{R}^{TT} . The CL terms will dominate the cross section at forward scattering angles, while for backward scattering mainly the transverse currents contribute.

2.3 MODELING QUASI-ELASTIC NEUTRINO-NUCLEUS SCATTERING

A model that describes the neutrino-nucleus cross section contains in principle two fundamental ingredients, the nuclear currents which we described in the previous section, and the nuclear wavefunctions.

Before discussing a number of different models for the nucleus we first mention the very common Impulse Approximation (IA). Then we will mention some prominent models that aim to describe the nucleus.

2.3.1 Impulse Approximation

The impulse approximation is the simplest and most widely used approximation when dealing with nuclear currents in CCQE scattering. In the IA the nuclear current for a nucleus with mass number A is treated as the sum of A one-body currents which are simply the hadron currents that appear in eq. (2.5). The IA seems to be a natural way of implementing the nuclear current for CCQE scattering as the emitted nucleon is assumed to absorb most of the energy and momentum in order to be knocked out of the nucleus while the residual nucleus is left behind in a pure

hole state. This nuclear current implemented in an independent particle model then describes the interaction of an initial state bound nucleon with a quasi-free outgoing nucleon without taking any nuclear effects beyond the mean field into consideration. The omitted effects can be corrected by meson-exchange currents (MEC), short-range correlations (SRCs), and long-range correlations (for example through the RPA) which are included in the nuclear currents.

Explicitly the one-nucleon current for neutrino induced CC scattering is

$$\bar{u}\hat{f}^\mu u = \bar{u} \left(F_1^V \gamma^\mu + \frac{i}{2M} F_2^V \sigma_{\mu\nu} q^\nu + G_A \gamma^\mu \gamma^5 + G_p q^\mu \gamma_5 \right) u \quad (2.31)$$

The form factors F_1, F_2 and G_A have been previously discussed. The term proportional to G_p , the pseudo-scalar form factor, is usually taken into account even though it does not contribute significantly to the description of the process. The expectation value of the operator is considered between the Dirac spinors u . Different forms are possible for the one-nucleon current, but they are always parametrized according to nucleon form factors as shown. Different forms are equivalent, when considering free nucleons, however when they are bound in the nucleus, different forms of the current do not necessarily produce identical results [33].

2.3.2 Nuclear structure

Up to this point we have discussed the structure of the cross-section and the nuclear currents. The second ingredient needed to calculate the nuclear responses is the description of the initial and final nuclear states.

A common approach is the independent particle model where the initial wave function is described as a single nucleon moving independently of the other nucleons in the nucleus. As the simplest example we mention the Fermi gas model where the nucleons are plane waves with definite binding energy and momentum below the Fermi momentum. These parameters can be optimized to reproduce the data for a certain nucleus.

The local Fermi gas model is analogous, but the momentum and binding energy are determined by the distance from the nuclear core.

A different type of independent particle model, the mean field approach, considers the initial nucleon in a potential that is in principle generated by the interaction with other nucleons. The choice of potential is crucial and we mention two different methods. In one approach the potential is an analytic functional form such as the phenomenological Woods-Saxon potential.

In another approach the mean field potential is generated by an (iterative) method such as the well known HF approximation. The HF mean field can be determined from a nucleon-nucleon potential, which describes the interaction between two nuclei. The nucleon-nucleon interaction however is not well known, and many different forms are possible. The relevant components of the nucleon-nucleon force can be fitted to experimental data to produce a phenomenological interaction such as

the extended Skyrme interaction [34–36]. The nucleon state in a mean field method is generally described as combinations of the energy eigenfunctions of the single-particle potential, the energies of the nucleons are called the single-particle energies.

Consideration should also be given to the description of the outgoing nucleon. In the plane wave (impulse) approximation the outgoing nucleon is simply a plane wave with definite momentum and energy. When the plane wave approximation is coupled to the impulse approximation one considers a single nucleon absorbing all the energy in a one-step process which is then completely free. In this case the responses simplify, the process is in principle completely analogous to scattering off a single nucleon, with exception of the initial state of the nucleon.

In more realistic models however the outgoing nucleon should be able to interact with the nuclear medium, as the struck nucleon has to make its way out of the nucleus. A simple approximation, dubbed the spectator approach, describes the outgoing nucleon under the influence of the (mean field) potential of the residual $(A - 1)$ -body system.

2.3.3 Modern descriptions of neutrino-nucleus scattering

We mention some modern approaches that aim to describe (quasi-elastic) neutrino-nucleus scattering for E_ν ranging from a couple 100 MeV to a couple GeV.

- The model of Martini et al. [37–40] describes the nucleus by a local relativistic Fermi gas. Multinucleon excitations are taken into account by introduction of meson-exchange currents. The nucleon-nucleon force can be understood in an effective way by the exchange of light mesons. The three-point nucleon-nucleon- W boson vertex considered in the impulse approximation is then extended with diagrams where nucleons couple through the exchange of these mesons.

The Δ excitation of the nucleons is also considered in the particle-hole propagator. The model includes long-range correlations between nucleons in the Random Phase Approximation. The RPA treatment of the currents is used to "dress" the bare ph -propagator, by including a sum of higher order ph -diagrams that are coupled through interactions. Leading to a self-consistent equation from which the dressed propagator can be obtained from the bare propagator and the interaction potential. This treatment then also mixes the multi-nucleon and Δ -excitations contributions into the pure $1p1h$ responses as illustrated in Fig. 2.2.

We also mention the prominent model of Nieves et al. [41–43] which can be considered similar.

- In the approach of Benhar et al. [44, 45] the transition matrix elements are obtained from a spectral-function formalism, determining the removal proba-

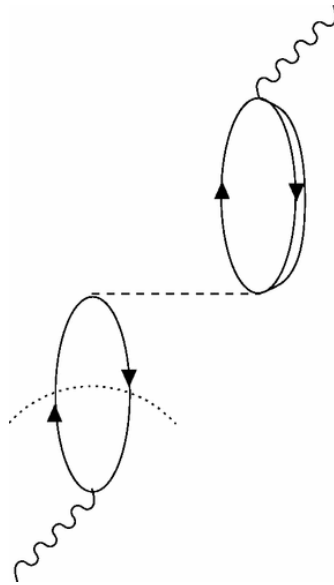


Figure 2.2: Figure from [37] showing the lowest order contribution of the Δ -excitation on the RPA-propagator. The wiggle represents the external W -boson. The single lines are particle, or hole propagators. The bare particle-hole propagator, can be represented by looking at the bottom part of the diagram until one reaches the dotted line. The RPA couples the bare particle hole propagator with in this case a delta excitation (double line), through the nucleon-nucleon interaction represented by the dashed line. The dotted line shows where the particle-hole are placed on-shell to obtain a single nucleon knock-out reaction.

bility of a nucleon for certain energy-momentum distributions of the nucleus, as described in [46, 47].

- The Super Scaling Approach, or SuSA for short, uses scaling properties of cross sections measured in electron-nucleus scattering to determine neutrino cross sections [48]. The scaling ansatz states that a universal scaling-function can be used to determine the cross section instead of the spectral function. The scaling function is obtained by dividing the cross section by the single nucleon part. The idea of *type-1 scaling* is that a universal scaling function can be found for different kinematic regions. *Type-2 scaling* uses a universal scaling function for different nuclei. When first- and second-kind scaling occur, one speaks of superscaling [49]. The phenomenological super-scaling function includes long- and short-range correlations [48]. The multinucleon contributions, and MEC were included in [50].
- The GiBUU model treats final-state interactions by transport of nucleons through the nuclear medium [51]. It is used in neutrino CCQE scattering, where the nucleus is described in a density-dependent mean field [52]. The reaction is then described as a two-step process, initial absorption of all energy by a single nucleon, which is then transported out of the nucleus.

2.3.3.1 The HF and CRPA models

The model(s) we will extensively use in this work, and refer to as HF and CRPA, were developed in the Ghent nuclear physics group. The model for CCQE neutrino-nucleus scattering is described in [20].

The reaction is modeled with an independent particle model in which the nucleus is treated in the mean field approach. The mean field potential is determined from the HF approximation, using an effective nucleon-nucleon interaction of the Skyrme type, the extended Skyrme force (SkE) [34–36, 53]. The outgoing nucleon wave function is treated as a mean field continuum state to account for interactions with the residual nucleus.

The CRPA approximation allows to treat long range correlations of the nucleons [53, 54]. The potential used in the expansion of the propagator is the same SkE force used to generate the mean field. This leads to a consistent model, in which the Giant Resonance (GR) region³ can be taken into account. The CRPA formalism, in the Greens function approach, is considered in coordinate space, this allows to treat the continuum in an exact way. The final-state wave function is constructed as a combination of bound and continuum states, which have the correct asymptotic behavior.

³ GR are collective excitations of the nucleus as a whole

The cross section is treated analogously as in eq. (2.23), explicitly it is computed as

$$\frac{d^2\sigma}{d\omega d\Omega} = \frac{G_F|V_{ud}|^2}{16\pi^2} \left(\frac{2}{2J_i + 1} \right) E_l k_l \xi^2(Z, E_l, q) \left(\sum_{J=0}^{\infty} \sigma_{CL}^J + \sum_{J=1}^{\infty} \sigma_T^J \right). \quad (2.32)$$

In addition to the HF+CRPA formalism described above, additional modifications are made to the cross-section. These include the effective momentum approximation for the final state lepton, folding of the responses with a Lorentzian do account for spreading width of the final state nucleon, and effective relativistic corrections. These modifications are described in [10]. We will briefly touch upon illustrate these modifications.

An additional factor $\xi^2(Z, E, q)$ is introduced. It takes into account distortion of the final-state lepton wave function in the Coulomb field of the residual nucleus in the modified effective momentum approximation [55].

The position of the GR peaks are well described in the CRPA approach, but as the states are described in terms of ph states, the spreading width of the final state nucleon is not accounted for. To reduce the height, and increase the width of the resonance peaks, a folding procedure may be implemented. The individual responses $R(\omega, q)$ are folded with a Lorentzian with a width of $\Gamma = 3$ MeV.

$$R'(q, \omega') = \int d\omega R(q, \omega) \times \frac{1}{2\pi} \left[\frac{\Gamma}{(\omega - \omega')^2 + (\Gamma/2)^2} \right]. \quad (2.33)$$

The energy integrated responses are however not affected by the procedure.

The non-relativistic description of the nucleus requires modifications when considering higher momentum transfers, as the transferred momentum becomes comparable to the nucleon mass. A semi-relativistic correction is obtained by substituting

$$\frac{\omega}{2M_N} \rightarrow \frac{\omega}{2M_N} \left(1 + \frac{\omega}{2M_N} \right)$$

In this way the quasi-elastic peak is shifted towards smaller values of ω .

NEUTRINO EXPERIMENTS

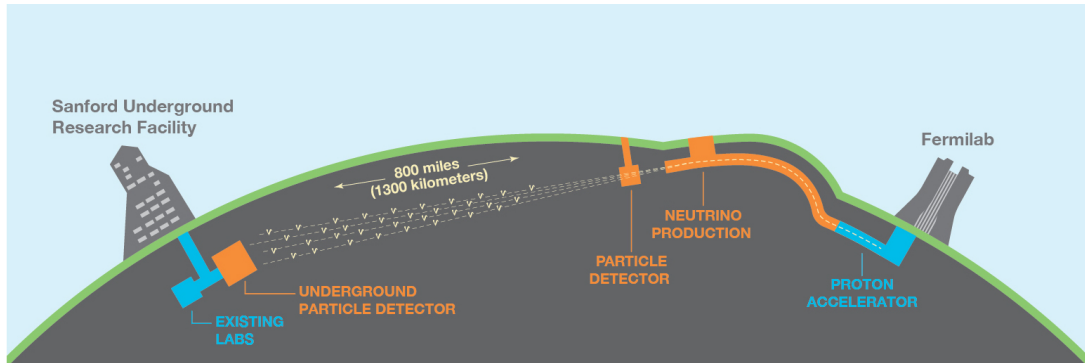


Figure 3.1: Overview of the [DUNE](#) [56], a long-baseline accelerator based neutrino experiment.

The discovery of neutrino oscillations, for which the Sudbury neutrino observatory (SNO) [6] and Super-Kamiokande [7] experiments were awarded a Nobel prize in 2015, has spawned a vast number of experiments with the goal of determining the nature of neutrino mixing. These experiments respectively used solar- and atmospheric neutrinos as incoming particles. The neutrino flux $\Phi(E_\nu)$, and traveled distance L were thus fixed. The current generation of accelerator based neutrino experiments uses neutrino beams originating from high energy protons incident on a nuclear target, producing charged mesons which subsequently decay resulting in a beam of neutrinos. In this way $\Phi(E_\nu)$, and L can be optimized for oscillation experiments. We shall firstly give a short overview of the neutrino beamlines, detection mechanisms and experiments. Afterwards we will focus deeper on the Miniature Booster Neutrino Experiment ([MiniBooNE](#)) experiment in order to give concrete examples.

3.1 NEUTRINO BEAMS

There are many neutrino sources for experiments. "Natural" sources, such as the aforementioned solar-, atmospheric-, but also including other astrophysical sources such as supernova neutrinos are being studied.

Solar neutrinos, which originate from the nuclear fusion in the sun, are a source of low-energy neutrinos. The neutrino flux is dependent on the solar model, the flux predictions by Bahcall [5], are shown in Fig. 3.2. The dominant contribution is due to the pp reaction where two protons fuse to form deuteron, with emission of a positron and electron neutrino. The neutrino energy spectrum from pp however

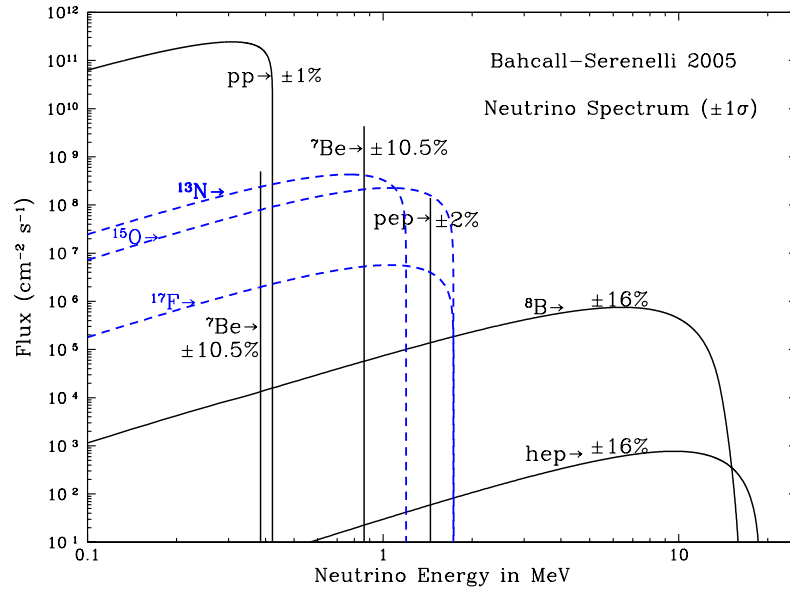


Figure 3.2: Prediction of the neutrino flux due to different fusion processes from the sun, figure from Bahcall [5].

is cut off at around 500 keV, which is too low to detect. Other reactions produce neutrinos with energies up to about 15 MeV, detectable by the Čerenkov detectors used in the [SNO](#) and Kamiokande experiments, or the chemical detectors such as the chlorine detector in the Homestake experiment [4].

Atmospheric neutrinos are created in air showers, where high energy cosmic rays, usually protons, from astrophysical sources scatter on the atmosphere, this produces an array of particles, which further react and decay. Creation of pions and other charged mesons which subsequently decay into leptons and neutrinos are the main source of neutrinos from air-showers. The neutrino energies have a vast spread over several orders of magnitude of GeV.

The astrophysical sources of neutrinos are supernova explosions, and other astrophysical processes where particles react at high energies to produce neutrinos that find their way to the earth. Studying these neutrinos opens a new window on astrophysics, and the experiments are often called neutrino telescopes.

In addition anti-neutrinos originating from nuclear reactors, through the β -decay of the neutron rich fission products, are a source of low-energy (couple of MeV) neutrinos from which neutrino oscillations are studied in disappearance experiments. The energy of the (oscillated) neutrinos is too low to produce muons or τ -leptons,

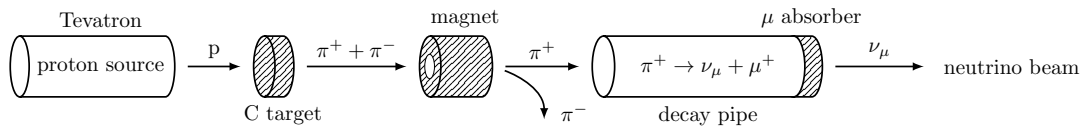


Figure 3.3: Schematic depiction of the neutrino beam production at NuMI

and measurements are done of the disappearance of electron neutrinos from the reactor core [57].

We shall here outline accelerator-based neutrino beams where high energy protons from an accelerator are used to produce neutrinos with energies ranging from hundreds of MeV to several GeV.

The basic mechanism in production of a neutrino beam is as follows. An accelerator provides high energy protons which are directed into a nuclear target (common targets are carbon, beryllium, and aluminum). The hadronic interactions between the protons and the target material produce mainly pions, and other charged mesons. The resulting charged mesons are directed to a decay pipe by electromagnetic devices, named focusing horns. These horns focus the beam and make it possible to select mesons based on their charge. In the decay region the prominent pions decay primarily into muons and muon neutrinos. Depending on the selected charge of the pions (π^+ or π^-), the resulting beam is composed mainly of ν_μ or $\bar{\nu}_\mu$, respectively. The particles other than neutrinos are stopped at the end of the decay region [8].

Each of these steps has to be described by Monte-Carlo simulations to predict the produced neutrino flux. The simulations are sensitive to the material and geometry of the components, as well as the description of hadronic and electromagnetic interactions of the particles in the beam. The main uncertainties in the flux predictions are due to the description of the hadronic interactions of incident protons with the target material.

A simple example of a source of background in a ν_μ beam is the production of kaons, that produce ν_μ with higher energies in comparison to the pions, and can also contribute to the ν_e flux. The amount of muons and kaons, along with their energy distributions should thus be determined by simulation of interactions of incident p with the target material. Also of interest is that the detector is not always positioned directly on the axis of the neutrino beam. A slightly off-axis position leads to a smaller flux which is however peaked in a more narrow, specific energy region. Listed are some of the most prominent neutrino beamlines.

- The Booster Neutrino Beamline (BNB) delivers 8 GeV protons produced by the booster synchrotron at Fermi National Accelerator Laboratory (FNAL) to a beryllium target. The average energy of the resulting ν_μ beam is approximately 800 MeV. The target is embedded in a pulsed electromagnet (the horn) producing a magnetic field to focus either positive or negative particles [8].

- The *NuMI* neutrino beam, also located at *FNAL*, uses protons of about 120 GeV, incident on a graphite target. The charged mesons are subsequently focused by 2 magnetic horns [58]. By specific configurations of the focusing horns, different neutrino energy regimes are accessible, dubbed the Low Energy (LE), Medium Energy (ME), and High Energy (ME) configurations. The neutrino flux in the low energy configuration is peaked at an energy of 3.5 GeV with high energy tails extending to tens of GeV [59]. The flux predictions are shown in Fig. 3-4.
- *J-PARC* creates a neutrino beam as described above, with the additional feature of allowing a fraction of muons to exit the decay region. These muons can then be monitored, and utilized as a feedback mechanism for the simulations in order to make better flux predictions [60]. The neutrino beam also features 2 near detectors: INGRID monitors the direction and intensity of the beam [61], and ND280 (located slightly off axis) measures the neutrino spectrum and contamination with electron neutrinos which is of importance in oscillation experiments [62].

3.2 DETECTORS

Simply stated there are three main types of detectors in use in accelerator based experiments,

- *Čerenkov detectors* (*MiniBooNE* [63], Tokai-to-Kamiokande (*T2K*) far detector [64]) consist of a tank filled with a liquid (mineral oil and heavy water respectively). The experiments detect the final state lepton of an interaction by the emission of Čerenkov light as it passes through the medium if its kinetic energy is sufficient. The outgoing particles that are below the threshold are not detected. The Charged-Current Quasi Elastic (*CCQE*) reaction channel is then usually defined as an event where a single outgoing lepton is observed and thus includes multi-nucleon knock out reactions as well. Differentiation can be made between final state electrons and muons as there Čerenkov light is different.
- In Liquid Argon Time Projection Chamber (*LArTPC*) detectors (*ArgoNeut* [65], *MicroBooNE* [66]) a neutrino enters a chamber filled with liquid argon where it can interact with an argon nucleus thus producing charged particles. The particles are guided by electric fields to wires where they can be detected. This, combined with calorimetric energy reconstruction and precise particle identification in principle, allows full reconstruction of the event including all final state charged particles [67].
- *Scintillation detectors* (*Minerva* [68], *T2K* near detector [62]) consist of an array of scintillator strips connected to photomultiplier tubes. Charged particles excite the scintillator material which re-emits the absorbed energy as light. The

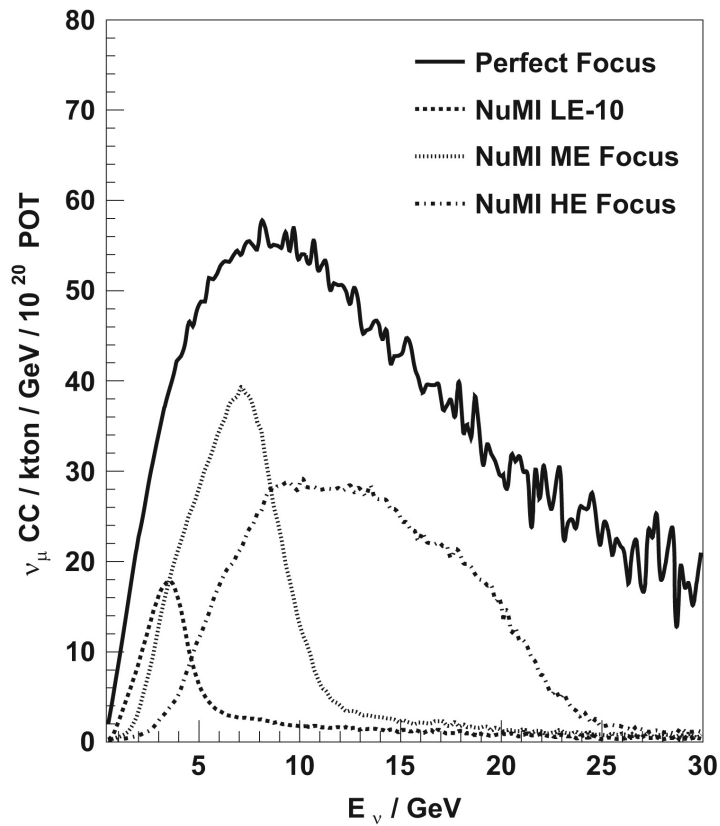


Figure 3.4: Shown is the event rate (flux \times cross-section) as a function of neutrino energy at the Soudan mine in Minnesota for different horn configurations. The solid black line shows the “perfect” focusing, and the dotted lines show the actual focusing for different NuMI beam configurations. The three different beam configurations correspond to the true low energy (LE), medium energy (ME), and high energy (HE) beam configurations. Figure from [58].

Table 3.1: Selected accelerator based experiments that measure the neutrino-nucleus cross section

Experiment	neutrino beam ($\langle E_\nu \rangle$ in GeV)	detector type
ArgoNeut [†]	NuMI (4.3)	LArTPC
MicroBooNE	BNB (0.8)	LArTPC
Minerva	NuMI (3.5 (LE), 5.5 (ME))	scintillator detector with, He, CH, H ₂ O, Fe, Pb
MiniBooNE [†]	BNB (0.8)	(CH ₂) Čerenkov
MINOS	NuMI (3.5)	Fe
NOMAD [†]	NuMI (23.4)	C
Nova	off-axis NuMI (2)	CH ₂ scintillator
SciBooNE [†]	BNB (0.8)	CH scintillator
T2K	off-axis J-Parc (0.6)	H ₂ O Čerenkov (FD), CH scintillator (ND)

photomultiplier tubes convert the light to an electrical signal which allows 3D-reconstruction of all outgoing charged particles by the geometry of the strips.

Each of these detectors uses nuclear targets to detect the neutrino, nuclear targets naturally have a larger cross sections, but the downside of using heavy nuclei is that non-trivial modeling of the relevant reaction mechanisms, such as CCQE scattering, and the backgrounds is necessary in order to interpret the results. But this also means that these neutrino experiments provide data of neutrino-nucleus scattering processes which is crucial to understanding the weak nuclear structure.

3.3 EXPERIMENTS

A comprehensive list of past, present, and future neutrino experiments of all sorts is maintained at [69]. We shall focus mainly on experiments that study neutrino oscillations, and specifically on accelerator based experiments that are sensitive to, and have measured, the (CCQE) neutrino-nucleus scattering cross section. An overview of selected experiments and their characteristics is given in table 3.1.

The experiments marked by a [†] superscript, are not actively running anymore¹. Of these experiments, the most famous is T2K, making use of the J-Parc neutrino beam [60], and 2 off-axis detectors, the Near Detector ND280 is a scintillation detector used to monitor the beam before oscillations [62], while the FD is the famous Super-Kamiokande detector, a Čerenkov detector filled with heavy water located in the

¹ ArgoNeuT, MiniBooNe, NOMAD, and SciBooNE stopped taking data in 2010, 2012, 1998, and 2008 respectively

Kamioka mine in Japan 295 km away from the beam source [64]. The intensity, and direction of the beam is monitored by the Interactive Neutrino GRID detector [61]

Another experiment using the off-axis detector geometry is *Nova*, using a near- and far-detector which are both liquid scintillators filled with CH as a nuclear target. Neutrinos travel from the near detector at *FNAL*, to the far detector located in Minnesota. The off-axis placement allows to use the *NuMI* beam in the ME configuration, which on-axis is broadly peaked around ≈ 7 GeV as seen in Fig. 3.4, to obtain a flux peaked sharply around 2 GeV [70].

The different experiments, and their influence on the description of *CCQE* scattering and neutrino oscillations, are described in [21, 71]. We shall here only present the *MiniBooNE* experiment in some additional detail in order to contextualize further discussion of the results.

3.3.1 *MiniBooNE*

The *MiniBooNE* experiment, located at the *FNAL*, utilizes the *BNB* and a mineral oil (CH_2) Čerenkov detector to detect neutrinos. *MiniBooNE* was built to study the short baseline neutrino oscillation signal, appearance of $\bar{\nu}_e$ in a $\bar{\nu}_\mu$ beam, indicated by *LSND* [72]. The *LSND* experiment was accelerator-based, with a baseline $L \approx 30$ m and mean neutrino energy of around 30 MeV, while the *MiniBooNE* flux is peaked around half a GeV with a baseline $L \approx 550$ m in order to study the same L/E region but in a very different energy region leading to different backgrounds and systematics [63].

Unlike most other oscillation experiments, *MiniBooNE* features a single detector, instead of using a separate near- and far detector to analyze the (un)oscillated flux. The experiment is thus very dependent on accurate determination of the relevant cross-sections for ν_μ and ν_e , and simulation of the expected backgrounds [71]. This means that in order to study the oscillation signal, the first measurements of flux integrated (double-differential) *CCQE* cross-sections of (anti-)neutrinos on ^{12}C were made [26, 73, 74]. In addition to the flux-integrated double differential cross sections, the reconstructed, and extracted cross sections are also presented.

In the Čerenkov detector, an event is considered as *CCQE*, if there is a single lepton, and no pion, found in the final state. The lepton type can be determined, but any sub-threshold reaction products are invisible in the analysis. One thus in principle sets out to measure the inclusive *CCQE* scattering cross section, however the measurements required additional contributions from processes where more than one nucleon was knocked out, indistinguishable from the genuine quasi-elastic contribution in the detector [37, 38]. This led to these events to be dubbed "*CCQE-like*" in order to distinguish them from genuine quasi-elastic events.

It was found that the (unfolded) cross-sections seemed to conform to a simple Relativistic Fermi Gas (*RFG*) prediction with an effective $M_A \approx 1.25$ GeV which does not conform with the world-average of $M_A = 1.03 \pm 0.02$ GeV, the discrepancies could however be explained by including long range RPA, and multi-nucleon knock-

out contributions without having to change the axial mass of the nucleon [37, 75]. The unexpectedly high quasi-elastic cross section in comparison to a Fermi gas thus shows that nuclear effects are crucial at understanding the neutrino-nucleus scattering mechanism, and oscillation signals at the few-GeV scale. A model should in principle contain, apart from the bare quasi-elastic contribution, the effects of short range correlations, RPA, Meson-exchange currents and final-state interactions in order to describe the data.

The main non-quasi elastic background in the detector is production of charged pions which are subsequently absorbed by the nucleus resulting in the same final state as the CCQE reaction. This background is estimated from Monte-Carlo predictions, with an input based on the measurement of events where the pion is visible in the final state. Therefore the neutrino-induced (charged) pion production cross section is measured by MiniBooNE as well [76, 77].

ENERGY RECONSTRUCTION

As explained in the previous chapter neutrino beams are produced through the leptonic decay of charged mesons produced by bombarding a target with high energy protons. The pions can be separated by their charge, and subsequent decay results in charged leptons and neutrinos, these neutrinos are sent through the earth towards the detector. This results in a beam of neutrinos with varying energies, even in off-axis geometries where the flux is significantly peaked around a certain energy, compared to the on-axis geometry, there is still a significant spread in the flux.

The measurable quantities in a quasi-elastic scattering event in a Čerenkov detector are the energy and scattering angle of the outgoing lepton. From these kinematic variables the energy of the incoming neutrino is reconstructed. We first explain the method of energy reconstruction used by Miniature Booster Neutrino Experiment (MiniBooNE) and Tokai-to-Kamiokande (T2K) [9, 78]. We then discuss why an accurate reconstructed energy is necessary and briefly highlight some research done on the topic. We explore the implications of the reconstruction procedure by comparing with theoretical distributions of incoming neutrino energies for several sets of lepton kinematic variables.

4.1 QUASI-ELASTIC ENERGY RECONSTRUCTION

The reconstructed energy for an event characterized by the kinematic variables of the outgoing lepton, its scattering angle θ and energy E_l , is based on the incoming energy in quasi-elastic scattering of a neutrino off a free neutron at rest. The energy transfer $\omega = E_\nu - E_l$, and momentum transfer $q^2 = E_\nu^2 + P_l^2 - 2E_\nu P_l \cos \theta$ are then related by $\omega = \frac{q^2 - \omega^2}{2M_n}$ where P_l is the lepton momentum and M_n is the neutron mass. From this one finds:

$$\bar{E}_\nu = \frac{E_l - m_l^2 / (2M_n)}{1 - (E_l - P_l \cos \theta) / M_n}. \quad (4.1)$$

Introducing a binding correction in this formula can be done using

$$\bar{E}_\nu = \frac{2M'_n E_l - ((M'_n)^2 + m_l^2 - M_p^2)}{2(M'_n - E_l + P_l \cos \theta)} \quad (4.2)$$

Where $M'_n = M_n - E_B$ is the adjusted neutron mass depending on the chosen separation energy E_B . M_p is the proton mass [9]. The second expression is equal to the former when omitting the binding energy in the adjustment of the neutron mass and setting $M_n = M_p$. This reconstructed energy is the energy of a neutrino that scatters

with an energy transfer on the quasi-elastic peak when the neutron separation energy is E_b . Nuclear effects are neglected in this consideration, and the reconstructed value can be tuned through the separation energy.

The reconstructed energy \bar{E}_ν is a simple definition, which is model independent as all the parameters are well defined. Therefore it is possible to calculate the amount of events in bins of reconstructed energies using the predicted flux and cross-section. In this way one can compare a model with data in reconstructed bins. The reconstruction procedure as described is then perfectly valid as long as the predicted events from an (oscillation) model are expressed in terms of the well defined reconstructed energy. This method of comparing predictions with data does however always involve the smearing of energy distributions with the predicted flux.

In order to study neutrino-oscillations (and neutrino cross sections) in a more direct way, one may wish to accurately reconstruct the energy of an event. This procedure involves calculating back from the measured data, in bins of reconstructed energy, to distributions of real neutrino energies. This process is called unfolding, and the resulting distributions are expressed in terms of the unfolded energy E_ν^{uf} . The unfolded energy distribution is determined by redistributing the data in bins of reconstructed energy into unfolded energy bins. This procedure however is dependent on the model used to predict the amount of events in bins of reconstructed energy, determining the relation between unfolded and reconstructed bins.

The reconstruction procedure was analyzed in [79] and it was shown that multi-nucleon knockout processes, which have proven crucial in explaining the high cross sections measured by MiniBooNE [26, 73], have a large effect on distributions of reconstructed energies. An inclusive multi-nucleon event with certain outgoing lepton angle and energy is more likely due to a neutrino with higher energy compared to a pure quasi-elastic event as the larger transferred energy is carried by more nucleons. This leads to an enhancement of the cross-section in bins of certain reconstructed energies due to far larger real energies.

The unfolding procedure uses predictions of the flux-folded cross section in terms of reconstructed- and true energies to redistribute events from bins of \bar{E}_ν to E_ν^{uf} . The MiniBooNE experiment, uses a Relativistic Fermi Gas (RFG) model for this prediction [26, 73]. The procedure was examined by reproducing the data unfolding as closely as possible, and using it to unfold data based on a model of the cross section that includes multi-nucleon knock out and RPA. This prediction in terms of E_ν^{uf} could then be directly compared to the MiniBooNE unfolded data. This showed that multi-nucleon processes could be taken into account to accurately reproduce the measured data [80].

The influence of multi-nucleon events on neutrino oscillation analysis has also been by looking at predictions in terms of reconstructed energies [81].

The accuracy of the unfolded quasi elastic cross section depends on how well nuclear effects such as stuck-pion events, multi-nucleon knockout, RPA etc. can be predicted. The reconstruction procedure was examined in [82] in a Monte-Carlo simulation using the GiBUU transport model [52]. Flux-weighted events for specific

neutrino energies were generated, and these events were binned according to the reconstruction procedure, effectively determining the matrix that determines the distribution of reconstructed energies for a true energy.

The excess of electron-like events in bins of low reconstructed energies found by MiniBooNE [83], was investigated in the same manner in more recent work, where it was found that the multi-nucleon contributions reduce the excess, but not enough to explain the anomaly [84]

In the following, we do not include any multi-nucleon effects, and will assess the general effects of the reconstruction procedure on the pure quasi-elastic cross section.

4.2 ENERGY DISTRIBUTIONS WITH FIXED LEPTON OBSERVABLES

Fixed lepton observables $\cos\theta$ and E_l constitute a range of incoming neutrino energies E_ν by $E_l = E_\nu - \omega$. We can examine the probability of an event with a certain neutrino energy by considering the product of the double differential cross section $\frac{d^2\sigma}{d\omega d\cos\theta}$ with the incoming flux $\Phi(E_\nu)$. The probability of an event with given lepton observables and neutrino energy E_ν is proportional to

$$f(E_\nu, E_l, \theta) dE_\nu = C \frac{d^2\sigma}{d\omega d\cos\theta} \Big|_{\omega=E_\nu-E_l} \Phi(E_\nu) dE_\nu. \quad (4.3)$$

We choose the normalization constant C as the inverse of the total flux such that f has the dimension of a cross section divided by an energy squared. All the cross sections are for quasi-elastic scattering off ^{12}C .

The distribution $f(E_\nu, E_l, \theta)$, using the MiniBooNE ν_μ -flux prediction [8], is shown for different values of $T_\mu = E_\mu - m_\mu$ and θ in Fig. 4.1. The green vertical line shown the reconstructed energy as defined by eq. (4.1).

The cross sections obtained in the HF and CRPA models are compared to a RFG prediction with $p_F = 220$ MeV based on the appendix of [85].

One sees for the RFG model, that the reconstructed energy with $\cos\theta = 0.5$ and 0.2 seems to represent the average energy of the RFG model. In the forward direction the reconstructed energy lies on the peak, and the distribution is narrow. In the backward direction the peak and average of $f(E_\nu, \cos\theta, E_\mu)$ are lower than the reconstructed energy.

A shift of the HF and CRPA models is notable. The shift is due to the inherent inclusion of shell-effects and binding energy in these models. The reconstructed energy with a correction for binding shifts the value of the reconstructed energy. The values of the separation energy in eq. (4.2) could be tuned to reproduce the peak or the average of $f(E_\nu, \cos\theta, E_\mu)$ in certain parameter regions to increase the accuracy of the energy reconstruction based on a certain cross section. Using $E_B = 34$ MeV the reconstructed energy is more representative of the average of $f(E_\nu, \cos\theta, E_l)$ in the HF and CRPA case.

One sees that the reconstruction formula underpredicts the average of the distribution in the forward scattering case, and seems to overpredict the average in the

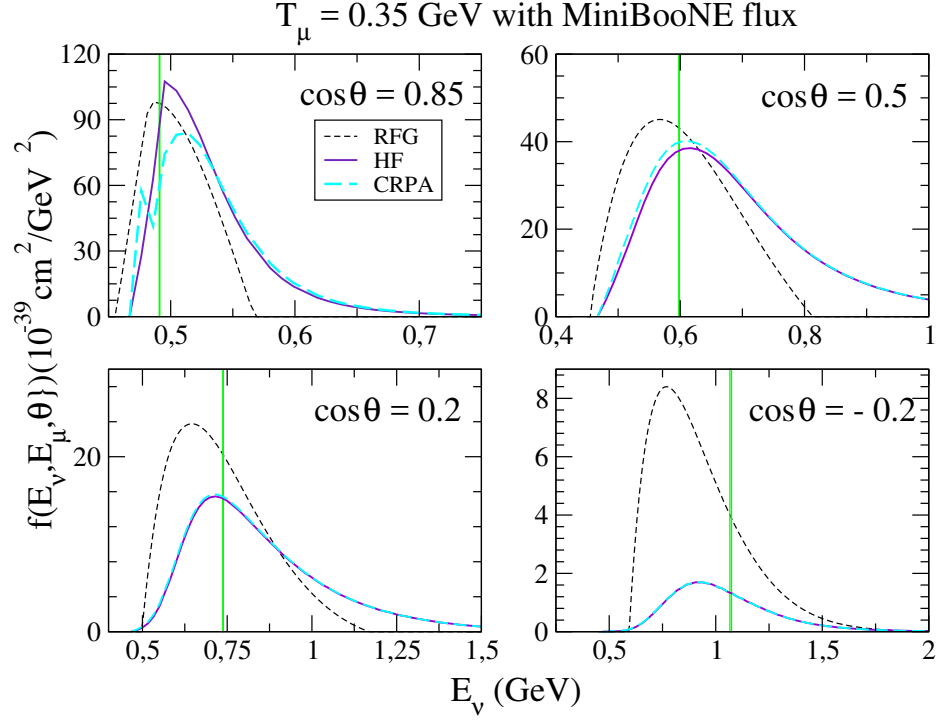


Figure 4.1: Energy distribution for fixed lepton observables. The [HF](#) and [CRPA](#) distributions are compared to a relativistic Fermi gas. For a muon with kinetic energy $T_\mu = 350 \text{ MeV}$ with different scattering angles using the [MiniBooNE](#) flux prediction [8] The reconstructed energy in accordance with eq. (4.1) is given by the green horizontal line.

opposite direction. These effects will average out, and the reconstructed energy then seems able to reproduce the average energy contribution when integrated over lepton kinematics.

The [HF](#) and [CRPA](#) models show a less symmetric picture compared to the [RFG](#). A large part of the strength is due to the tails of the distributions.

The [RFG](#) model was tuned to resemble the reconstruction procedure as closely as possible. We did not include any binding correction to the [RFG](#) to illustrate the general effects of the reconstruction procedure. One can thus conclude that as long as the binding energy is well-chosen the reconstructed energy seems able to reproduce the average energy in the [RFG](#) when averaging over lepton variables. This will be shown explicitly in the next chapter, where we will see that the cross section in terms reconstructed energies does not differ significantly from the actual cross section for a [RFG](#).

In what follows we compare the distributions obtained from the **HF** and **CRPA** to the ones obtained in the description of Martini et. al [10, 38]. The model labeled by either *QE-bare* or *LRFG* is the local relativistic Fermi gas of Martini, we use (*QE*) *RPA* to denote the local Fermi gas with RPA contributions.

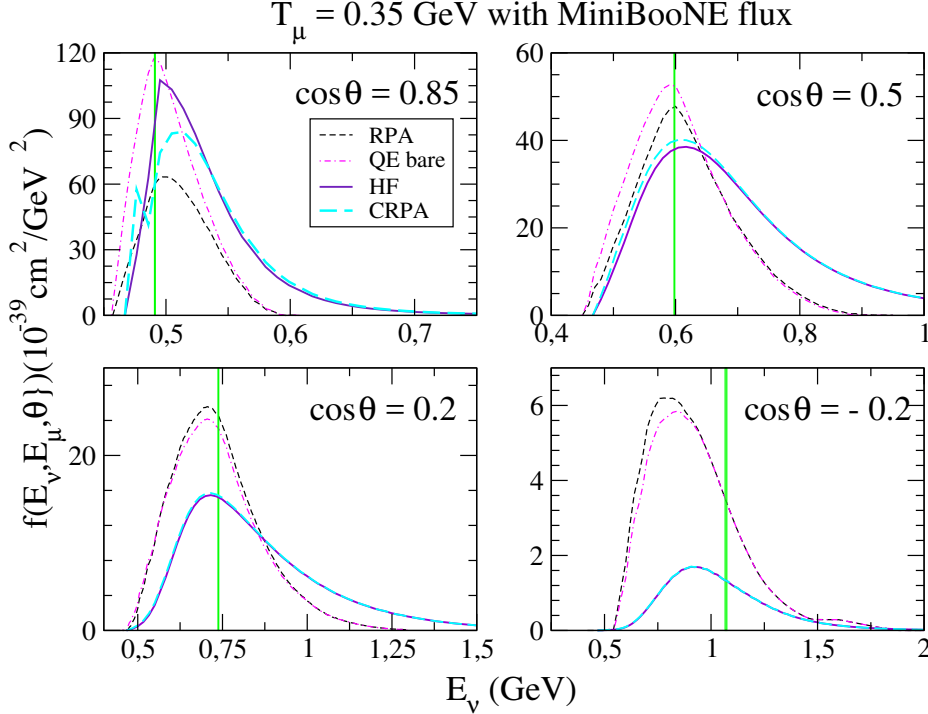


Figure 4.2: Comparison of the energy distributions using four different models for the double differential cross section. The **HF** and **CRPA** models are described in [10]. The *QE bare*, and *QE RPA* models are described in [37, 38]. Distributions $f(E_\nu, \cos\theta, E_l)$ shown for a muon with kinetic energy $T_\mu = 350 \text{ MeV}$ and different scattering angles using the MiniBooNE ν_μ -flux prediction [8]. The reconstructed energy in accordance with eq. (4.1) is given by the green vertical line.

4.2.1 Comparison of reconstructed energy distributions

The comparison of energy distributions for fixed lepton observables between different models are essentially comparisons of double differential cross sections. A point of attention however is the relation $E_\nu = E_l + \omega$ which fixes the energy transfer considered for a certain neutrino energy. When comparing the **CRPA** and **HF** double differential cross sections to the model of Martini in Fig. 4.5 the quasi-elastic peaks align when the *QE bare*, and the *QE RPA* cross sections are shifted by 18 MeV in ω [86].

This means that although for $\cos\theta = 0.5$ the **HF** and *QE RPA* cross sections are comparable in strength and shape for a fixed incoming energy, the distributions

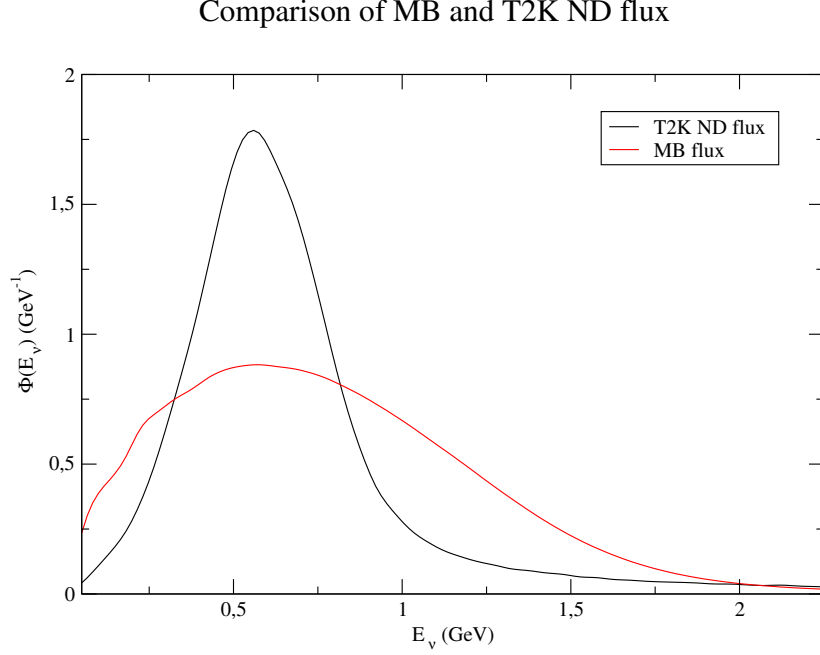


Figure 4.3: Comparison of the [MiniBooNE](#) and [T2K](#) near detector flux predictions [8, 87].

$f(E_\nu, \cos \theta, E_l)$ are not. The shift in ω , required to match the position of the peaks in the cross section shown in Fig. 4.5, means that the value for $f(E_\nu, \cos \theta, E_l)$ at some $E_\nu = E_l + \omega$ will differ. This can be seen in Fig. 4.2 where the distributions $f(E_\nu, \cos \theta, E_l)$ are compared for different values of the scattering angle for muon with $T_\mu = 350$ MeV. This also explains the seemingly large discrepancy for the backward scattering with $\cos \theta = -0.2$.

Again the position of the peaks differ due to the inherent inclusion of binding energy in the [HF](#) and [CRPA](#) cross sections, absent in the model of Martini. Due to the shell structure of the HF description there is a minimal separation energy of around 16 MeV present. This means that the range of possible energies starts at $E_\nu^{\min} = E_l + \omega_{\min}$. However the most important feature is the redistribution of strength from the peak to the tails of the distribution. This was already noted in the previous comparison with the [RFG](#), but the effect persists when compared to the more realistic local Fermi gas.

4.2.1.1 Effect of the flux-weighting

The flux dependence of the distributions can be seen by comparing Fig. 4.4 with Fig. 4.2 where $f(E_\nu, \cos \theta)$ is shown for the [T2K](#) and [MiniBooNE](#) fluxes respectively. The normalized fluxes are shown in Fig. 4.3 [8, 87]. The [T2K](#) flux is more sharply peaked in comparison to the [MiniBooNE](#) flux due to its off-axis geometry.

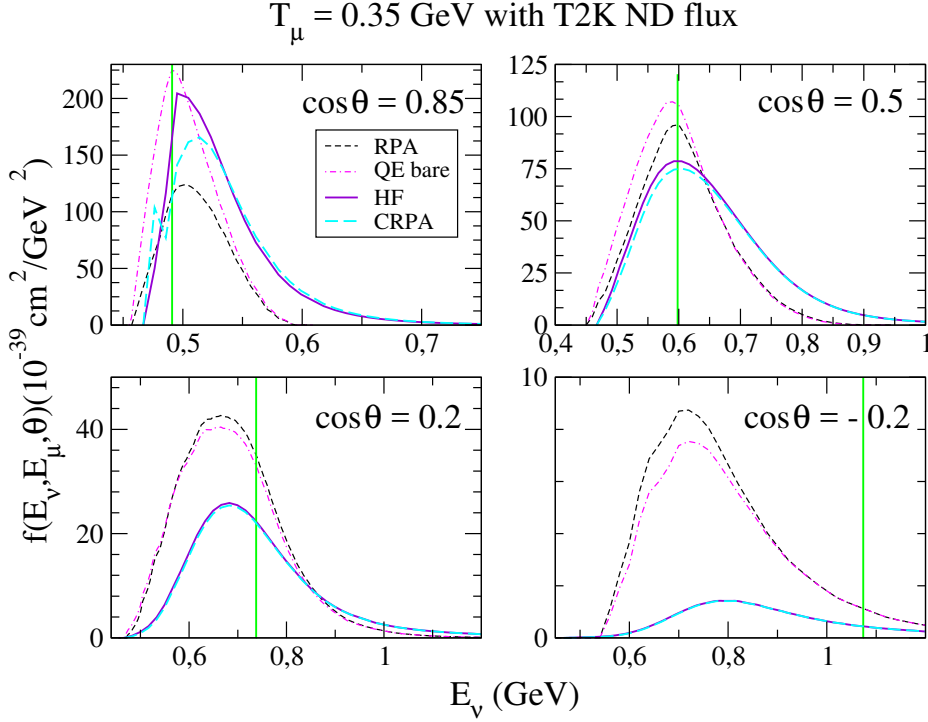


Figure 4.4: Comparison of the reconstructed energy distributions using four different models for the double differential cross section [37, 88]. For a muon with kinetic energy $T_\mu = 350 \text{ MeV}$ and the same scattering angles as in Fig. 4.2 using the T2K near detector flux [87]. The reconstructed energy in accordance with eq. (4.1) is given by the green horizontal line.

When comparing the energy distributions $f(E_\nu, \cos \theta, E_l)$ this results in an enhancement of the peaks around values of $E_\nu \approx 600 \text{ MeV}$ and a quenching of the tails especially obvious for $\cos \theta = 0.5$ and 0.2 from the T2K flux. The reconstructed energy reproduces the peak position quite well for the considered forward scattering angles but becomes gradually worse for more backward angles. For $\cos \theta = -0.2$ there is no real relationship between the reconstructed energy and $f(E_\nu, \cos \theta, E_l)$ in the T2K case, the reconstructed value lies far in the tail of the distribution. Due to the shape of the flux the probability of a neutrino having energy \bar{E}_ν is very low.

Whereas for the structureless part of the cross sections, meaning the part dominated by the quasi-elastic peak as shown previously, the different cross sections do not significantly differ in shape, larger discrepancies between the models are present for more forward scattering angles. A thorough comparison of the double differential cross sections was already done for electron neutrinos, and the differences are highlighted in Fig. 4.5 [86]. The most important feature is the presence of giant resonance peaks in the CRPA approach, and the quenching of the QE peak in favor of the higher ω tail. When determining the distribution of energies for a certain reconstructed energy without specification of the lepton observables much of the structure

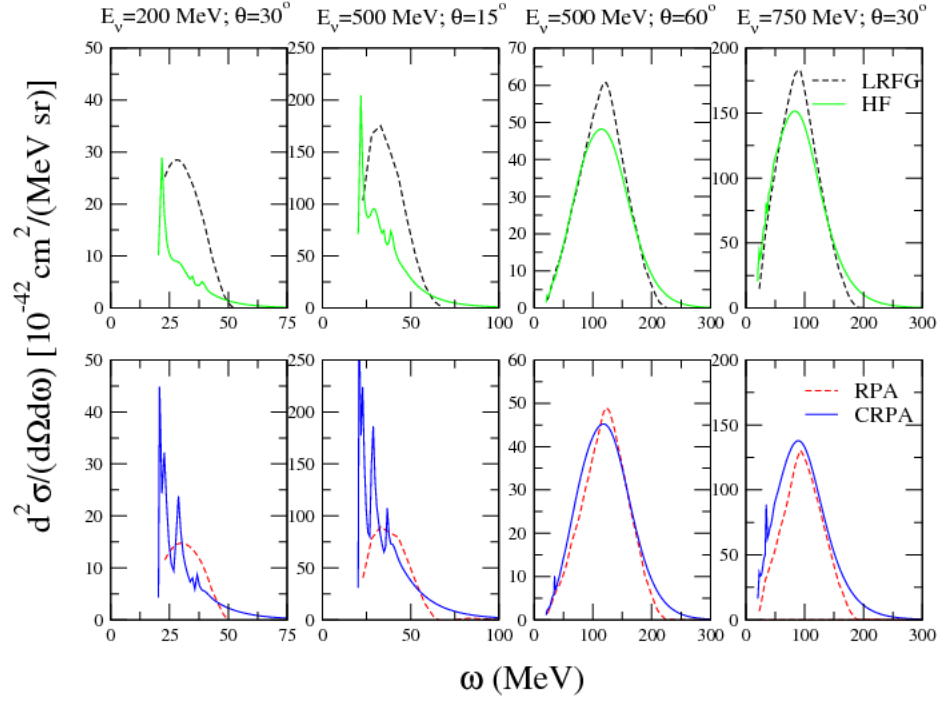


Figure 4.5: Comparison of the double differential cross sections for electron neutrinos on ^{12}C for different energies and scattering angles. The HF and local relativistic Fermi gas (*QE bare*) are compared in the top row. The CRPA is compared to the *QE RPA* in the bottom row. The LRFQ and RPA results are shifted to the right by 18 MeV to account for the binding energy. Figure taken from [86]

of the cross section is not immediately visible, nonetheless one should be aware of the fact that models with vastly different cross section strengths and shape in certain parameter regions can seem rather equivalent when considering the whole phase space. For example, the HF, and CRPA cross sections can differ strongly, especially in more forward scattering bins, as can be seen in Fig. 4.5 In the next section we will present the distributions of reconstructed energy obtained without specification of the lepton observables, considered over the whole phase space. We will not look at the distributions in specific angular bins, or for specific regions of E_l .

Efforts have been made [90] to increase the accuracy with which the reconstructed energy describes the peak of $f(E_\nu, \cos\theta, E_l)$. In principle the value of the reconstructed energy is not of direct interest, but it is merely a tool in order to later unfold the data into bins that resemble the real energy. In that sense a more accurate reconstructed energy would be able to reduce the spread on the distributions of E_ν for a value of \bar{E}_ν , in the following chapter defined as $d(E_\nu, \bar{E}_\nu)$, improving the accuracy of the unfolding procedure. The improved reconstruction procedure would also facilitate interpretation of data in terms of reconstructed energies. However it would introduce a model-dependence into the definition of \bar{E}_ν , which makes it far more difficult to compare predictions in terms of \bar{E}_ν .

RECONSTRUCTED ENERGY DISTRIBUTIONS

The energy distributions for fixed lepton variables $f(E_\nu, \cos \theta, E_l)$ discussed in the previous chapter, show the discrepancies of a simple reconstruction procedure based on the assumption of scattering on the quasi-elastic peak with an average separation energy. We shall here outline the procedure of predicting the amount of events in terms of the reconstructed energy. We follow the framework and notation from [79, 81], and will link it to the equivalent definitions in [80]. We will first look at a smearing function which gives information on the shape of the distribution of reconstructed energies. Then in a more quantitative approach we give the expression for the cross section per E_ν and \bar{E}_ν , from which the amount of events in reconstructed energy bins can be predicted using the double differential cross section. We investigate the dependence of the distributions on the lepton mass and binding energy E_B used in the reconstruction procedure, and compare the distributions obtained in the Continuum Random Phase Approximation (CRPA) model, the Relativistic Fermi Gas (RFG) and the model of Martini et al. [37].

5.1 THE SMEARING FUNCTION

Considering the reconstruction procedure as described in the previous chapter. The reconstructed energy is given by eq. (4.2) as

$$\bar{E}_\nu = \frac{2M'_n E_l - ((M'_n)^2 + m_l^2 - M_p^2)}{2(M'_n - E_l + P_l \cos \theta)} \quad (4.2)$$

where as stated before the case without binding energy in eq. (4.1) is retrieved by setting $M'_n = M_p$.

The probability $F(E_\nu, \bar{E}_\nu)$ of finding the real energy E_ν for a given reconstructed energy \bar{E}_ν , is again proportional to the product of the cross section with the flux. We integrate this product over all the lepton observables corresponding to this reconstructed energy.

$$F(E_\nu, \bar{E}_\nu) = C\Phi(E_\nu) \int_{E_l^-}^{E_l^+} dE_l \frac{d^2\sigma}{d\omega d\cos\theta} \Big|_{\omega=E_\nu-E_l, \theta=\theta(E_l, \bar{E}_\nu)} \quad (5.1)$$

where Φ denotes the normalized flux. The constant C is a normalization constant, which will be discussed later. The set of lepton energies contributing to a certain reconstructed energy lie between the extreme values found for E_l by setting $\cos \theta = \pm 1$.

For a massless final state lepton, and without taking into account binding energy, one finds $E^+ = \bar{E}_\nu$ and $E^- = \frac{\bar{E}_\nu}{1+2\bar{E}_\nu/M_n}$. One can easily see this by considering that

the reconstructed energy is determined as the location of the quasi-elastic peak. This means that on the quasi-elastic peak $\omega = \bar{E}_\nu - E_l$. The quasi-elastic peak is given by the condition $\omega = (q^2 - \omega^2)/2M$. Bringing these expressions together for $\cos\theta = \pm 1$ results in

$$\omega = \bar{E}_\nu - E_l = \frac{(\bar{E}_\nu \pm P_l)^2 - (\bar{E}_\nu - E_l)^2}{2M} = \frac{(\bar{E}_\nu \pm E_l \sqrt{1 - \frac{m^2}{E_l^2}})^2 - (\bar{E}_\nu - E_l)^2}{2M}. \quad (5.2)$$

When neglecting the lepton mass, the solutions E_l then correspond to the aforementioned E_l^+ , and E_l^- . For an E_l in this range one can then solve for the corresponding $\cos\theta(E_l, \bar{E}_\nu)$ from equation 4.2.

The normalization factor C , will in this work either be chosen such that the distribution in eq. (5.1) is normalized to unity, or it will be set to $C = 1$. By normalizing the distribution to unity one can interpret it as a probability distribution [79]. We shall denote by $F(E_\nu, \bar{E}_\nu)$ the distribution when normalized to unity, and by $I(E_\nu, \bar{E}_\nu)$ the non normalized distribution with $C = 1$.

Information such as the average energy $\langle E_\nu \rangle$ and variance σ can be extracted as the first and second moment of the distribution $F(E_\nu, \bar{E}_\nu)$.

$$\langle E_\nu \rangle = \int dE_\nu E_\nu F(E_\nu, \bar{E}_\nu), \quad (5.3)$$

$$\sigma^2 = \int dE_\nu E_\nu^2 F(E_\nu, \bar{E}_\nu) - \langle E_\nu \rangle^2. \quad (5.4)$$

One can also fold a measured distribution in terms of reconstructed energies $g(\bar{E}_\nu)$ with $F(E_\nu, \bar{E}_\nu)$ to obtain the distribution in neutrino energies $G(E_\nu)$

$$G(E_\nu) = \int d\bar{E}_\nu g(\bar{E}_\nu) F(E_\nu, \bar{E}_\nu). \quad (5.5)$$

This smearing procedure redistributes the strength from bins of reconstructed energies \bar{E}_ν into bins of true neutrino energies E_ν . The multi-nucleon component, has been shown to play a big role in the errors of the energy reconstruction procedure as it redistributes low reconstructed energies to higher reconstructed energies [79–82]. Note that the total amount of events is conserved by the smearing procedure, the only effect is a redistribution of strength.

5.2 CROSS SECTION IN TERMS OF RECONSTRUCTED ENERGIES

In order to construct a more quantitative distribution we write the amount of events for certain values $(E_\nu, \omega, \cos\theta)$ as the product of the flux $\Phi(E_\nu)$ with the double differential cross section

$$g(E_\nu, \omega, \cos\theta) dE_\nu d\omega d\cos\theta = \frac{d^2\sigma}{d\omega d\cos\theta}(E_\nu, \omega, \cos\theta) \Phi(E_\nu) dE_\nu d\omega d\cos\theta. \quad (5.6)$$

We will transform this distribution to the variables $(E_\nu, E_l, \bar{E}_\nu)$. We assume a general case for some reconstruction procedure $\bar{E}_\nu = f(E_l, \cos \theta)$, i.e. the reconstructed energy depends on the measurable kinematic variables. In any case we then have

$$\begin{aligned} E_\nu &= E_\nu \\ \omega &= E_\nu - E_l \\ \cos \theta &= h(E_l, \bar{E}_\nu) \end{aligned}$$

Where h is the function found by inverting $f(E_l, \cos \theta)$. The only dependence on reconstructed energy is thus in $\cos \theta(E_l, \bar{E}_\nu)$. The Jacobian determinant is

$$\mathcal{J} = \begin{vmatrix} 1 & 0 & 0 \\ 1 & -1 & 0 \\ 0 & \frac{\partial \cos \theta}{\partial E_l} & \frac{\partial \cos \theta}{\partial \bar{E}_\nu} \end{vmatrix} = -\frac{\partial \cos \theta}{\partial \bar{E}_\nu}$$

For the quasi-elastic reconstruction formulas in eqs. (4.2, 4.1), with- and without the binding energy correction respectively, this is

$$-\frac{\partial \cos \theta}{\partial \bar{E}_\nu} = \frac{ME_l - m_l^2/2}{\bar{E}_\nu^2 P_l}, \quad (5.7)$$

$$-\frac{\partial \cos \theta}{\partial \bar{E}_\nu} = \frac{2M'_n E_l - ((M'_n)^2 + m_l^2 - M_p^2)/2}{\bar{E}_\nu^2 P_l}. \quad (5.8)$$

With this we can write the amount of events predicted in bins of $(E_\nu, \bar{E}_\nu, E_l)$ as

$$\mathcal{J} \Phi(E_\nu) \frac{d^2 \sigma}{d\omega d \cos \theta} (E_\nu, \omega, \cos \theta) \Big|_{\omega=E_\nu-E_l, \cos \theta(E_l, \bar{E}_\nu)} dE_\nu d\bar{E}_\nu dE_l. \quad (5.9)$$

Keeping this in mind we define the distribution $d(E_\nu, \bar{E}_\nu)$ by

$$d(E_\nu, \bar{E}_\nu) = \int_{E_l^-}^{E_l^+} dE_l \mathcal{J} \frac{d^2 \sigma}{d\omega d \cos \theta} \Big|_{\omega=E_\nu-E_l, \cos \theta(E_l, \bar{E}_\nu)}. \quad (5.10)$$

The amount of events in a bin of reconstructed energy $N(\bar{E}_\nu)$, for a given flux $\Phi(E_\nu)$, is then given in terms of $d(E_\nu, \bar{E}_\nu)$ as

$$N(\bar{E}_\nu) = \int dE_\nu \Phi(E_\nu) d(\bar{E}_\nu, E_\nu). \quad (5.11)$$

Also, the total cross-section in terms of E_ν is recovered from the distribution as

$$\sigma(E_\nu) = \int d\bar{E}_\nu d(\bar{E}_\nu, E_\nu). \quad (5.12)$$

The distribution $d(\bar{E}_\nu, E_\nu)$ represents the cross section, differential in \bar{E}_ν . It is this distribution which in [80] is denoted as

$$\frac{d\sigma}{d\bar{E}_\nu} (E_\nu, \bar{E}_\nu) \equiv d(\bar{E}_\nu, E_\nu). \quad (5.13)$$

5.2.1 Unfolding procedure

We will briefly outline some results from [80] on the unfolding of distributions in terms of reconstructed energies. In keeping with the notation in eq. (5.13) we can write the probability of an event with a certain reconstructed energy for a given flux $\Phi(E_\nu)$ as

$$P(\bar{E}_\nu) = \frac{1}{\langle \sigma \Phi \rangle} \int dE_\nu \frac{d\sigma}{dE_\nu} \Phi(E_\nu), \quad (5.14)$$

where $\langle \sigma \Phi \rangle$ is a normalization factor, namely the total flux averaged cross section which thus gives the total number of events. Using this one can write the conditional probability, of finding a real energy E_ν for a given \bar{E}_ν as

$$P(E_\nu | \bar{E}_\nu) = \frac{\Phi(E_\nu) \frac{d\sigma}{dE_\nu}}{\int dE_\nu \Phi(E_\nu) \frac{d\sigma}{dE_\nu}}. \quad (5.15)$$

This conditional probability $P(E_\nu | \bar{E}_\nu)$ is equivalent to the normalized distributions $F(E_\nu, \bar{E}_\nu)$ obtained in eq. (5.1), except for the Jacobian.

Using the relation between the cross section and $P(\bar{E}_\nu)$ one gets

$$\sigma(E_\nu) = \int d\bar{E}_\nu \{ \langle \sigma \Phi \rangle P(\bar{E}_\nu) \} \times \left[\frac{\frac{d\sigma}{dE_\nu}(E_\nu, \bar{E}_\nu)}{\int dE_\nu \Phi(E_\nu) \frac{d\sigma}{dE_\nu}} \right]. \quad (5.16)$$

The term between braces $\langle \sigma \Phi \rangle P(\bar{E}_\nu)$ is the amount of events in a bin of reconstructed energy, this term is measured by experiments. The unfolding process is equivalent to the calculation of the above expression, for a measured distribution of data as the term between braces.

The model dependence of the unfolding procedure is introduced by the term between brackets. This term determines the redistribution of data in terms of \bar{E}_ν to E_ν . If one uses a model which accurately describes the cross section the term between braces cancels the denominator of the second term (i.e. the cross section as a function of reconstructed energy reproduces the reconstructed data) and the cross section is recovered. If however the unfolding is done using a RFG which does not contain for example a multinucleon component, while the multi-nucleon component is present in the data, the unfolded cross section need not resemble the actual cross section.

To be able to distinguish the actual cross section $\sigma(E_\nu)$ and energy E_ν , from the unfolded cross section and energy we denote the latter $\sigma_{uf}(E_\nu^{uf})$, or $\sigma(E_\nu^{uf})$ where the argument determines that we are looking at the unfolded distribution.

The model dependence of the unfolding procedure was made clear by Miniature Booster Neutrino Experiment (MiniBooNE), and therefore the unfolded energy in MiniBooNE data is labeled as $E_\nu^{QE,RFG}$, where the superscript denotes that the distribution was unfolded using a RFG model.

In order to compare theoretical models with the unfolded cross sections σ_{uf} one should calculate the unfolding term (between brackets in eq. (5.16)) using the same model used to unfold the data in the first place, and calculate the term between braces using the predicted cross section. One then recovers the unfolded cross section $\sigma_{uf}(E_\nu^{uf})$ which can be compared to the unfolded data.

It is by unfolding the distribution $P(\bar{E}_\nu)$, obtained from eq. (5.14) with a model containing a multi-nucleon component [42], through a simple RFG with $M_A \approx 1.3$ GeV, that the seemingly anomalous MiniBooNE data was explained in [80].

Using the unfolding procedure as described above, it is possible to make an approximate theoretical prediction of events in bins of unfolded energies. The procedure used by experiments is based on an analogous discrete approach dubbed iterative Bayesian unfolding described in [91, 92]. The procedure is based on Monte-Carlo simulations to describe the unfolding matrix, taking into account detector efficiencies and backgrounds.

The unfolding procedure also depends on the predicted flux, in the case of cross-section measurements where the flux is well defined this does not pose a problem. However when looking at an oscillation experiment, where the flux is also an observable of interest, the distribution in terms of unfolded energies can not directly be linked to the distribution in terms of real energies unless the model (flux dependent) accurately describes the data (i.e. reproduces the distribution in reconstructed bins).

Accurately reproducing the unfolding procedure in order to compare theoretical predictions in terms of unfolded energies is rather difficult as the unfolding process has to be carefully mimicked. It is much easier to predict events in bins of reconstructed energies as they're far more clearly defined.

5.3 COMPARISON OF $d(E_\nu, \bar{E}_\nu)$ IN DIFFERENT MODELS

In this section we will compare the distributions $d(E_\nu, \bar{E}_\nu)$, and $F(E_\nu, \bar{E}_\nu)$, obtained in different nuclear models. First we will take a look at the dependence of these distributions on the lepton mass m_l , and the binding energy E_B . Afterwards we compare $d(E_\nu, \bar{E}_\nu)$ obtained from the Hartree Fock (HF), and CRPA models. In the last subsection $d(E_\nu, \bar{E}_\nu)$ in the CRPA is compared to a simple RFG model, and to the model of Martini et al. [37, 38].

5.3.1 *Dependence on lepton mass and separation energy*

Before we discuss the influence of the binding correction, we wish to make clear that the parameter E_B refers to the separation energy introduced in eq. (4.2). The inherent binding energy in the HF and CRPA descriptions are due to the shell structure of the nucleus, in this work this binding energy is not considered a parameter, and is in no

way altered. It is only the definition of the reconstructed energy which is changed by E_B in eq. (4.2).

The lepton mass m_l and separation energy E_B influence $d(E_\nu, \bar{E}_\nu)$ ¹ through the solution of $\cos \theta(E_\nu, \bar{E}_\nu)$ and by the integration bounds E_l^+ and E_l^- that determine the combinations of lepton energy and angle that enter \bar{E}_ν . In the simple case, ignoring any binding energy and lepton mass, we found the integration bounds from eq. (5.2). We expand this equation under the assumption that the lepton's mass is small in comparison to its energy to assess the influence of a small lepton mass.

$$E_l^+ = \frac{-(E_\nu - E_l \sqrt{1 - \frac{m^2}{E_l^2}})^2 + (E_\nu - E_l)^2}{2M} + \bar{E}_\nu \quad (5.17)$$

$$\approx -m^2 \frac{\left(1 - \frac{\bar{E}_\nu}{E_l^+}\right)}{2M} + \bar{E}_\nu \quad (5.18)$$

In the massless case $E_l^+ = \bar{E}_\nu$, thus for a small mass, the term between brackets is expected to be negligible and the upper limit remains practically unchanged.

The lower limit is

$$E_l^- \approx \left(-\frac{2E_\nu E_l^-}{M} + \bar{E}_\nu \right) + m^2 \frac{1 + \frac{\bar{E}_\nu}{E_l^-}}{2M}. \quad (5.19)$$

The term between brackets is the solution in the massless case. For the lower limit, filling in E_l^- one obtains $m^2(1 + \frac{\bar{E}_\nu}{M})/M$ for the second term. The lower limit is thus more influenced by the lepton mass.

In practice, the integration bounds are determined by setting $\cos \theta = \pm 1$ in the reconstruction function. For eq. (4.2) this yields a second order polynomial in E_l

$$\begin{aligned} 0 = & E_l^2 \cdot [M_n'^2 + 2\bar{E}_\nu M_n'] \\ & + E_l \cdot [-2(M_n' + \bar{E}_\nu)(M_n' \bar{E}_\nu + m'^2/2)] \\ & + [(M_n' \bar{E}_\nu + m'^2/2)^2 + m^2 \bar{E}_\nu^2] \end{aligned}$$

with roots E_l^\pm . In this polynomial $m' = M'^2 + m^2 - M_p^2$. By setting $m' = m$ and $M_n' = M_p = M_n$ the case without binding energy is recovered.

In Fig. 5.1 the function $\cos \theta(E_l, \bar{E}_\nu)$ is plotted for different values of \bar{E}_ν . The thin dashed lines represent $\cos \theta$ obtained for the simple reconstruction formula in eq. (4.1), the fat dashed lines are obtained with the inclusion of a separation energy $E_b = 34$ MeV in eq. (4.2). Both dashed lines are solution for a final state muon. The solution for electrons, with the same separation energy $E_b = 34$ MeV, is shown by the straight line.

This figure should be interpreted in light of eq. (5.10), the integration range can be determined from the E_l -axis, the cross section is integrated for values of E_l between

¹ And $F(E_\nu, \bar{E}_\nu)$ in the same way

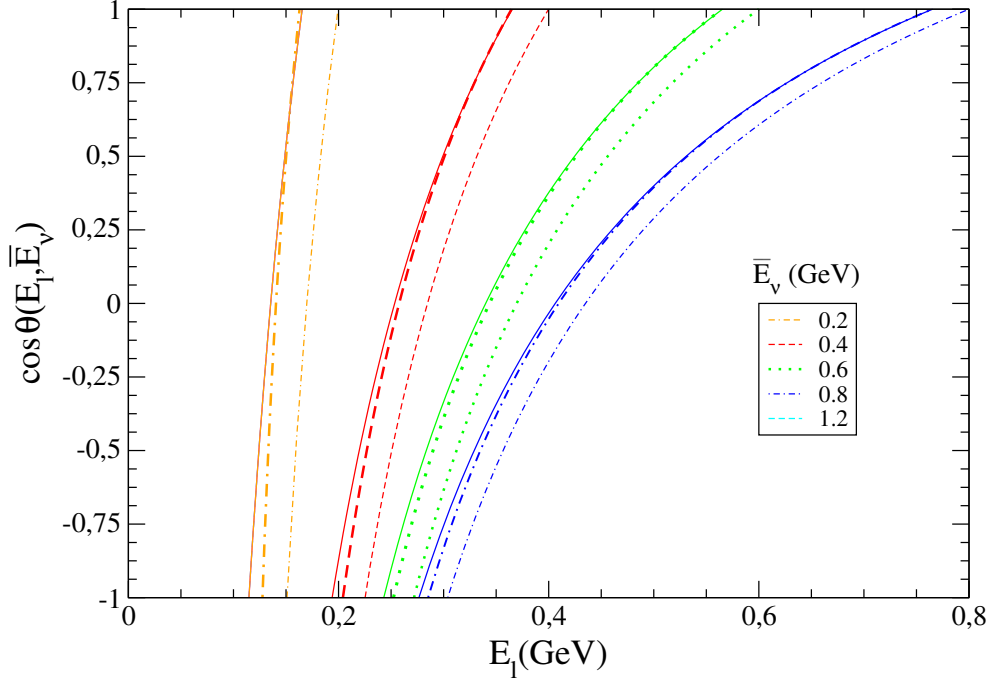


Figure 5.1: The effect of the separation energy and rest mass of the final state lepton on $\cos\theta(E_l, \bar{E}_\nu)$. The dashed lines are for a final state muon, where the thin dashed lines do not include a separation energy and the thick dashed lines are for a separation energy of $E_b = 34$ MeV. The straight lines are the solutions for a final state electron using the same separation energy.

E_l^+ and E_l^- , given by the points for which $\cos\theta = \pm 1$. For each E_l in this range, the angle by which the integrand is considered is given by $\cos\theta(E_l, \bar{E}_\nu)$. The integration is thus performed along this line in the $E_l, \cos\theta$ space.

The most obvious effect of the separation energy is that the integration range is shifted to lower energies. Less obvious is that the integration range becomes narrower, the narrowing of the integration range will reduce the strength and width of the distribution $F(E_\nu, \bar{E}_\nu)$. The narrowing of the integration range is more important for lower values of \bar{E}_ν as in this case the range is already smaller than for higher values.

The effect of a non-zero lepton mass is consistent with what was anticipated by the discussion above. Comparing the red dashed- and filled lines, the solution for the muon- and electron mass respectively, the upper limit is not much affected while the lower limit is affected far more.

The effect of the smaller electron mass is a broadening of the integration range, the integration bounds are resembling the bounds for a massless lepton. Thus the distribution $d(E_\nu, \bar{E}_\nu)$ for an electron in the final state is expected to be larger and broader than for a final state muon. This is to be expected as the phase space for

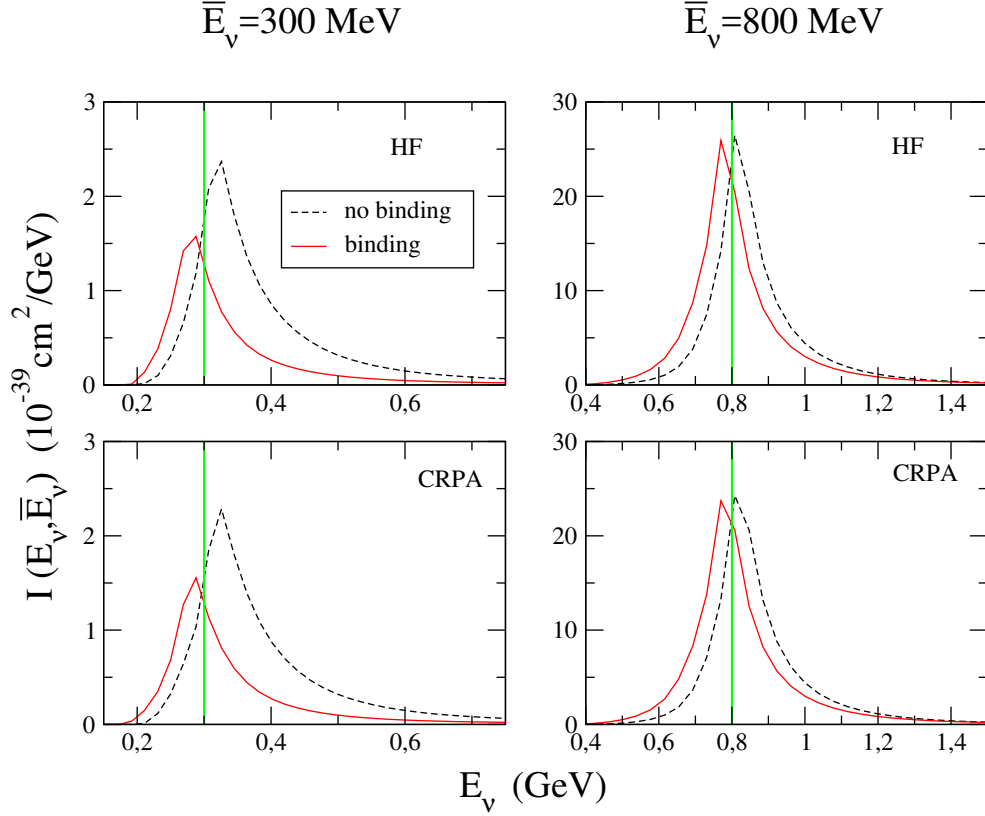


Figure 5.2: Effect of a separation energy of $E_b = 34$ MeV on the distribution $I(E_\nu, \bar{E}_\nu)$ (defined by setting $C = 1$ in eq. (5.1)) using the MiniBooNE flux [8].

a final state lepton with a lower rest mass is larger, and the total cross section is therefore larger.

The influence of the separation energy $E_b = 34$ MeV as used by MiniBooNE [9] on the distributions $I(E_\nu, \bar{E}_\nu)$, defined by taking $C = 1$ in eq. (5.1), is shown in Fig. 5.2. In this figure, the value of \bar{E}_ν is kept fixed, but the distribution labeled with *no binding* is obtained by defining \bar{E}_ν by eq. (4.1), while *binding* is obtained from eq. (4.2). No changes are made to the model, the only difference is that \bar{E}_ν is defined differently, leading to a different energy distribution for a fixed value of \bar{E}_ν .

One can see that for $\bar{E}_\nu = 800$ MeV the effect is basically a simple shift of the distribution. For lower values of the reconstructed energy, in this case $\bar{E}_\nu = 300$ MeV, the narrowing of the distribution, a reduction in strength and a shift is visible. However, the distribution $I(E_\nu, \bar{E}_\nu)$ does not include the Jacobian, thus the reduction in strength is simply illustrative.

Looking at the *no binding* case, we see that the reconstructed energy is not well suited to the distribution. It under predicts the peak, as well as the average of the distribution. From this one expects more events in bins of low reconstructed energy as compared to the real neutrino energy. The binding correction improves the re-

constructed energy. The reconstructed energy seems to resemble the average of the distribution $I(E_\nu, \bar{E}_\nu)$.

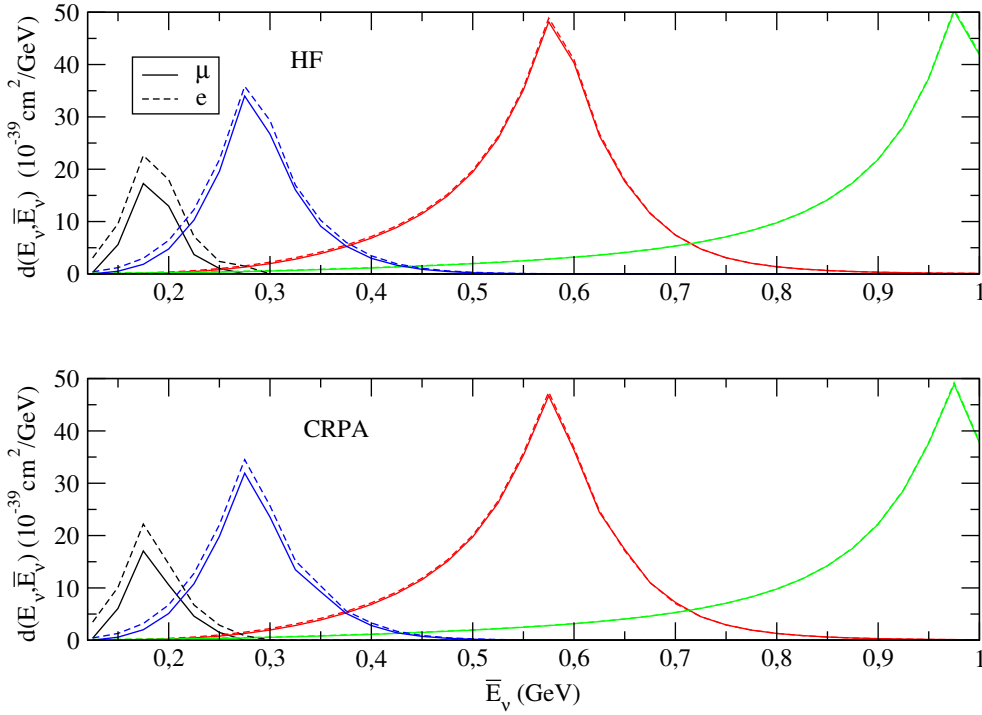


Figure 5.3: Effect of the final state lepton mass on the distribution $d(E_\nu, \bar{E}_\nu)$. The distributions are shown for fixed values of $E_\nu = 0.2, 0.3, 0.6,$ and 1 GeV, and \bar{E}_ν was obtained from eq. (4.1).

The distributions $d(E_\nu, \bar{E}_\nu)$ are compared in Fig. 5.3 for different final state leptons. As anticipated, for low values of the reconstructed energy the broadening of the integration range due to the smaller lepton rest mass influences the distributions. For higher reconstructed energies the distributions are practically the same.

In Fig. 5.3, $d(E_\nu, \bar{E}_\nu)$ is obtained from eq. (4.1). Comparing this with Fig. 5.2, also in the *no binding* case, the underprediction of the peak and average lead to a large strength for low reconstructed energies \bar{E}_ν .

5.3.2 Comparison of the Hartree-Fock and Continuum Random Phase Approximation

In this section we first compare the energy distributions obtained in the CRPA with the ones obtained from the bare HF model. Afterwards we shall compare these to distributions obtained with RFG based models. In this section \bar{E}_ν is always defined by eq. (4.2), with $E_B = 34$ MeV.

The distribution $d(E_\nu, \bar{E}_\nu)$ as obtained from eq. (5.10) are shown in Fig. 5.4. The HF and CRPA results do not differ significantly. The HF distributions are slightly larger,

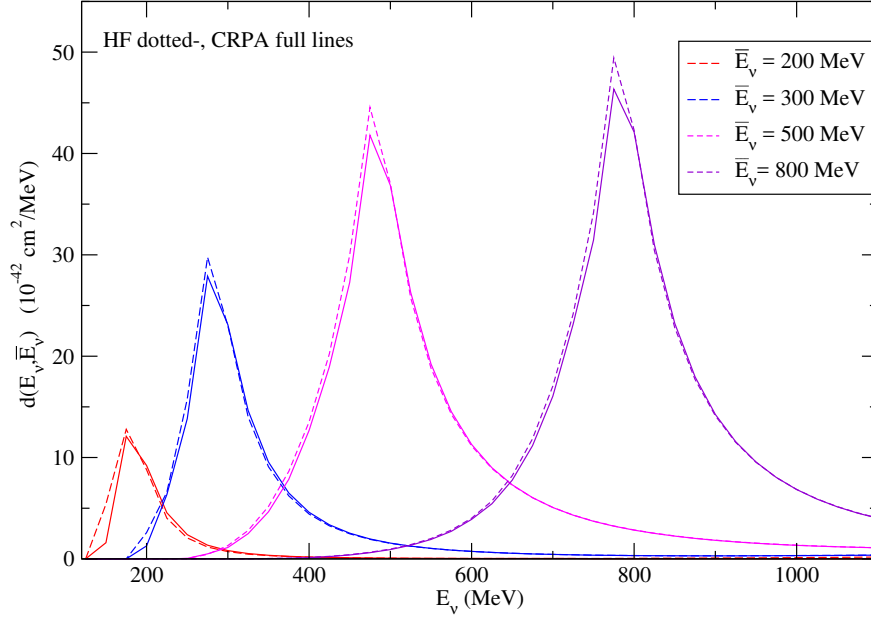


Figure 5.4: Comparison of $d(E_\nu, \bar{E}_\nu)$ in the HF (dotted lines) and CRPA (straight lines) approach for fixed values of \bar{E}_ν in the case of a final state muon.

most obvious in the peak and low energy tails, because the HF cross section is larger than the CRPA.

The slight differences can be explained by examining the construction of the distribution. For every value of E_ν the cross section is integrated over a range of lepton energies with corresponding angles. We examine the case of $\bar{E}_\nu = 500$ MeV, the integration bounds in eq. (5.10) are $E_\mu^- = 230$ MeV, and $E_\mu^+ = 465$ MeV. As shown in Fig. 5.1 the lower part of the lepton energy range is considered for $\cos\theta$ in the backward direction, while the higher energies correspond to more forward scattering.

In Fig. 5.5, the double differential cross section that appears in the integrand of eq. (5.10), is shown. The integrand is depicted for $\bar{E}_\nu = 500$ MeV fixed, but for different values of E_ν .

If we now look at $d(E_\nu, \bar{E}_\nu = 500 \text{ MeV})$ For a certain value of E_ν the energy transfer at which the cross section is calculated is given by $\omega = E_\nu - E_l$. As the smallest value for ω yielding a non-zero cross section² is 16 MeV, the smallest E_ν value that can in principle contribute is around 250 MeV. We examine $d(E_\nu, \bar{E}_\nu = 500 \text{ MeV})$, depicted in Fig. 5.4, from left to right:

- For the low-energy tail only the lowest part the lepton energy range will be considered, as the upper bound in eq. (5.10) is given by E_ν as long as $E_\nu < E_l^+$. In the low-energy tail, before the peak, the integrand is considered at low energy transfers and backward scattering angles. The range of energy transfers increases as E_ν increases, and more forward scattering angles are taken into

² The smallest single particle energy

account. The cross section which is integrated for $E_\nu = 325$ MeV is shown in the top left panel of Fig. 5.5. For backward scattering the HF cross section is higher than the CRPA

- The full lepton energy range will be considered at an energy of approximately 475 MeV corresponding to the peak of the distribution. The integrand is depicted in the top right panel of Fig. 5.5. The tails for the most backward scattering angles (high values of ω) are comparable, but the CRPA cross section is smaller, and more strength is due to the narrow peaks.
- Past the peak of the distribution the CRPA cross section is slightly larger in the region of low energy transfer and small scattering angles. Shown in the bottom left panel of Fig. 5.5. This explains why the CRPA distribution is slightly larger for E_ν in this region, most visible for $\bar{E}_\nu = 200$ MeV in Fig. 5.4.
- In the high energy tail of the distribution the cross sections are computed for high energy transfers and the HF and CRPA are basically indistinguishable. The contributing cross section for $E_\nu = 600$ MeV is shown in the bottom right panel of Fig. 5.5

Thus although the cross sections are different in varying parameter regions, the integrated distributions are comparable. The HF cross section is slightly larger than the CRPA, but in terms of shape the distributions are the same.

As a remark we mention that in order to compare the cross sections to data the responses are usually folded with a Lorentzian with a width $\Gamma \approx 3$ MeV as described in [10], and discussed in chapter 2. We have performed this procedure in order to assess its effect on the distributions. The effects are however negligible. As the folding procedure amounts to a redistribution of strength over a rather small region, when integrated no significant differences are found. We therefore will not fold the responses, as it is computationally too taxing.

The most important feature in the distributions are the contributions of the tails. The tails effectively show that in the mean field description the contribution to a certain \bar{E}_ν are spread out over a broad range of energies. There are many energies contributing to a single bin of reconstructed energy.

The distributions $d(E_\nu, \bar{E}_\nu)$ for fixed values of E_ν are shown in Fig. 5.6. Here one sees that when trying to unfold the data the contributions from many reconstructed energies has to be taken into account. The high energy tails effectively transform into contributions of low reconstructed energies. This contrasts the case of a RFG description, in which the cross section is only non-zero in certain parameter regions as we will show in the following section.

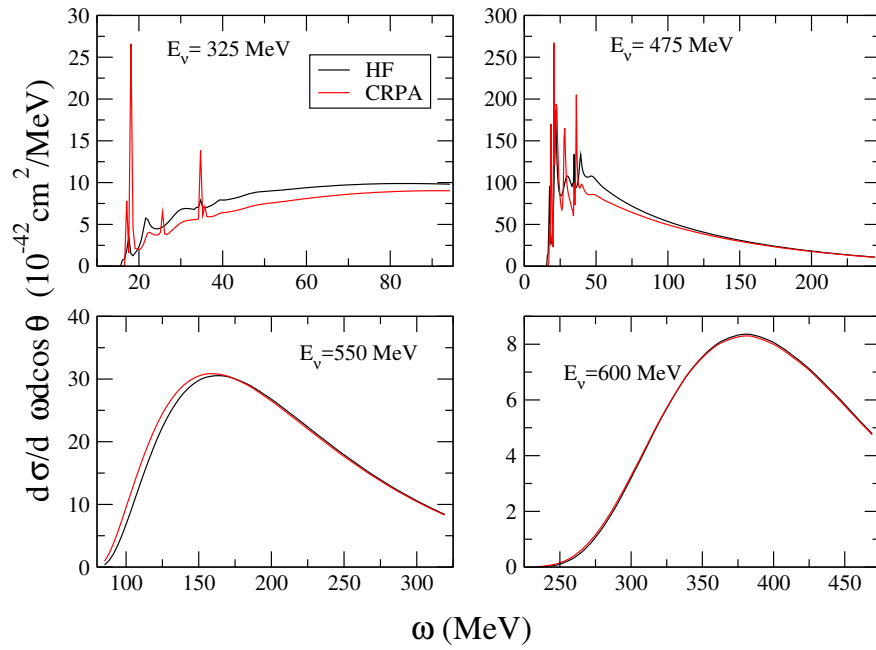


Figure 5.5: Contributions of the cross section to $d(E_\nu, \bar{E}_\nu)$, where $\bar{E}_\nu = 500$ MeV is kept fixed. The value of $d(E_\nu, \bar{E}_\nu)$, for certain values of E_ν as shown in the picture, is obtained by integrating over these cross sections as in eq. (5.10)

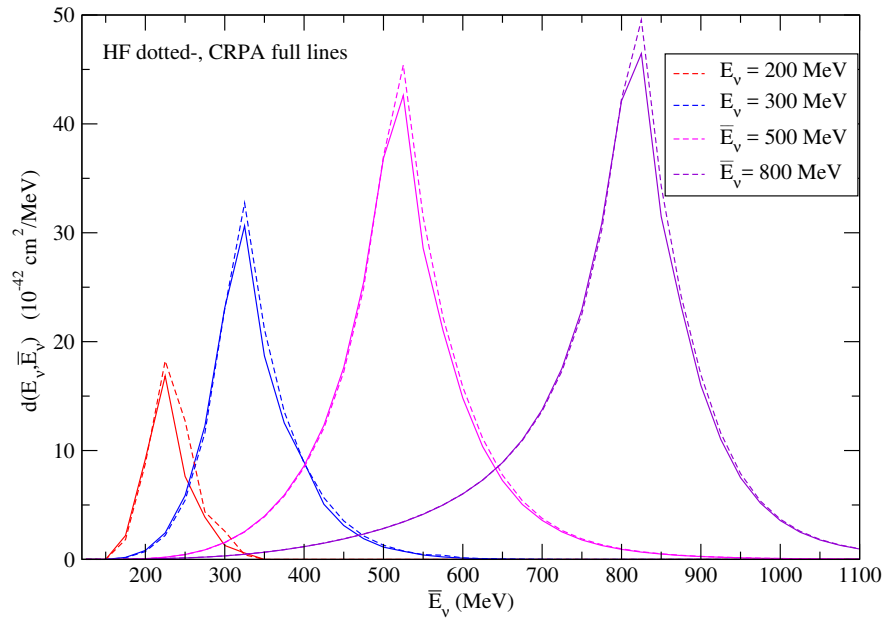


Figure 5.6: $d(E_\nu, \bar{E}_\nu)$ for fixed values of E_ν in the HF (dotted) and CRPA (straight lines) description. The distributions are obtained in terms of bins of \bar{E}_ν with a separation energy of 34 MeV

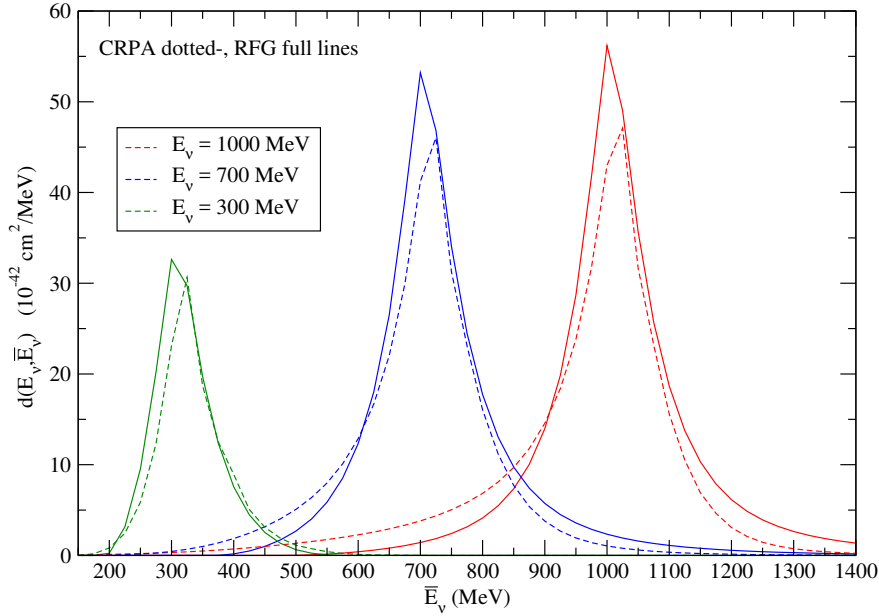


Figure 5.7: $d(E_\nu, \bar{E}_\nu)$ for fixed values of E_ν . The reconstructed energy is defined by eq. (4.2), using a separation energy of $E_b = 34$ MeV. The RFG calculation is based on the model described in [85], with a binding energy included of $E_s = 34$ MeV.

5.3.3 Comparison with the RFG approach and multi-nucleon contributions

As seen in the previous section, were $f(E_\nu, E_l, \cos \theta)^3$ obtained from a RFG was compared to the results from the HF/CRPA model. The mean field approach featured more strength in the tails of the cross section. This is due to the fact that the RFG model has a more limited region of phase space in which its cross section is non-zero. We shall here show the effect this has on the distribution $d(E_\nu, \bar{E}_\nu)$.

First we make the distinction between the separation energy E_B , which is introduced in eq. (4.2), and the energy shift (or binding energy) which we will introduce in the RFG model denoted as E_s . The parameter E_B is used to define the reconstructed energy, and different values of E_B , including $E_B = 0$ MeV, do not change the model in any way. It is through E_s , that a RFG model will be altered to introduce the effect of binding energy of the nucleons.

The comparison is made in Fig. 5.7. The RFG as described in the appendix of [85] was used. In order to facilitate comparison we use the RFG in which a binding energy is introduced through substitution of ω with $\omega_{eff} = \omega - E_s$ with $E_s = 34$ MeV.

One sees that the distributions from the RFG approach are peaked around the reconstructed energy, and are quite symmetric. The peaks of the mean field method are slightly displaced from the reconstructed energy, in favor of the low reconstructed

³ The flux weighted distribution of energies for fixed values of the lepton observables $f(E_\nu, E_l, \cos \theta)$ was defined in eq. (4.3)

energy tail. The high \bar{E}_ν tail is smaller in the CRPA approach due to the threshold energy, and strength is shifted from the peak to the low \bar{E}_ν tails.

From this comparison one thus expects that, even though both models might not differ significantly in terms of the total cross section, the distribution in terms of reconstructed energies will differ. The RFG model as used here can be assumed to resemble the model used to predict data in terms of reconstructed bins, and in unfolding the total cross section in the MiniBooNE experiment [26].

In other works on energy reconstruction [79–81], it was shown that the differences in the pure quasi-elastic cross sections in bins of \bar{E}_ν in comparison to bins of the real energy were insignificant. Also the unfolding procedure based on the RFG was shown to accurately unfold the pure quasi-elastic contributions to the cross section and the focus was set mainly on the discrepancies when including multi-nucleon effects. However in these works the quasi-elastic cross section was modeled according to a RFG in the first place. Here it is obvious that in a mean field model the low reconstructed energy tails can not be reproduced, or unfolded using the RFG model, leading to an increase in events in bins of low reconstructed- or unfolded energy. This result is analogous to the effect multi-nucleon processes have on the reconstructed (or unfolded) energy.

This becomes clear from Fig. 5.8, where the results obtained in the approach of Martini et al. [79] are compared to the results obtained with the CRPA.

In the results of Martini the reconstructed energy is defined by eq. (4.1), which does not include the binding correction. The local Fermi gas in the RPA by Martini does not include a binding energy, the pure quasi-elastic contribution (dashed line) is therefore symmetric around this reconstructed energy without taking into account binding. This is for the same reason as why the RFG distribution (straight line) with a binding energy of $E_s = 34$ MeV in Fig. 5.7 is symmetric around the reconstructed energy including this correction through the separation energy E_B ⁴.

In order to facilitate the comparison with the quasi-elastic and multi-nucleon contribution in Fig 5.8, the CRPA results are calculated for bins defined by eq. (4.2) with $E_b = 34$ MeV. The compared $d(E_\nu, \bar{E}_\nu)$ are thus not defined for the same \bar{E}_ν bins, but the \bar{E}_ν are chosen in such a way that the effect of the binding energy is largely negated in order to focus on the effect of the mean field description in comparison to the multi-nucleon contribution.

This discussion shows that the reconstructed energy \bar{E}_ν which was shown to be rather accurate in comparison to the real energy in a well suited Fermi gas model, is asymmetric in the mean field approach as described here. The reconstructed energy however is not necessarily claimed to be an accurate guess for the real energy, it is the unfolding procedure (which is model-dependent) that in principle gives the most accurate real energy. In this sense it should be noted that if \bar{E}_ν accurately reproduces the real energy, the unfolding procedure is more stable, as there is a smaller spread on the distributions.

⁴ We have shown the effect of the binding energy in eq. (5.2), we shall come back to this point in the next section.

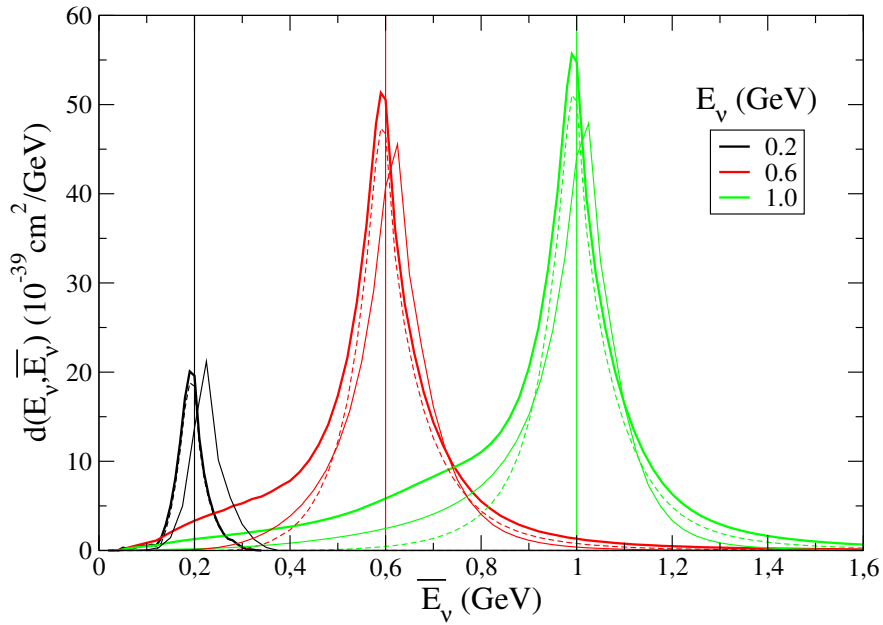


Figure 5.8: Comparison of $d(E_\nu, \bar{E}_\nu)$ in the **CRPA** (thin straight lines) approach compared to the distribution obtained by Martini et al. [81] in the RPA approach (dashed lines). The distributions are calculated for electron neutrinos, the results of Martini are obtained with the simple reconstruction formula without binding energy, while the **CRPA** results do include a binding energy of $E_b = 34$ MeV in the reconstructed energy. Also shown is the multi-nucleon+RPA (thick lines) contribution by Martini.

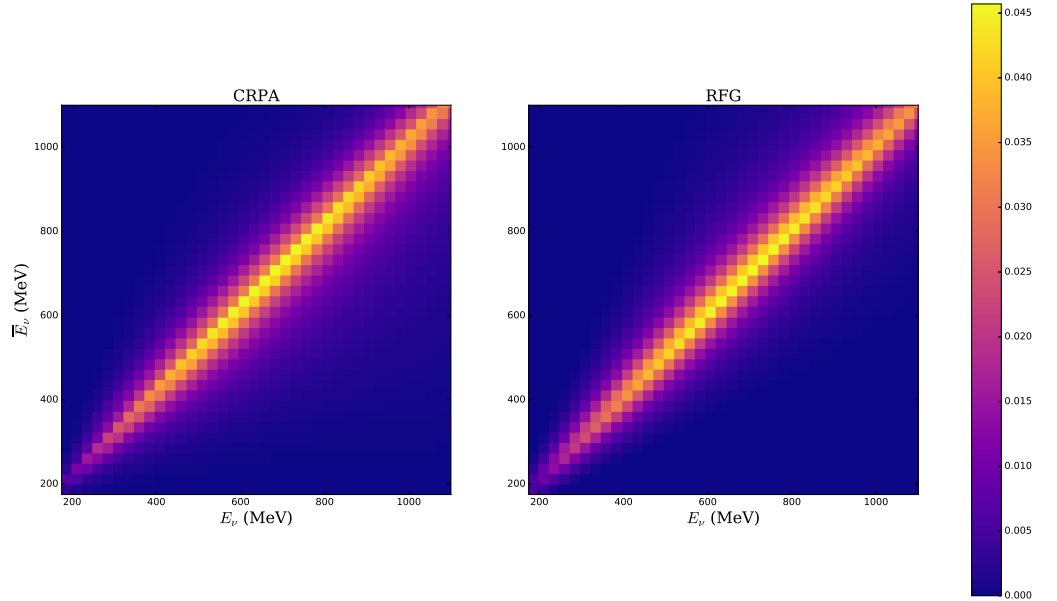


Figure 5.9: The flux weighted distribution $\Phi(E_\nu)d(E_\nu, \bar{E}_\nu)$ in the **RFG** and **CRPA** case. The weighing by the flux suppresses the tails slightly, but the **CRPA** distribution is more diffuse. It can also be seen that the peak of the **CRPA** is slightly off axis by one pixel. One pixel represents a bin of 25 MeV in either \bar{E}_ν , or E_ν . Only the relative scale is important, the unit is arbitrary.

The observable of interest here is the prediction of the amount of events in bins of reconstructed energy. These are obtained by folding $d(E_\nu, \bar{E}_\nu)$ with the flux as shown in eq. (5.11).

When considering the unfolding procedure the matrix which relates the amount of events in terms of reconstructed energies to real energies is related to the flux weighted distribution $\Phi(E_\nu)d(E_\nu, \bar{E}_\nu)$. This distribution is shown in Fig. 5.9 for the **RFG** with $E_b = 34$ MeV and the **CRPA** model. We shall compare the predictions in terms of reconstructed energies in the next section.

5.4 RECONSTRUCTED CROSS SECTIONS

With the discussion in previous sections we have established the differences between the Fermi gas description, with a limited region of nuclear response, and the mean field model in which the response strength is shifted from the peak to the tails.

We shall now use the distributions $d(E_\nu, \bar{E}_\nu)$ to determine the cross section in terms of the reconstructed energy. First we will perform a consistency check and introduce a sharp cut off in the **CRPA** model. We will then look at the influence of the binding

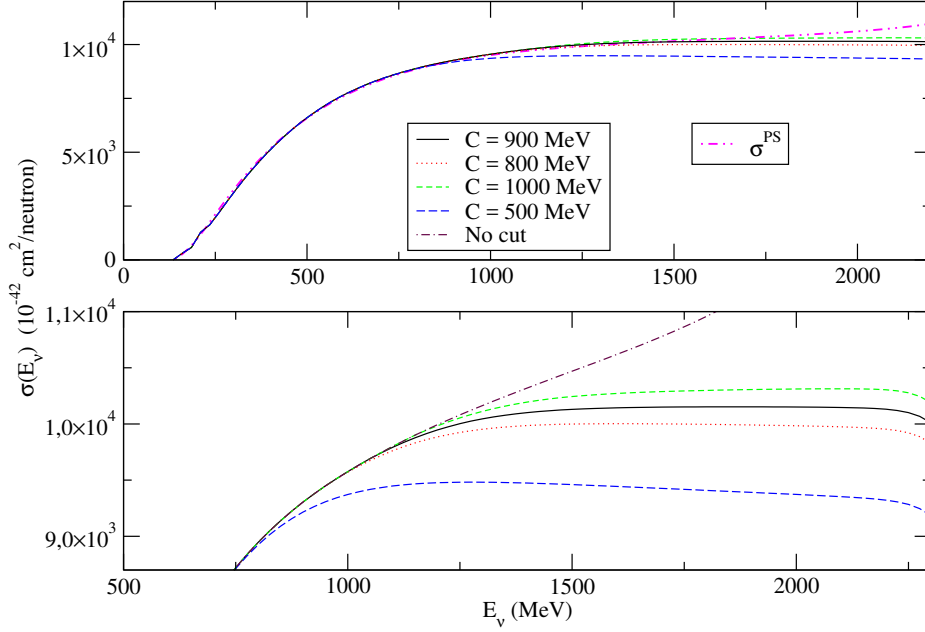


Figure 5.10: The total cross section, σ^{PS} is calculated independently from $d(E_\nu, \bar{E}_\nu)$ by an integration over the phase space of the double differential cross section. The other cross sections are calculated by integrating $d(E_\nu, \bar{E}_\nu)$ over the reconstructed energy, with a hard cut-off C (explained in the text). In the top panel these cross sections have been shifted by 10 MeV. All cross sections are obtained in the HF approach, the results for CRPA are analogous.

energy E_B in the reconstruction formula eq. (4.2) in terms of reconstructed cross sections and explain its influence. Then we have all elements in place to compare the distribution of reconstructed energies with the Fermi gas prediction. Finally we shall also perform the approximate unfolding procedure as outlined in [80].

5.4.1 Cross sections in terms of real energies

A consistency check of the validity of $d(E_\nu, \bar{E}_\nu)$ is obtained by

$$\sigma(E_\nu) = \int d\bar{E}_\nu d(E_\nu, \bar{E}_\nu) = \int d\bar{E}_\nu \frac{d\sigma(E_\nu, \bar{E}_\nu)}{d\bar{E}_\nu}. \quad (5.20)$$

We compare the cross section obtained by this method with the cross section obtained independently by integrating the double differential cross section over the phase space which we denote as

$$\sigma^{PS}(E_\nu) = \int \int d\Omega d\omega \frac{d\sigma}{d\Omega d\omega} \quad (5.21)$$

in Fig. 5.10.

Some problems are present in the evaluation of the total cross section. The cross-sections for high energies require many multipoles to be taken in consideration, this makes calculation of the high energy cross section uncertain. In comparing with the cross section σ^{PS} , the cross sections σ have to be shifted by ≈ 10 MeV to the right in order to align in the low energy regime. The cross sections in the upper panel are shifted by this amount. Another problem is that σ diverges for high energies, to nullify the divergence we implement a sharp cut-off by setting

$$d(E_\nu, \bar{E}_\nu) = 0 \text{ if } E_\nu - \bar{E}_\nu > C. \quad (5.22)$$

This effectively removes parts of the high energy tail.

The cut-off can also be understood as a cut in terms of ω by writing $E_\nu = \omega + E_l$. Further, the upper bound for E_l is $E_l^+ \leq \bar{E}_\nu$, with E_l^+ approaching \bar{E}_ν . This gives approximately for the upper bound of the integration range, corresponding to the smallest value of ω

$$\omega_{min} + E_l^+ - \bar{E}_\nu \approx \omega_{min} > C. \quad (5.23)$$

Meaning that the cross-section is set to zero, once the smallest ω in the integration range is larger than C .

The bottom panel shows the effect of the sharp cut on the cross section in detail. The regularization of the high energy cross section has to be further investigated in terms of the calculation from reconstructed energies. In any way the sharp cut-off drastically reduces the strength in the tails of the distribution. For every cut-off the cross section at higher energies is underestimated.

We shall calculate reconstructed distributions for different cut-offs to give an idea of the effect due to the heavy tails, but further analysis, and inclusion of the multi-nucleon component is necessary to perform a proper analysis of data.

5.4.2 Influence of the binding energy

We will briefly revisit the effect of the separation energy E_B in the reconstruction formula eq. (4.2) on the obtained distributions in terms of reconstructed variables.

We again denote by E_s the shift in the RFG model in order to implement binding energy by substituting ω with $\omega_{eff} = \omega - E_s$. The parameter E_B , which is unrelated to the shift, defines the reconstructed energy by eq. (4.2).

In Fig. 5.11, the top panel is obtained using a RFG where $E_s = 0$, while in the bottom panel $E_s = 34$ MeV is introduced. The total cross section $\sigma(E_\nu)$ is calculated as

$$\sigma(E_\nu) = \int d\bar{E}_\nu d(E_\nu, \bar{E}_\nu) \quad (5.24)$$

while the effective cross section σ_{eff} is related to the distribution of reconstructed energies by considering that

$$N(\bar{E}_\nu) = \int dE_\nu d(E_\nu, \bar{E}_\nu) \Phi(E_\nu), \quad (5.25)$$

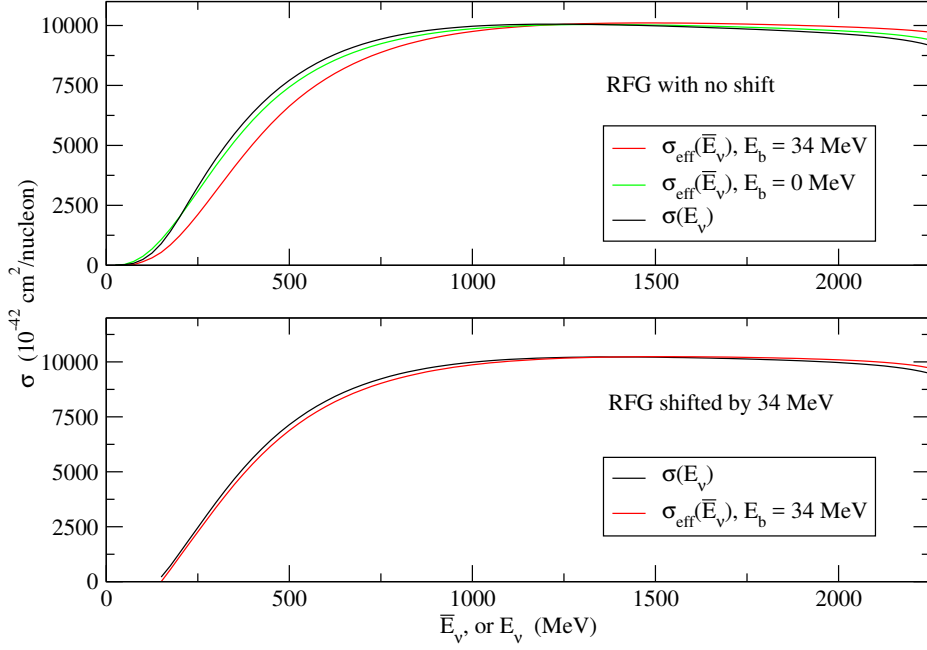


Figure 5.11: The top panel shows the cross section $\sigma(E_\nu)$ and reconstructed distributions $\sigma_{eff}(\bar{E}_\nu)$ in a RFG without any energy shift (i.e. $E_s = 0$). For different values of E_B in the definition of \bar{E}_ν in eq. (4.2). The bottom panel shows the same but for a RFG where $\omega_{eff} = \omega - 34$ MeV was used.

gives the number of events in bins of reconstructed energies. Here σ_{eff} is defined as the distribution of reconstructed energies for a unit flux $\Phi(E_\nu) = 1 \text{ MeV}^{-1}$

$$\sigma_{eff}(\bar{E}_\nu) = \int dE_\nu d(E_\nu, \bar{E}_\nu). \quad (5.26)$$

It thus represents the number of events in bins of reconstructed energies, if every value of the energy has equal probability, measured in units of a cross section.

One sees in Fig. 5.11 that if $E_s = E_b$ the difference between $\sigma_{eff}(\bar{E}_\nu)$ and $\sigma(E_\nu)$ is a very small shift towards higher energies. When however one considers the model with $E_s = 0$, while the reconstructed bins are defined with $E_b = 34$ MeV, one sees a sizeable shift towards higher values of \bar{E}_ν . This shows that the cross section in terms of reconstructed energy is sensitive to the parameter E_s .

To have as little spread as possible in the distributions of reconstructed energy, the binding energy E_b could be tuned to the corresponding model. However in order to accurately compare with data in bins of reconstructed energy, the binding energy defining the bins E_B should be set to the same value as the one used by the experiment.

In the discussion [80], it is unclear whether the binding energy correction was implemented in the reconstruction formula, non-inclusion of this parameter might introduce a systematic shift in the reconstructed distribution, and therefore also in

the unfolded distribution. This effect however can be considered minor in comparison to the two-nucleon knock-out contribution, but in order to accurately unfold the cross section to compare with data it should be taken into account.

5.4.3 Distribution of reconstructed energies in the mean field model

We shall now present the cross section in terms of reconstructed energies in the [CRPA](#) model. The number of events for a certain reconstructed energy, given by eq. (5.25), is computed for a normalized flux such that it has unit $\text{cm}^2\text{Mev}^{-2}$, it will be denoted as

$$\sigma(\bar{E}_\nu) = \int dE_\nu \Phi(E_\nu) d(E_\nu, \bar{E}_\nu) \quad (5.27)$$

where $\Phi(E_\nu)$ is the normalized [MiniBooNE](#) flux. The absolute number of events is then found by multiplying with the integrated absolute flux.

The distinction between the cross section $\sigma(E_\nu)$ and the above defined $\sigma(\bar{E}_\nu)$ is made by the explicit notation of the argument.

The [RFG](#) model which is used in comparison was shifted by $E_s = 34$ MeV in the same way as previously described.

In order to facilitate comparison, the cross section in terms of the real energies as found from integrating $d(E_\nu, \bar{E}_\nu)$ over the reconstructed energy is shown in Fig. 5.12. The top panel shows the total cross section, the bottom panel is the cross section weighed with the [MiniBooNE](#) ν_μ -flux [8]. This cross section is presented in terms of real energies. Here the [RFG](#) cross section is larger up until $E_\nu \approx 1.2$ GeV, than the [CRPA](#).

From the lower panel one sees that around the peak of the flux folded cross section, the difference due to the cut-off is very small.

The cross section $\sigma(\bar{E}_\nu)$, in terms of \bar{E}_ν , looks different as can be appreciated from Fig. 5.13. The flux-weighted cross section $\Phi(E_\nu)\sigma(E_\nu)$ is depicted in the left panel for the [RFG](#) model, and the [CRPA](#) cut by $C = 500$, and 1000 MeV. The right panel shows $\sigma(\bar{E}_\nu)$ defined in eq. (5.27) for the same models.

The position of the peak of the [RFG](#) distribution is unchanged, but the peak strength diminishes slightly in favor off higher energies. The [CRPA](#) peak, and strength of the distribution is shifted to lower energies, while the high energy tail is strongly quenched.

Even though $\Phi(E_\nu)\sigma(E_\nu)$ for the [RFG](#) is larger for almost every energy in the left panel, the [CRPA](#) predicts more events around the peak of the flux, and in the low- \bar{E}_ν region when considering $\sigma(\bar{E}_\nu)$. The effect is reminiscent of the effect of multi-nucleon contributions, the mechanism can also be considered the same, i.e. the asymmetry in $d(E_\nu, \bar{E}_\nu)$, leading to high E_ν tails for fixed \bar{E}_ν , mean that the distribution of reconstructed energies is skewed towards smaller values of \bar{E}_ν . The effect remains even when $C = 500$ MeV. This affects the unfolding procedure as well, the cross

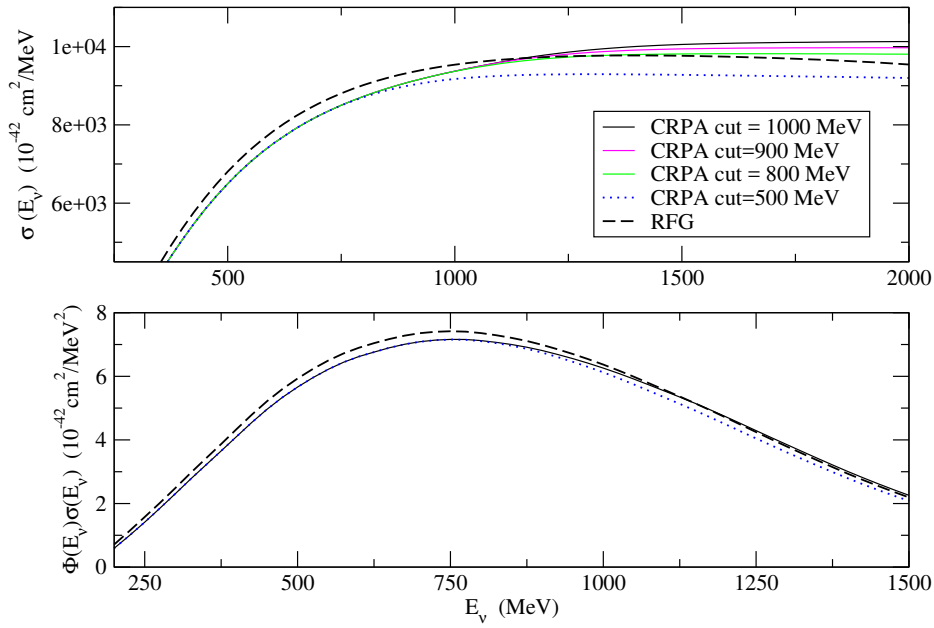


Figure 5.12: The (flux weighted) cross section in the RFG and CRPA for different cut-offs is shown in the top(bottom) panel.

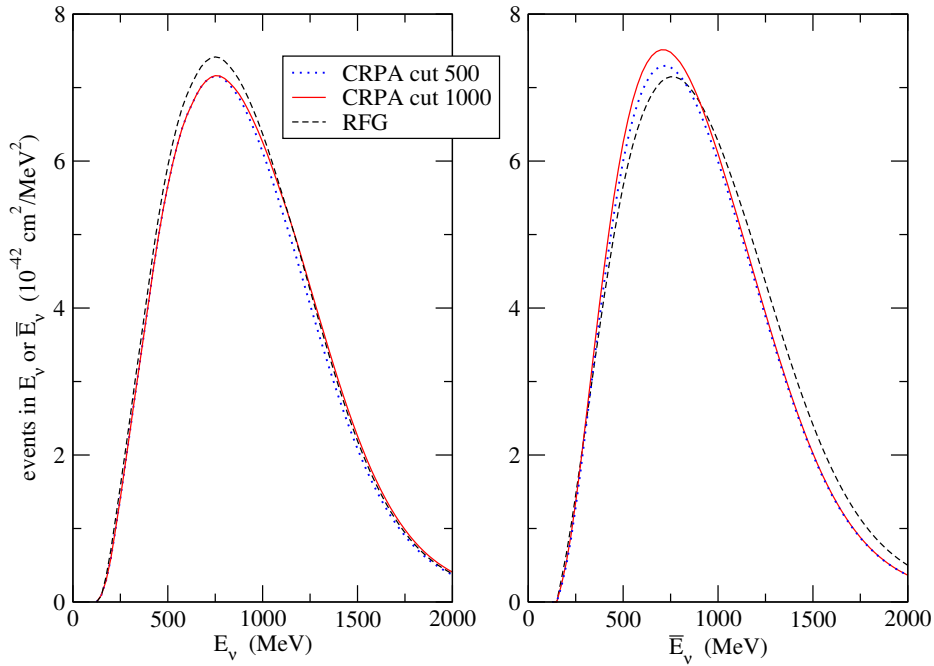


Figure 5.13: The MiniBooNE flux-folded cross sections in terms of E_ν and \bar{E}_ν . The number of events predicted in terms of real energies is shown on the left, in terms of reconstructed energies on the right.

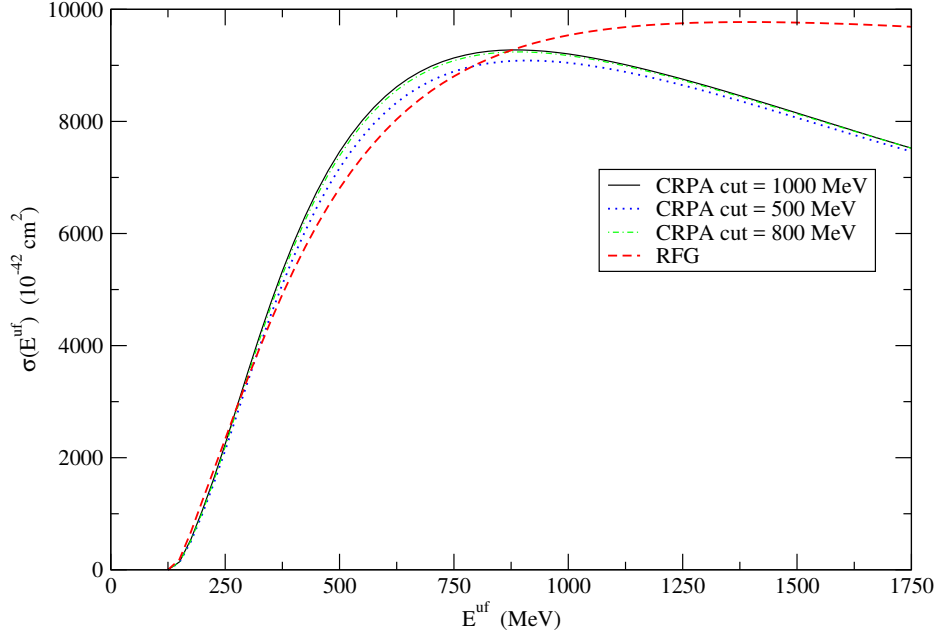


Figure 5.14: The unfolded cross sections according to eq. (5.28). The CRPA model, for different cut-offs C , is unfolded using a RFG prediction. Also shown is the unfolded RFG prediction, which is left invariant by the procedure.

section in terms of unfolded energies is shown in 5.14. The unfolding procedure is described in eq. (5.16) and comes down to the following quantity

$$\sigma(E_v^{uf}) = \int d\bar{E}_v \left\{ \int dE_v \Phi(E_v) d(E_v, \bar{E}_v) \right\} \times \left[\frac{\frac{d\sigma}{d\bar{E}_v}(E_v, \bar{E}_v)}{\int dE_v \Phi(E_v) \frac{d\sigma}{d\bar{E}_v}} \right]^{RFG}. \quad (5.28)$$

The unfolding is always performed with the RFG model to compute the term between brackets. The term between braces is the distribution that is being unfolded, in this case $\sigma(\bar{E}_v)$, as defined by eq. (5.27).

The result of the unfolding procedure is shown in Fig. 5.14, for the RFG, and CRPA with different cut-offs C .

A consistency check is obtained by noting that the unfolding of the RFG model reproduces the cross section as expected, i.e. $\sigma(E_v) = \sigma(E_v^{uf})$. Further one sees that $\sigma(E_v^{uf})$ for the CRPA, is not representative of $\sigma(E_v)$, this was anticipated, additional strength is found for lower E_v^{uf} , while the cross section falls rapidly in the high energy region. The unfolding of the mean field CRPA with a RFG model deforms the cross section, again due to the tails in $d(E_v, \bar{E}_v)$.

CONCLUSION

In order to fully understand the neutrino and their mass-mixing, a multitude of different neutrino-nucleus scattering experiments have set out to measure neutrino oscillations. The targets in accelerator-based experiments are nuclei, and the incoming energy of the neutrino is spread out over a large energy region. Detection of the neutrino, through charged-current (quasi-elastic) scattering, is often possible only through inclusive measurements, where the state of the nuclear system, including the outgoing nucleon, remain unobserved. As neutrino oscillations are dependent on E_ν/L , measurement of the oscillation parameters requires accurate knowledge of the neutrino energy. Because of the inclusiveness of measurements, and the large spread in the neutrino flux, modeling of the neutrino-nucleus interaction is necessary in order to accurately determine this energy.

Recent developments have shown that different nuclear models can severely influence the interpretation of data, not only in analysis of neutrino oscillations, but also from a nuclear modeling standpoint. It has been accepted that in order to determine the neutrino energy in the few-GeV region, many effects beyond the impulse approximation play an important role.

Inclusion of multi-nucleon knock-out contributions, short- and long-range correlations, final-state interactions, etc. have a non-trivial effect on the reconstruction- and unfolding procedures used to determine the distribution of neutrino energies.

In *chapter four* we have carefully described the quasi-elastic reconstruction procedure, in which the reconstructed energy $\bar{E}_\nu(\cos\theta, E_l)$ is determined by the observables in an inclusive charged-current scattering event

$$\bar{E}_\nu(\cos\theta, E_l) = \frac{2M'_n E_l - ((M'_n)^2 + m_l^2 - M_p^2)}{2(M'_n - E_l + P_l \cos\theta)}.$$

Here $M'_n = M_n - E_B$, where M_n is the neutron mass, and E_B is the separation energy.

Different energies contribute to a single value of the reconstructed energy. And the distribution of these energies has been the main subject of this work.

First we examined the distribution of energies for fixed values of E_l and $\cos\theta$ obtained in different nuclear models. In this way it becomes clear how the contributions to a single value of the reconstructed energy may differ.

It is noted that the distribution of energies E_ν which contribute to a certain \bar{E}_ν , can differ significantly between different nuclear models. This is even the case in kinematic regions where different cross-sections, considered at the same energy E_ν , produce equivalent results in strength and shape that are however in different positions along the ω -axis. When this is the case, the total cross-section for a fixed E_ν ,

considered in some angular bin, $\sigma(E_\nu)$ will not differ significantly, however $\sigma(\bar{E}_\nu)$ will.

Comparing the Continuum Random Phase Approximation (CRPA), and Hartree Fock (HF) results, with different (local) Relativistic Fermi Gas (RFG) models, it is immediately obvious that these mean field predictions feature a more spread-out distribution of E_ν for fixed lepton observables. This is due to the fact that the RFG-based models have a more limited region in which the nuclear response is non-zero.

In *Chapter five*, the procedure for constructing the cross-section, single differential in \bar{E}_ν , is outlined using the same conventions as in [81]. Care is taken in correctly implementing and analyzing the effects of the separation energy E_B , in the definition of \bar{E}_ν .

We then outlined how $d(E_\nu, \bar{E}_\nu)$, can be used to predict the experimentally measurable distribution of \bar{E}_ν . Also the unfolding procedure outlined in [80], was touched upon.

The influence of E_B was assessed; the separation energy induces shifts in $d(E_\nu, \bar{E}_\nu)$. In a RFG model, which is tuned to have the same binding energy as E_B , the cross section is similar in terms of \bar{E}_ν as in E_ν . However when the energy shift in the model is not comparable to E_B , the cross section in terms of \bar{E}_ν is shifted in comparison to the one in E_ν .

The distributions $d(E_\nu, \bar{E}_\nu)$ obtained in the HF/CRPA approach, and (local) RFG models, were compared. The mean-field descriptions feature a larger spread in E_ν for fixed values of \bar{E}_ν and vice-versa, again to be expected as the RFG models have a limited region of response. It is shown that the flux-folded distribution of events in terms of reconstructed energies

$$N(\bar{E}_\nu) = \int dE_\nu \Phi(E_\nu) d(E_\nu, \bar{E}_\nu),$$

measurable in experiments, is enhanced for low values of \bar{E}_ν . The amount of events are redistributed from higher reconstructed energies towards lower values of \bar{E}_ν . This effect is due to the large- E_ν tails in $d(E_\nu, \bar{E}_\nu)$ for fixed values of \bar{E}_ν . The influence of the high E_ν tails are quenched by the flux, and in addition we have introduced a sharp cut-off of these high E_ν at various energies C by setting

$$d(E_\nu, \bar{E}_\nu) = 0, \quad \text{if } E_\nu - \bar{E}_\nu > C.$$

The redistribution is less pronounced for smaller cut-offs, but it remains present even for the smallest cut-off considered $C = 500$ MeV. This cut leads to a underprediction of the total cross section

$$\sigma(E_\nu) = \int d\bar{E}_\nu d(E_\nu, \bar{E}_\nu).$$

The flux-folded distribution of (reconstructed) energies is shown on the left (right) in Fig. 6.1. The cross section in terms of E_ν in the RFG model is larger then the CRPA

cross section as can be seen from the left panel. When considering the right panel, the cross section in terms of reconstructed energies, which can be measured in an experiment, the CRPA cross section features more strength around the peak, and the low energy tail, while the high- \bar{E}_ν cross-section is quenched. The position of the peak is slightly shifted towards lower \bar{E}_ν . The peak-position of the RFG cross section is the same in both cases, but the reconstructed cross section features slightly more strength in the high \bar{E}_ν region.

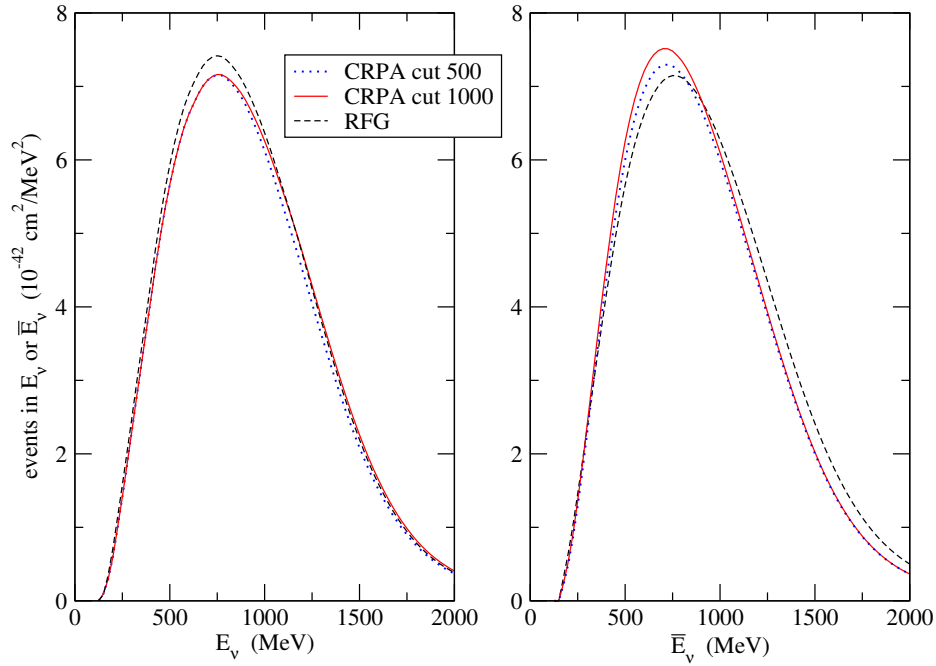


Figure 6.1: Same as Fig. 5.13. Comparison of the flux-folded cross section in terms of neutrino energy E_ν with the cross section in terms of \bar{E}_ν .

OUTLOOK

Systematic uncertainties in the calculation of $d(E_\nu, \bar{E}_\nu)$, should firstly be considered.

The total cross section as obtained from $d(E_\nu, \bar{E}_\nu)$ should exactly reproduce the cross section found by a straightforward integration over the phase space. Here, the shape is reproduced exactly but the former seems to be shifted by ≈ 10 MeV.

The reconstructed energy \bar{E}_ν depends on contributions of many energies. Therefore the cross section for relatively high energies also contribute, even to the low- \bar{E}_ν distribution. Analysis of the contribution of different multipoles needs to be revisited to be confident of the high E_ν cross section. If necessary a better cut-off in terms of ω , and q^2 should be implemented.

The range of validity of the semi-relativistic correction through substitution of

$$\lambda \rightarrow \lambda(1 + \lambda),$$

is also of interest in this analysis.

Analysis of the [CRPA](#) flux-folded double differential cross section shows that the data in forward scattering bins is well reproduced, but strength seems to be lacking in backward bins [31].

An analysis in angular bins should be undertaken, the results described here consider the whole $(E_l, \cos\theta)$ -space. These angular cuts will produce different $d(E_\nu, \bar{E}_\nu)$ for the [CRPA](#) and the [HF](#), which in this work only resemble each other because we consider all angles and lepton energies. Much more can be learned by looking at a restricted part of the phase space.

Also experimental data does often not describe the full angular distribution, for example the Tokai-to-Kamiokande ([T2K](#)) near detector has a limited angular acceptance, and can only detect forward scattered leptons.

Fully exclusive measurements of the Charged-Current Quasi Elastic ([CCQE](#)) cross section are needed to further constrain different nuclear models. These measurements could be made in the near future in Liquid Argon Time Projection Chamber ([LArTPC](#)) detectors. However, the exclusive cross sections are strongly dependent on the FSI of the outgoing nucleon(s). There are multiple choices for models by which FSI could be implemented, which would have different implications for the kinematics of the final state nucleon.

The optimal experimental conditions would be a mono-energetic neutrino beam, combined with exclusive measurements of the final-state. A mono-energetic neutrino beam could be obtained from the decay of charged mesons that are at rest into $l\nu_l$, therefore the energy of the neutrino beam is determined by the rest mass of the decaying meson. Such a beam would also be an opportunity in oscillation experiments, specifically as proposed in [93, 94] to examine the LSND, and Miniature Booster Neutrino Experiment ([MiniBooNE](#)) signals [72, 83].

The [CRPA](#) model used here is not complete in the sense that it does not include multi-nucleon knock out, SRC, full FSI¹, Δ -excitations etc. In order to confront the model with data in terms of reconstructed energies these contributions have to be implemented, or their effects should at least be carefully assessed.

¹ FSI are partially implemented due to the calculation of the outgoing nucleon wave function in the potential of the residual nucleus.

BIBLIOGRAPHY

- [1] F. Reines and C. L. Cowan. "Detection of the Free Neutrino." In: *Phys. Rev.* 92 (3 1953), pp. 830–831. DOI: [10.1103/PhysRev.92.830](https://doi.org/10.1103/PhysRev.92.830). URL: <https://link.aps.org/doi/10.1103/PhysRev.92.830>.
- [2] G. Danby, J-M. Gaillard, K. Goulianos, L. M. Lederman, N. Mistry, M. Schwartz, and J. Steinberger. "Observation of High-Energy Neutrino Reactions and the Existence of Two Kinds of Neutrinos." In: *Phys. Rev. Lett.* 9 (1 1962), pp. 36–44. DOI: [10.1103/PhysRevLett.9.36](https://doi.org/10.1103/PhysRevLett.9.36). URL: <https://link.aps.org/doi/10.1103/PhysRevLett.9.36>.
- [3] K. Kodama et al. "Observation of tau neutrino interactions." In: *Physics Letters B* 504.3 (2001), pp. 218–224. ISSN: 0370-2693. DOI: [https://doi.org/10.1016/S0370-2693\(01\)00307-0](https://doi.org/10.1016/S0370-2693(01)00307-0). URL: <http://www.sciencedirect.com/science/article/pii/S0370269301003070>.
- [4] Bruce T. Cleveland, Timothy Daily, Jr. Raymond Davis, James R. Distel, Kenneth Lande, C. K. Lee, Paul S. Wildenhain, and Jack Ullman. "Measurement of the Solar Electron Neutrino Flux with the Homestake Chlorine Detector." In: *The Astrophysical Journal* 496.1 (1998), p. 505. URL: <http://stacks.iop.org/0004-637X/496/i=1/a=505>.
- [5] John N. Bahcall, Aldo M. Serenelli, and Sarbani Basu. "New Solar Opacities, Abundances, Helioseismology, and Neutrino Fluxes." In: *The Astrophysical Journal Letters* 621.1 (2005), p. L85. URL: <http://stacks.iop.org/1538-4357/621/i=1/a=L85>.
- [6] *Sudbury neutrino observatory*. URL: <http://www.sno.phy.queensu.ca/>.
- [7] *Super-Kamiokande*. URL: <http://www-sk.icrr.u-tokyo.ac.jp/sk/index-e.html>.
- [8] A. A. Aguilar-Arevalo et al. "Neutrino flux prediction at MiniBooNE." In: *Phys. Rev. D* 79 (7 2009), p. 072002. DOI: [10.1103/PhysRevD.79.072002](https://doi.org/10.1103/PhysRevD.79.072002). URL: <https://link.aps.org/doi/10.1103/PhysRevD.79.072002>.
- [9] A. A. Aguilar-Arevalo et al., MiniBooNE Collaboration. "First measurement of the muon neutrino charged current quasielastic double differential cross section." In: *Phys. Rev. D* 81 (9 2010), p. 092005. DOI: [10.1103/PhysRevD.81.092005](https://doi.org/10.1103/PhysRevD.81.092005). URL: <https://link.aps.org/doi/10.1103/PhysRevD.81.092005>.
- [10] V. Pandey, N. Jachowicz, T. Van Cuyck, J. Ryckebusch, and M. Martini. "Low-energy excitations and quasielastic contribution to electron-nucleus and neutrino-nucleus scattering in the continuum random-phase approximation." In: *Phys. Rev. C* 92 (2 2015), p. 024606. DOI: [10.1103/PhysRevC.92.024606](https://doi.org/10.1103/PhysRevC.92.024606). URL: <https://link.aps.org/doi/10.1103/PhysRevC.92.024606>.

- [11] C. Patrignani et al. “Status of Higgs Boson Physics.” In: *Chin. Phys. C* 40 (2016).
- [12] E.A. Paschos. *Electroweak Theory*. Cambridge University Press, 2007. ISBN: 9780511273971. URL: <https://books.google.be/books?id=JKDgngEACAAJ>.
- [13] S. M. Bilenky and S. T. Petcov. “Massive neutrinos and neutrino oscillations.” In: *Rev. Mod. Phys.* 59 (3 1987), pp. 671–754. DOI: [10.1103/RevModPhys.59.671](https://doi.org/10.1103/RevModPhys.59.671). URL: <https://link.aps.org/doi/10.1103/RevModPhys.59.671>.
- [14] A. Zee. “A theory of lepton number violation and neutrino Majorana masses.” In: *Physics Letters B* 93.4 (1980), pp. 389–393. ISSN: 0370-2693. DOI: [http://dx.doi.org/10.1016/0370-2693\(80\)90349-4](https://doi.org/10.1016/0370-2693(80)90349-4). URL: <http://www.sciencedirect.com/science/article/pii/0370269380903494>.
- [15] J. Schechter and J. W. F. Valle. “Neutrino masses in $SU(2) \otimes U(1)$ theories.” In: *Phys. Rev. D* 22 (9 1980), pp. 2227–2235. DOI: [10.1103/PhysRevD.22.2227](https://doi.org/10.1103/PhysRevD.22.2227). URL: <https://link.aps.org/doi/10.1103/PhysRevD.22.2227>.
- [16] Hiroshi Nunokawa, Stephen Parke, and José W.F. Valle. “{CP} violation and neutrino oscillations.” In: *Progress in Particle and Nuclear Physics* 60.2 (2008), pp. 338–402. ISSN: 0146-6410. DOI: <https://doi.org/10.1016/j.pnpnp.2007.10.001>. URL: <http://www.sciencedirect.com/science/article/pii/S014664100700083X>.
- [17] Carlo Giunti and Chung W. Kim. *Fundamentals of Neutrino Physics and Astrophysics*. Oxford University Press, 2007. DOI: [10.1093/acprof:oso/9780198508717.001.0001](https://doi.org/10.1093/acprof:oso/9780198508717.001.0001).
- [18] Frank T. Avignone, Steven R. Elliott, and Jonathan Engel. “Double beta decay, Majorana neutrinos, and neutrino mass.” In: *Rev. Mod. Phys.* 80 (2 2008), pp. 481–516. DOI: [10.1103/RevModPhys.80.481](https://doi.org/10.1103/RevModPhys.80.481). URL: <https://link.aps.org/doi/10.1103/RevModPhys.80.481>.
- [19] M.C. Gonzalez-Garcia and Michele Maltoni. “Phenomenology with massive neutrinos.” In: *Physics Reports* 460.1–3 (2008), pp. 1–129. ISSN: 0370-1573. DOI: <https://doi.org/10.1016/j.physrep.2007.12.004>. URL: <http://www.sciencedirect.com/science/article/pii/S0370157308000148>.
- [20] N. Jachowicz, K. Heyde, J. Ryckebusch, and S. Rombouts. “Continuum random phase approximation approach to charged-current neutrino-nucleus scattering.” In: *Phys. Rev. C* 65 (2 2002), p. 025501. DOI: [10.1103/PhysRevC.65.025501](https://doi.org/10.1103/PhysRevC.65.025501). URL: <https://link.aps.org/doi/10.1103/PhysRevC.65.025501>.
- [21] G.T. Garvey, D.A. Harris, H.A. Tanaka, R. Tayloe, and G.P. Zeller. “Recent advances and open questions in neutrino-induced quasi-elastic scattering and single photon production.” In: *Physics Reports* 580 (2015). Recent advances and open questions in neutrino-induced quasi-elastic scattering and single photon production, pp. 1–45. ISSN: 0370-1573. DOI: <https://doi.org/10.1016/j.physrep.2015.04.001>. URL: <http://www.sciencedirect.com/science/article/pii/S0370157315002112>.

- [22] C.H. Llewellyn Smith. “Neutrino reactions at accelerator energies.” In: *Physics Reports* 3.5 (1972), pp. 261–379. ISSN: 0370-1573. DOI: [http://dx.doi.org/10.1016/0370-1573\(72\)90010-5](http://dx.doi.org/10.1016/0370-1573(72)90010-5). URL: <http://www.sciencedirect.com/science/article/pii/0370157372900105>.
- [23] R. P. Feynman and M. Gell-Mann. “Theory of the Fermi Interaction.” In: *Phys. Rev.* 109 (1 1958), pp. 193–198. DOI: [10.1103/PhysRev.109.193](https://link.aps.org/doi/10.1103/PhysRev.109.193). URL: <https://link.aps.org/doi/10.1103/PhysRev.109.193>.
- [24] C.F. Perdrisat, V. Punjabi, and M. Vanderhaeghen. “Nucleon electromagnetic form factors.” In: *Progress in Particle and Nuclear Physics* 59.2 (2007), pp. 694–764. ISSN: 0146-6410. DOI: <http://dx.doi.org/10.1016/j.pnnp.2007.05.001>. URL: <http://www.sciencedirect.com/science/article/pii/S0146641007000610>.
- [25] P. Bopp, D. Dubbers, L. Hornig, E. Klemt, J. Last, H. Schütze, S. J. Freedman, and O. Schärpf. “Beta-Decay Asymmetry of the Neutron and $\frac{g_A}{g_V}$.” In: *Phys. Rev. Lett.* 56 (9 1986), pp. 919–922. DOI: [10.1103/PhysRevLett.56.919](https://link.aps.org/doi/10.1103/PhysRevLett.56.919). URL: <https://link.aps.org/doi/10.1103/PhysRevLett.56.919>.
- [26] A. A. Aguilar-Arevalo et al. “First measurement of the muon neutrino charged current quasielastic double differential cross section.” In: *Phys. Rev. D* 81 (9 2010), p. 092005. DOI: [10.1103/PhysRevD.81.092005](https://link.aps.org/doi/10.1103/PhysRevD.81.092005). URL: <https://link.aps.org/doi/10.1103/PhysRevD.81.092005>.
- [27] Véronique Bernard, Latifa Elouadrhiri, and Ulf-G Meißner. “Axial structure of the nucleon.” In: *Journal of Physics G: Nuclear and Particle Physics* 28.1 (2002), R1. URL: <http://stacks.iop.org/0954-3899/28/i=1/a=201>.
- [28] R. Bradford, A. Bodek, H. Budd, and J. Arrington. “A New Parameterization of the Nucleon Elastic Form Factors.” In: *Nuclear Physics B - Proceedings Supplements* 159 (2006). Proceedings of the 4th International Workshop on Neutrino-Nucleus Interactions in the Few-GeV Region, pp. 127–132. ISSN: 0920-5632. DOI: <http://dx.doi.org/10.1016/j.nuclphysbps.2006.08.028>. URL: <http://www.sciencedirect.com/science/article/pii/S0920563206005184>.
- [29] J.D. Walecka. *Theoretical Nuclear and Subnuclear Physics*. Imperial College Press, 2004. ISBN: 9789812388988.
- [30] J. S. O’Connell, T. W. Donnelly, and J. D. Walecka. “Semileptonic Weak Interactions with C^{12} .” In: *Phys. Rev. C* 6 (3 1972), pp. 719–733. DOI: [10.1103/PhysRevC.6.719](https://link.aps.org/doi/10.1103/PhysRevC.6.719). URL: <https://link.aps.org/doi/10.1103/PhysRevC.6.719>.
- [31] Tom Van Cuyck. “Short-range correlations and meson-exchange currents in neutrino-nucleus scattering.” eng. PhD thesis. Ghent University, 2017.
- [32] N. Jachowicz, S. Rombouts, K. Heyde, and J. Ryckebusch. “Cross sections for neutral-current neutrino-nucleus interactions: Applications for ^{12}C and ^{16}O .” In: *Phys. Rev. C* 59 (6 1999), pp. 3246–3255. DOI: [10.1103/PhysRevC.59.3246](https://link.aps.org/doi/10.1103/PhysRevC.59.3246). URL: <https://link.aps.org/doi/10.1103/PhysRevC.59.3246>.

- [33] Christophe Praet. "Modeling quasi-free neutrino-nucleus reactions for accelerator-based experiments." eng. PhD thesis. Ghent University, 2009.
- [34] M. Waroquier, J. Sau, K. Heyde, P. Van Isacker, and H. Vincx. "Extended-Skyrme-force calculation: Theoretical description and application to Ca and Sn isotopes." In: *Phys. Rev. C* 19 (5 1979), pp. 1983–2001. DOI: [10.1103/PhysRevC.19.1983](https://doi.org/10.1103/PhysRevC.19.1983). URL: <https://link.aps.org/doi/10.1103/PhysRevC.19.1983>.
- [35] M. Waroquier, K. Heyde, and G. Wenes. "An effective Skyrme-type interaction for nuclear structure calculations." In: *Nuclear Physics A* 404.2 (1983), pp. 269–297. ISSN: 0375-9474. DOI: [http://dx.doi.org/10.1016/0375-9474\(83\)90550-X](http://dx.doi.org/10.1016/0375-9474(83)90550-X). URL: <http://www.sciencedirect.com/science/article/pii/037594748390550X>.
- [36] M. Waroquier, G. Wenes, and K. Heyde. "An effective Skyrme-type interaction for nuclear structure calculations." In: *Nuclear Physics A* 404.2 (1983), pp. 298–332. ISSN: 0375-9474. DOI: [http://dx.doi.org/10.1016/0375-9474\(83\)90551-1](http://dx.doi.org/10.1016/0375-9474(83)90551-1). URL: <http://www.sciencedirect.com/science/article/pii/0375947483905511>.
- [37] M. Martini, M. Ericson, G. Chanfray, and J. Marteau. "Unified approach for nucleon knock-out and coherent and incoherent pion production in neutrino interactions with nuclei." In: *Phys. Rev. C* 80 (6 2009), p. 065501. DOI: [10.1103/PhysRevC.80.065501](https://doi.org/10.1103/PhysRevC.80.065501). URL: <https://link.aps.org/doi/10.1103/PhysRevC.80.065501>.
- [38] M. Martini, M. Ericson, G. Chanfray, and J. Marteau. "Neutrino and antineutrino quasielastic interactions with nuclei." In: *Phys. Rev. C* 81 (4 2010), p. 045502. DOI: [10.1103/PhysRevC.81.045502](https://doi.org/10.1103/PhysRevC.81.045502). URL: <https://link.aps.org/doi/10.1103/PhysRevC.81.045502>.
- [39] M. Martini, M. Ericson, and G. Chanfray. "Neutrino quasielastic interaction and nuclear dynamics." In: *Phys. Rev. C* 84 (5 2011), p. 055502. DOI: [10.1103/PhysRevC.84.055502](https://doi.org/10.1103/PhysRevC.84.055502). URL: <https://link.aps.org/doi/10.1103/PhysRevC.84.055502>.
- [40] M. Martini and M. Ericson. "Quasielastic and multinucleon excitations in antineutrino-nucleus interactions." In: *Phys. Rev. C* 87 (6 2013), p. 065501. DOI: [10.1103/PhysRevC.87.065501](https://doi.org/10.1103/PhysRevC.87.065501). URL: <https://link.aps.org/doi/10.1103/PhysRevC.87.065501>.
- [41] J. Nieves, I. Ruiz Simo, and M. J. Vicente Vacas. "Inclusive charged-current neutrino-nucleus reactions." In: *Phys. Rev. C* 83 (4 2011), p. 045501. DOI: [10.1103/PhysRevC.83.045501](https://doi.org/10.1103/PhysRevC.83.045501). URL: <https://link.aps.org/doi/10.1103/PhysRevC.83.045501>.

- [42] J. Nieves, I. Ruiz Simo, and M.J. Vicente Vacas. “The nucleon axial mass and the MiniBooNE quasielastic neutrino–nucleus scattering problem.” In: *Physics Letters B* 707.1 (2012), pp. 72–75. ISSN: 0370-2693. DOI: <https://doi.org/10.1016/j.physletb.2011.11.061>. URL: <http://www.sciencedirect.com/science/article/pii/S0370269311014407>.
- [43] J. Nieves, I. Ruiz Simo, and M.J. Vicente Vacas. “Two particle–hole excitations in charged current quasielastic antineutrino-nucleus scattering.” In: *Physics Letters B* 721.1 (2013), pp. 90–93. ISSN: 0370-2693. DOI: <http://dx.doi.org/10.1016/j.physletb.2013.03.002>. URL: <http://www.sciencedirect.com/science/article/pii/S037026931300213X>.
- [44] Omar Benhar, Nicola Farina, Hiroki Nakamura, Makoto Sakuda, and Ryoichi Seki. “Electron- and neutrino-nucleus scattering in the impulse approximation regime.” In: *Phys. Rev. D* 72 (5 2005), p. 053005. DOI: [10.1103/PhysRevD.72.053005](https://doi.org/10.1103/PhysRevD.72.053005). URL: <https://link.aps.org/doi/10.1103/PhysRevD.72.053005>.
- [45] Omar Benhar, Pietro Coletti, and Davide Meloni. “Electroweak Nuclear Response in the Quasielastic Regime.” In: *Phys. Rev. Lett.* 105 (13 2010), p. 132301. DOI: [10.1103/PhysRevLett.105.132301](https://doi.org/10.1103/PhysRevLett.105.132301). URL: <https://link.aps.org/doi/10.1103/PhysRevLett.105.132301>.
- [46] Omar Benhar, Adelchi Fabrocini, and Stefano Fantoni. “The nucleon spectral function in nuclear matter.” In: *Nuclear Physics A* 505.2 (1989), pp. 267–299. ISSN: 0375-9474. DOI: [http://dx.doi.org/10.1016/0375-9474\(89\)90374-6](http://dx.doi.org/10.1016/0375-9474(89)90374-6). URL: <http://www.sciencedirect.com/science/article/pii/0375947489903746>.
- [47] O. Benhar, A. Fabrocini, S. Fantoni, and I. Sick. “Spectral function of finite nuclei and scattering of GeV electrons.” In: *Nuclear Physics A* 579.3 (1994), pp. 493–517. ISSN: 0375-9474. DOI: [http://dx.doi.org/10.1016/0375-9474\(94\)90920-2](http://dx.doi.org/10.1016/0375-9474(94)90920-2). URL: <http://www.sciencedirect.com/science/article/pii/0375947494909202>.
- [48] J. E. Amaro, M. B. Barbaro, J. A. Caballero, T. W. Donnelly, A. Molinari, and I. Sick. “Using electron scattering superscaling to predict charge-changing neutrino cross sections in nuclei.” In: *Phys. Rev. C* 71 (1 2005), p. 015501. DOI: [10.1103/PhysRevC.71.015501](https://doi.org/10.1103/PhysRevC.71.015501). URL: <https://link.aps.org/doi/10.1103/PhysRevC.71.015501>.
- [49] T. W. Donnelly and Ingo Sick. “Superscaling of inclusive electron scattering from nuclei.” In: *Phys. Rev. C* 60 (6 1999), p. 065502. DOI: [10.1103/PhysRevC.60.065502](https://doi.org/10.1103/PhysRevC.60.065502). URL: <https://link.aps.org/doi/10.1103/PhysRevC.60.065502>.
- [50] G. D. Megias et al. “Meson-exchange currents and quasielastic predictions for charged-current neutrino- ^{12}C scattering in the superscaling approach.” In: *Phys. Rev. D* 91 (7 2015), p. 073004. DOI: [10.1103/PhysRevD.91.073004](https://doi.org/10.1103/PhysRevD.91.073004). URL: <https://link.aps.org/doi/10.1103/PhysRevD.91.073004>.

- [51] O. Buss, T. Gaitanos, K. Gallmeister, H. van Hees, M. Kaskulov, O. Lalakulich, A.B. Larionov, T. Leitner, J. Weil, and U. Mosel. "Transport-theoretical description of nuclear reactions." In: *Physics Reports* 512.1-2 (2012). Transport-theoretical Description of Nuclear Reactions, pp. 1 –124. ISSN: 0370-1573. DOI: <https://doi.org/10.1016/j.physrep.2011.12.001>. URL: <http://www.sciencedirect.com/science/article/pii/S0370157311003619>.
- [52] O. Lalakulich, K. Gallmeister, and U. Mosel. "Neutrino- and antineutrino-induced reactions with nuclei between 1 and 50 GeV." In: *Phys. Rev. C* 86 (1 2012), p. 014607. DOI: [10.1103/PhysRevC.86.014607](https://doi.org/10.1103/PhysRevC.86.014607). URL: <https://link.aps.org/doi/10.1103/PhysRevC.86.014607>.
- [53] J. Ryckebusch, K. Heyde, D. Van Neck, and M. Waroquier. "Aspects of the final-state interaction and long-range correlations in quasi-elastic ($e, e\bar{p}$) and ($e, e\bar{n}$) reactions." In: *Nuclear Physics A* 503.3 (1989), pp. 694 –722. ISSN: 0375-9474. DOI: [http://dx.doi.org/10.1016/0375-9474\(89\)90436-3](http://dx.doi.org/10.1016/0375-9474(89)90436-3). URL: <http://www.sciencedirect.com/science/article/pii/0375947489904363>.
- [54] J. Ryckebusch, M. Waroquier, K. Heyde, J. Moreau, and D. Ryckbosch. "An RPA model for the description of one-nucleon emission processes and application to $^{16}\text{O}(\gamma, N)$ reactions." In: *Nuclear Physics A* 476.2 (1988), pp. 237 –271. ISSN: 0375-9474. DOI: [http://dx.doi.org/10.1016/0375-9474\(88\)90483-6](http://dx.doi.org/10.1016/0375-9474(88)90483-6). URL: <http://www.sciencedirect.com/science/article/pii/0375947488904836>.
- [55] Jonathan Engel. "Approximate treatment of lepton distortion in charged-current neutrino scattering from nuclei." In: *Phys. Rev. C* 57 (4 1998), pp. 2004–2009. DOI: [10.1103/PhysRevC.57.2004](https://doi.org/10.1103/PhysRevC.57.2004). URL: <https://link.aps.org/doi/10.1103/PhysRevC.57.2004>.
- [56] *Deep Underground Neutrino Experiment*. URL: <http://www.dunescience.org>.
- [57] P. Vogel, L.J. Wen, and C. Zhang. "Neutrino oscillation studies with reactors." In: *Nature Communications* 6 (). URL: <http://dx.doi.org/10.1038/ncomms7935>.
- [58] P. Adamson et al. "The NuMI neutrino beam." In: *Nuclear Instruments and Methods in Physics Research Section A: Accelerators, Spectrometers, Detectors and Associated Equipment* 806 (2016), pp. 279 –306. ISSN: 0168-9002. DOI: <https://doi.org/10.1016/j.nima.2015.08.063>. URL: <http://www.sciencedirect.com/science/article/pii/S016890021501027X>.
- [59] L. Aliaga et al. "Neutrino flux predictions for the NuMI beam." In: *Phys. Rev. D* 94 (9 2016), p. 092005. DOI: [10.1103/PhysRevD.94.092005](https://doi.org/10.1103/PhysRevD.94.092005). URL: <https://link.aps.org/doi/10.1103/PhysRevD.94.092005>.
- [60] *Japan Proton Accelerator Research Complex*. URL: <https://j-parc.jp/Neutrino/en/index.html>.

- [61] K. Abe, N. Abgrall, Y. Ajima, H. Aihara, J.B. Albert, and C. Andreopoulos. "Measurements of the T2K neutrino beam properties using the INGRID on-axis near detector." In: *Nuclear Instruments and Methods in Physics Research Section A: Accelerators, Spectrometers, Detectors and Associated Equipment* 694 (2012), pp. 211–223. ISSN: 0168-9002. DOI: <https://doi.org/10.1016/j.nima.2012.03.023>. URL: <http://www.sciencedirect.com/science/article/pii/S0168900212002987>.
- [62] ND280. URL: <http://nd280.org/info>.
- [63] A.A. Aguilar-Arevalo et al. "The MiniBooNE detector." In: *Nuclear Instruments and Methods in Physics Research Section A: Accelerators, Spectrometers, Detectors and Associated Equipment* 599.1 (2009), pp. 28–46. ISSN: 0168-9002. DOI: <https://doi.org/10.1016/j.nima.2008.10.028>. URL: <http://www.sciencedirect.com/science/article/pii/S0168900208015404>.
- [64] S. Fukuda et al. "The Super-Kamiokande detector." In: *Nuclear Instruments and Methods in Physics Research Section A: Accelerators, Spectrometers, Detectors and Associated Equipment* 501.2–3 (2003), pp. 418–462. ISSN: 0168-9002. DOI: [https://doi.org/10.1016/S0168-9002\(03\)00425-X](https://doi.org/10.1016/S0168-9002(03)00425-X). URL: <http://www.sciencedirect.com/science/article/pii/S016890020300425X>.
- [65] *The ArgoNeuT experiment*. URL: <http://t962.fnal.gov/index.html>.
- [66] *MicroBooNE*. URL: <http://www-microboone.fnal.gov/>.
- [67] R. Acciarri et al. "Detection of back-to-back proton pairs in charged-current neutrino interactions with the ArgoNeuT detector in the NuMI low energy beam line." In: *Phys. Rev. D* 90 (1 2014), p. 012008. DOI: [10.1103/PhysRevD.90.012008](https://doi.org/10.1103/PhysRevD.90.012008). URL: <https://link.aps.org/doi/10.1103/PhysRevD.90.012008>.
- [68] *The Minerva experiment*. URL: <http://minerva.fnal.gov/>.
- [69] *Neutrino unbound website*. URL: <http://www.nu.to.infn.it/>.
- [70] *The Nova experiment*. URL: <https://www-nova.fnal.gov/>.
- [71] Teppei Katori and Marco Martini. "Neutrino-Nucleus Cross Sections for Oscillation Experiments." In: (2016). arXiv: [1611.07770](https://arxiv.org/abs/1611.07770) [hep-ph].
- [72] A. Aguilar et al. "Evidence for neutrino oscillations from the observation of $\bar{\nu}_e$ appearance in a $\bar{\nu}_\mu$ beam." In: *Phys. Rev. D* 64 (11 2001), p. 112007. DOI: [10.1103/PhysRevD.64.112007](https://doi.org/10.1103/PhysRevD.64.112007). URL: <https://link.aps.org/doi/10.1103/PhysRevD.64.112007>.
- [73] A. A. Aguilar-Arevalo et al. "Measurement of Muon Neutrino Quasielastic Scattering on Carbon." In: *Phys. Rev. Lett.* 100 (3 2008), p. 032301. DOI: [10.1103/PhysRevLett.100.032301](https://doi.org/10.1103/PhysRevLett.100.032301). URL: <https://link.aps.org/doi/10.1103/PhysRevLett.100.032301>.

- [74] A. A. Aguilar-Arevalo et al. "First measurement of the muon antineutrino double-differential charged-current quasielastic cross section." In: *Phys. Rev. D* 88 (3 2013), p. 032001. DOI: [10.1103/PhysRevD.88.032001](https://doi.org/10.1103/PhysRevD.88.032001). URL: <https://link.aps.org/doi/10.1103/PhysRevD.88.032001>.
- [75] J. Nieves, I. Ruiz Simo, and M.J. Vicente Vacas. "The nucleon axial mass and the MiniBooNE quasielastic neutrino–nucleus scattering problem." In: *Physics Letters B* 707.1 (2012), pp. 72–75. ISSN: 0370-2693. DOI: <https://doi.org/10.1016/j.physletb.2011.11.061>. URL: <http://www.sciencedirect.com/science/article/pii/S0370269311014407>.
- [76] A. A. Aguilar-Arevalo et al. "Measurement of neutrino-induced charged-current charged pion production cross sections on mineral oil at $E_\nu \sim 1$ GeV." In: *Phys. Rev. D* 83 (5 2011), p. 052007. DOI: [10.1103/PhysRevD.83.052007](https://doi.org/10.1103/PhysRevD.83.052007). URL: <https://link.aps.org/doi/10.1103/PhysRevD.83.052007>.
- [77] A. A. Aguilar-Arevalo et al. "Measurement of ν_μ -induced charged-current neutral pion production cross sections on mineral oil at $E_\nu \in 0.5\text{--}2.0$ GeV." In: *Phys. Rev. D* 83 (5 2011), p. 052009. DOI: [10.1103/PhysRevD.83.052009](https://doi.org/10.1103/PhysRevD.83.052009). URL: <https://link.aps.org/doi/10.1103/PhysRevD.83.052009>.
- [78] K. Abe et al. "Evidence of electron neutrino appearance in a muon neutrino beam." In: *Phys. Rev. D* 88 (3 2013), p. 032002. DOI: [10.1103/PhysRevD.88.032002](https://doi.org/10.1103/PhysRevD.88.032002). URL: <https://link.aps.org/doi/10.1103/PhysRevD.88.032002>.
- [79] M. Martini, M. Ericson, and G. Chanfray. "Neutrino energy reconstruction problems and neutrino oscillations." In: *Phys. Rev. D* 85 (9 2012), p. 093012. DOI: [10.1103/PhysRevD.85.093012](https://doi.org/10.1103/PhysRevD.85.093012). URL: <https://link.aps.org/doi/10.1103/PhysRevD.85.093012>.
- [80] J. Nieves, F. Sánchez, I. Ruiz Simo, and M. J. Vicente Vacas. "Neutrino energy reconstruction and the shape of the charged current quasielastic-like total cross section." In: *Phys. Rev. D* 85 (11 2012), p. 113008. DOI: [10.1103/PhysRevD.85.113008](https://doi.org/10.1103/PhysRevD.85.113008). URL: <https://link.aps.org/doi/10.1103/PhysRevD.85.113008>.
- [81] M. Martini, M. Ericson, and G. Chanfray. "Energy reconstruction effects in neutrino oscillation experiments and implications for the analysis." In: *Phys. Rev. D* 87 (1 2013), p. 013009. DOI: [10.1103/PhysRevD.87.013009](https://doi.org/10.1103/PhysRevD.87.013009). URL: <https://link.aps.org/doi/10.1103/PhysRevD.87.013009>.
- [82] O. Lalakulich, U. Mosel, and K. Gallmeister. "Neutrino energy reconstruction in quasielastic-like scattering in the MiniBooNE and T2K experiments." In: *Phys. Rev. C* 86 (5 2012), p. 054606. DOI: [10.1103/PhysRevC.86.054606](https://doi.org/10.1103/PhysRevC.86.054606). URL: <https://link.aps.org/doi/10.1103/PhysRevC.86.054606>.
- [83] A. A. Aguilar-Arevalo et al., MiniBooNE Collaboration. "Unexplained Excess of Electronlike Events from a 1-GeV Neutrino Beam." In: *Phys. Rev. Lett.* 102 (10 2009), p. 101802. DOI: [10.1103/PhysRevLett.102.101802](https://doi.org/10.1103/PhysRevLett.102.101802). URL: <https://link.aps.org/doi/10.1103/PhysRevLett.102.101802>.

- [84] M. Ericson, M. V. Garzelli, C. Giunti, and M. Martini. “Assessing the role of nuclear effects in the interpretation of the MiniBooNE low-energy anomaly.” In: *Phys. Rev. D* 93 (7 2016), p. 073008. DOI: [10.1103/PhysRevD.93.073008](https://doi.org/10.1103/PhysRevD.93.073008). URL: <https://link.aps.org/doi/10.1103/PhysRevD.93.073008>.
- [85] J. E. Amaro, M. B. Barbaro, J. A. Caballero, T. W. Donnelly, and C. Maieron. “Semirelativistic description of quasielastic neutrino reactions and superscaling in a continuum shell model.” In: *Phys. Rev. C* 71 (6 2005), p. 065501. DOI: [10.1103/PhysRevC.71.065501](https://doi.org/10.1103/PhysRevC.71.065501). URL: <https://link.aps.org/doi/10.1103/PhysRevC.71.065501>.
- [86] M. Martini, N. Jachowicz, M. Ericson, V. Pandey, T. Van Cuyck, and N. Van Dessel. “Electron-neutrino scattering off nuclei from two different theoretical perspectives.” In: *Phys. Rev. C* 94 (1 2016), p. 015501. DOI: [10.1103/PhysRevC.94.015501](https://doi.org/10.1103/PhysRevC.94.015501). URL: <https://link.aps.org/doi/10.1103/PhysRevC.94.015501>.
- [87] K. Abe et al., T2K Collaboration. “Measurements of neutrino oscillation in appearance and disappearance channels by the T2K experiment with 6.6×10^{20} protons on target.” In: *Phys. Rev. D* 91 (7 2015), p. 072010. DOI: [10.1103/PhysRevD.91.072010](https://doi.org/10.1103/PhysRevD.91.072010). URL: <https://link.aps.org/doi/10.1103/PhysRevD.91.072010>.
- [88] V. Pandey, N. Jachowicz, M. Martini, R. González-Jiménez, J. Ryckebusch, T. Van Cuyck, and N. Van Dessel. “Impact of low-energy nuclear excitations on neutrino-nucleus scattering at MiniBooNE and T2K kinematics.” In: *Phys. Rev. C* 94 (5 2016), p. 054609. DOI: [10.1103/PhysRevC.94.054609](https://doi.org/10.1103/PhysRevC.94.054609). URL: <https://link.aps.org/doi/10.1103/PhysRevC.94.054609>.
- [89] R.A. Smith and E.J. Moniz. “Neutrino reactions on nuclear targets.” In: *Nuclear Physics B* 43 (1972), pp. 605–622. ISSN: 0550-3213. DOI: [http://dx.doi.org/10.1016/0550-3213\(72\)90040-5](http://dx.doi.org/10.1016/0550-3213(72)90040-5). URL: <http://www.sciencedirect.com/science/article/pii/0550321372900405>.
- [90] Artur M. Ankowski, Omar Benhar, and Makoto Sakuda. “Improving the accuracy of neutrino energy reconstruction in charged-current quasielastic scattering off nuclear targets.” In: *Phys. Rev. D* 91 (3 2015), p. 033005. DOI: [10.1103/PhysRevD.91.033005](https://doi.org/10.1103/PhysRevD.91.033005). URL: <https://link.aps.org/doi/10.1103/PhysRevD.91.033005>.
- [91] G. D’Agostini. “A multidimensional unfolding method based on Bayes’ theorem.” In: *Nuclear Instruments and Methods in Physics Research Section A: Accelerators, Spectrometers, Detectors and Associated Equipment* 362.2 (1995), pp. 487–498. ISSN: 0168-9002. DOI: [http://dx.doi.org/10.1016/0168-9002\(95\)00274-X](http://dx.doi.org/10.1016/0168-9002(95)00274-X). URL: <http://www.sciencedirect.com/science/article/pii/016890029500274X>.

- [92] K. Abe et al. "Measurement of the Inclusive Electron Neutrino Charged Current Cross Section on Carbon with the T2K Near Detector." In: *Phys. Rev. Lett.* 113 (24 2014), p. 241803. DOI: [10.1103/PhysRevLett.113.241803](https://doi.org/10.1103/PhysRevLett.113.241803). URL: <https://link.aps.org/doi/10.1103/PhysRevLett.113.241803>.
- [93] J. Spitz. "Sterile neutrino search with kaon decay at rest." In: *Phys. Rev. D* 85 (9 2012), p. 093020. DOI: [10.1103/PhysRevD.85.093020](https://doi.org/10.1103/PhysRevD.85.093020). URL: <https://link.aps.org/doi/10.1103/PhysRevD.85.093020>.
- [94] S. Ajimura et al. "Technical Design Report (TDR): Searching for a Sterile Neutrino at J-PARC MLF (E56, JSNS2)." In: (2017). arXiv: [1705.08629](https://arxiv.org/abs/1705.08629) [[physics.ins-det](https://arxiv.org/abs/1705.08629)].

LIST OF FIGURES

Figure 2.1	Feynman diagram of charged current neutrino-nucleus scattering	18
Figure 2.2	Figure from [37] showing the lowest order contribution of the Δ -excitation on the RPA propagator.	26
Figure 3.1	Overview of the Deep Underground Neutrino Experiment (DUNE) [56], a long-baseline accelerator based neutrino experiment.	29
Figure 3.2	Prediction of the solar neutrino flux	30
Figure 3.3	Schematic depiction of the neutrino beam production at Neutrinos at the Main Injector (NuMI)	31
Figure 3.4	The NuMI flux for different horn configurations from [58]	33
Figure 4.1	Energy distribution for fixed lepton observables for the CRPA and HF models compared to a relativistic Fermi gas	40
Figure 4.2	Energy distributions for fixed lepton observables using the MiniBooNE flux	41
Figure 4.3	Comparison of the MiniBooNE and T2K near detector flux predictions [8, 87].	42
Figure 4.4	Energy distributions with fixed lepton observables for the T2K flux	43
Figure 4.5	Comparison of double differential cross sections in the HF/CRPA and LRFG/RPA (<i>QE bare</i> / <i>QE RPA</i>) approaches	44
Figure 5.1	The effect of the separation energy and rest mass of the final state lepton on $\cos\theta(E_l, \bar{E}_\nu)$.	53
Figure 5.2	Effect of a separation energy of $E_B = 34$ MeV on the distribution $I(E_\nu, \bar{E}_\nu)$ using the MiniBooNE flux[8].	54
Figure 5.3	Effect of the final state lepton mass on the distribution $d(E_\nu, \bar{E}_\nu)$.	55
Figure 5.4	Comparison of $d(E_\nu, \bar{E}_\nu)$ in the HF and CRPA approach for fixed values of \bar{E}_ν	56
Figure 5.5	Contributions of the cross section to $d(E_\nu, \bar{E}_\nu = 500$ MeV) for different neutrino energies	58
Figure 5.6	$d(E_\nu, \bar{E}_\nu)$ for fixed values of E_ν in the HF and CRPA description	58
Figure 5.7	$d(E_\nu, \bar{E}_\nu)$ for fixed values of E_ν in a RFG model and the CRPA	59
Figure 5.8	$d(E_\nu, \bar{E}_\nu)$ for fixed values of E_ν in the CRPA approach and the RPA+LRFG(+2p2h)	61
Figure 5.9	two dimensional representation of the flux weighted (reconstructed) energy distribution	62

Figure 5.10	The total cross section as obtained from a straightforward integration over the phase space and from $d(E_\nu, \bar{E}_\nu)$ for different cut-off values	63
Figure 5.11	Effect of the binding energy E_b on the reconstructed distribution for different RFG energy shifts E_s	65
Figure 5.12	The (flux weighted) cross section for the RFG- and CRPA models with different cut-offs	67
Figure 5.13	MiniBooNE flux-folded cross sections in terms of E_ν and \bar{E}_ν .	67
Figure 5.14	The cross section in terms of the unfolded energy	68
Figure 6.1	Comparison of the flux-folded cross section in terms of neutrino energy E_ν with the cross section in terms of \bar{E}_ν	71

LIST OF TABLES

Table 1.1	Overview of the fermions in the standard model	9
Table 3.1	Selected accelerator based experiments that measure the neutrino-nucleus cross section	34

ACRONYMS

RFG	Relativistic Fermi Gas
SNO	Sudbury neutrino observatory
NuMI	Neutrinos at the Main Injector
IA	Impulse Aproximation
CCQE	Charged-Current Quasi Elastic
CRPA	Continuum Random Phase Approximation
T2K	Tokai-to-Kamiokande
HF	Hartree Fock
DUNE	Deep Underground Neutrino Experiment
FNAL	Fermi National Accelerator Laboratory

MiniBooNE Miniature Booster Neutrino Experiment

BNB Booster Neutrino Beamline

LArTPC Liquid Argon Time Projection Chamber

PMNS Pontecorvo-Maki-Nakagawa-Sakata